TECHNISCHE UNIVERSITÄT WIEN

D I P L O M A R B E I T

Holotomographic microscopy of subcellular structures and nuclear dynamics in filamentous fungi

Ausgeführt am Institut für

Verfahrenstechnik, Umwelttechnik und technische Biowissenschaften

der Technischen Universität Wien

unter der Anleitung von Assoc. Prof. Dr. Matthias Steiger und DI^{in} Susanne Fritsche

durch

Felix Fronek

13.03.2024 Felix Fronek

Table of contents

Eidesstattliche Erklärung

Ich erkläre an Eides statt, dass ich die vorliegende Arbeit selbstständig und ohne fremde Hilfe verfasst, andere als die angegebenen Quellen und Hilfsmittel nicht benutzt bzw. die wörtlich oder sinngemäß entnommenen Stellen als solche kenntlich gemacht habe. Zudem bestätige ich, dass keine künstliche Intelligenz (KI) für die Verfassung der Arbeit bzw. für Teile der Arbeit zum Einsatz gekommen ist.

Wien, am 13.03.2024

……
Felix Fronek

Einverständniserklärung zur Plagiatsprüfung

Ich nehme zur Kenntnis, dass die vorgelegte Arbeit mit geeigneten und dem derzeitigen Stand der Technik entsprechenden Mitteln (Plagiat-Erkennungssoftware) elektronisch-technisch überprüft wird. Dies stellt einerseits sicher, dass bei der Erstellung der vorgelegten Arbeit die hohen Qualitätsvorgaben im Rahmen der ausgegebenen der an der TU Wien geltenden Regeln zur Sicherung guter wissenschaftlicher Praxis - „Code of Conduct“ (Mitteilungsblatt 2007, 26. Stück, Nr. 257 idgF.) an der TU Wien eingehalten wurden. Zum anderen werden durch einen Abgleich mit anderen studentischen Abschlussarbeiten Verletzungen meines persönlichen Urheberrechts vermieden.

Wien, am 13.03.2024

……
Felix Fronek

Danksagung

Hiermit möchte ich mich bei allen Menschen Bedanken die mich während der Diplomarbeit sowie während dem Studium unterstützt haben. Besonderer Dank gilt **Prof. Matthias Steiger** und der Firma **ACIB**, welche diese Arbeit erst ermöglicht haben. Auch bei meiner Betreuerin **Susanne Fritsche** möchte ich mich ausdrücklich bedanken für die kontinuierliche Unterstützung während und auch nach der praktischen Arbeit. Weiters möchte ich mich bei der gesamten Arbeitsgruppe herzlich bedanken für eine großartige Zeit im und auch außerhalb des Labors.

Auch bei meiner Familie möchte ich mich bedanken für jegliche Unterstützung während meines Studiums. Nicht zuletzt gilt mein Dank auch meinem guten Freund **Dominik Hofreither** der mich von Beginn an für das gesamte Masterstudium motiviert hat und immer hilfsbereit war, trotz eigenem Stress im Studium.

Abstract

The morphology of filamentous fungi is determined by key events including the emergence of germ tubes, hyphal elongation as well as the formation of apical and lateral branches. *Aspergillus niger* is a fungus commonly used in the industrial production of citric acid. Growth characteristics such as the formation of a hyphal network are of great importance as they influence the secretion of the organic acid by the fungus. In this respect, live-cell imaging can be a powerful tool to study the morphogenesis of the fungus. However, most conventional high-resolution live-cell imaging techniques either require fluorescent markers or cannot be used for 3D imaging.

In this work, morphological differences of *Aspergillus niger* wild type ATCC 1015 and an improved industrial citric acid producing strain (ACIB1) were captured using a label-free live-cell imaging system based on quantitative phase imaging (QPI). Visualization was performed by creating a 3D refractive index (RI) map of the sample using holotomographic microscopy (HTM), a method that has been frequently applied to mammalian cells in recent years. In addition, subcellular structures of the fungi *A. niger*, *Aureobasidium pullulans*, and *Trichoderma reesei* were targeted. Organelle-specific fluorescent dyes or GFP-tagged proteins were used to allow identification of subcellular structures based on characteristic RI patterns. Furthermore, live-cell HTM coupled with fluorescence imaging was performed to investigate nuclear dynamics and the cyclin-dependent kinase (CDK) $NimX^{Cdc2}$ of *A. niger*. Genetic engineering was performed with Golden Gate cloning and an *in-vivo* expressed CRISPR/Cas9 system.

Prominent subcellular structures such as lipid droplets and vacuoles were successfully assigned to an RI pattern. In addition, it was confirmed that the fungal cell wall significantly affects the visualization of cellular contents with HTM. Thus, a detailed RI map as obtained for mammalian cells cannot be achieved for fungi without considering the fungal cell wall. However, the general applicability of HTM on fungi was demonstrated and morphological analyses revealed significant differences in growth between the *A. niger* wild type strain and the citric acid producer. Furthermore, synchronous nuclei division in apical hyphal compartments was observed. The investigation of the GFP-tagged CDK $NimX^{Cdc2}$ showed an accumulation in the nuclei at certain time points. The absence of nuclear division in the GFP signal suggests that $NimX^{Cdc2}$ is not located in the nucleus during cytokinesis.

Zusammenfassung

Die Morphologie filamentöser Pilze wird durch Schlüsselereignisse, wie der Entstehung von Keimschläuchen, dem Hyphenwachstum sowie der Bildung apikaler und lateraler Verzweigungen bestimmt. *Aspergillus niger* ist ein Pilz, der häufig für die industrielle Herstellung von Zitronensäure verwendet wird. Wachstumsmerkmale wie die Bildung eines Hyphen-Netzwerks sind von großer Bedeutung, da sie die Sekretion der organischen Säure durch den Pilz beeinflussen. In dieser Hinsicht kann die Bildgebung lebender Zellen ein leistungsfähiges Instrument zur Untersuchung der Morphogenese des Pilzes sein. Die meisten konventionellen hochauflösenden Live-Cell-Imaging-Techniken erfordern jedoch entweder Fluoreszenzmarker oder können nicht für 3D-Imaging verwendet werden.

In dieser Arbeit wurden die morphologischen Unterschiede zwischen dem *A. niger* Wildtyp ATCC 1015 und einem Zitronensäure-produzierenden Industriestamm (ACIB1) mit einem markierungsfreien Live-Cell-Imaging-System erfasst, das auf quantitativer Phasenbildgebung (QPI) basiert. Die Visualisierung erfolgte durch die Erstellung einer 3D-Brechungsindexkarte (RI map) der Probe mit Hilfe der holotomographischen Mikroskopie (HTM), einer Methode, die in den letzten Jahren häufig bei Säugetierzellen angewendet wurde. Darüber hinaus wurden subzelluläre Strukturen der Pilze *A. niger*, *Aureobasidium pullulans* und *Trichoderma reesei* untersucht. Organellenspezifische Fluoreszenzfarbstoffe oder GFP-markierte Proteine wurden verwendet, um die Identifizierung subzellulärer Strukturen auf der Grundlage charakteristischer RI-Muster zu ermöglichen. Weiters wurde Live-cell HTM mit Fluoreszenzbildgebung gekoppelt, um das Verhalten von Zellkernen und der Cyclin-abhängigen Kinase (CDK) $NimX^{Cdc2}$ von *A. niger* zu untersuchen. Genmodifikation wurden mittels Golden Gate cloning und einem *in-vivo* exprimierten CRISPR/Cas9-System durchgeführt.

Auffällige subzelluläre Strukturen wie Lipidtropfen und Vakuolen konnten erfolgreich einem RI-Muster zugeordnet werden. Darüber hinaus wurde bestätigt, dass die Zellwand von Pilzen die Visualisierung von Zellinhalten mittels HTM erheblich beeinträchtigt. Eine detaillierte RI-Karte, wie sie für Säugetierzellen erhalten wurde, kann daher für Pilze ohne Berücksichtigung der Pilzzellwand nicht erreicht werden. Die allgemeine Anwendbarkeit von HTM auf Pilze wurde jedoch demonstriert und morphologische Analysen zeigten signifikante Wachstumsunterschiede zwischen dem A. niger Wildtyp-Stamm und dem Zitronensäureproduzenten. Außerdem wurde eine synchrone Kernteilung in apikalen

Hyphenkompartimenten beobachtet. Die Untersuchung der GFP-markierten CDK NimX^{Cdc2} zeigte eine Akkumulation in den Kernen zu bestimmten Zeitpunkten. Das Fehlen der Kernteilung im GFP-Signal deutet darauf hin, dass sich NimX^{Cdc2} während der Zytokinese nicht im Zellkern befindet.

1. Introduction

1.1. Optical microscopy

The first use of a compound microscope in Europe was documented in 1623 by Galileo Galilei (Galilei, 1623). The integration of microscopes into the realm of biology gained prominence in the late 17th century with Antonie van Leeuwenhoek. His microscopes were equipped with a singular, exceptionally powerful lens, and it took 150 years for compound microscopes to achieve comparable resolution quality (Lane, 2015). Decisive progress was made in 1893 when August Köhler introduced Köhler illumination, which made it possible to overcome limitations such as images of the light source in the resulting image and uneven illumination (Köhler, 1893). Another milestone was reached in the early 1930s with the development of phase contrast microscopy (PCM) by Frits Zernike. PCM uses interference instead of light absorption and facilitates the imaging of transparent samples such as unstained mammalian cells (Zernike, 1955). Zernike's contributions were honored with the Nobel Prize in Physics in 1953 and formed the basis for differential interference contrast microscopy (DIC), which was developed around 1950 (Nomarski, 1955).

PCM is currently the most frequently used method of wide-field microscopy in biology. It allows for the recognition of a wider range of cellular structures compared to bright-field microscopy. This technique converts the phase fluctuations caused by the specimen into changes in light amplitude, enabling the visualization of low-contrast specimens such as unstained living cells. However, one of the disadvantages of this method is the presence of artifacts, such as a bright halo around the samples and a gradual shading from the edges to the center of the sample (Yin et al., 2012).

DIC microscopy represents a further development of PCM and also belongs to the wide-field microscopy techniques. The utilization of two orthogonally polarized lights eliminates artifacts that are observed in PCM. This method offers advantages such as high contrast and high spatial resolution, which facilitates the observation of intricate details. However, the technique is sensitive to changes in the orientation of the light source, potentially leading to information loss (Snyder et al., 1999).

The development of various fluorescence markers has enabled the scientific field of fluorescence microscopy to visualize molecules, proteins, or subcellular structures in a

targeted manner. These inventions were particularly interesting for bioscience and medicine. Currently, there is a wide range of labeling reagents and techniques available for almost all types of applications. Ranging from classical stains such as DAPI to fluorescence-labeled antibodies for specific biomolecule recognition and fluorescent proteins like GFP, which can be expressed in vivo and fused to other proteins of interest. Widefield fluorescence microscopy, also known as epifluorescence microscopy, employs a simple setup with a dichroic beamsplitter reflecting the excitation light while transmitting the higher-wavelength fluoresced light to the ocular. However, compared to conventional light microscopy, it demands higher illumination power, posing the risk of photodamage or phototoxic effects (Cox, 2012).

On this basis, a variety of different and specialized microscopy techniques have been developed, all of which have their own advantages and disadvantages. However, many of the newer techniques, particularly in the field of super-resolution microscopy (SRM), require the use of fluorophores and subsequent fluorescence imaging. While advantageous for achieving high resolution, this dependency may be undesirable, particularly when working with living cells.

1.2. Live-cell imaging

Live-cell imaging has gained increased interest with the advancement of analytical tools that can be used *in-vivo*. Although living cells were first imaged in 1907, the invention of PCM in the 1930s represented a significant breakthrough since it allowed for detailed observation of organelle movements within the cell (Landecker, 2009). However, the timeframe captured during the early stages of live-cell imaging was limited due to the unfavorable conditions for living cells under a microscope. In the late 1980s, Sally Temple achieved an experimental breakthrough by placing an old microscope within an incubator and establishing an amateur live-cell imaging device This allowed for imaging time to be extended up to seven days, a significant increase from the common maximum of several hours. Since then, live-cell imaging techniques have been continually developed, and today there is a wide range of devices available, including computerized incubation chambers for various organisms and applications. This eliminates previous challenges in maintaining cell health, such as controlling temperature, oxygen levels, and humidity (Baker, 2010).

While live-cell imaging offers the ability to capture cellular events or track fluorescent probes and proteins, there are still hurdles to overcome. In addition to high optical resolution, phototoxicity is one of the major remaining challenges, especially in live-cell imaging coupled with fluorescence microscopy, which is commonly used to observe fluorescent markers. In general, lower photon doses have less impact on cellular processes. Therefore, it is important to select the imaging method that has the least impact on cell health while still being sufficient for the desired live-cell experiment. If fluorescence microscopy is required, factors such as excitation wavelength, fluorophores, exposure time, intensity, media, and oxygen concentration can be optimized to minimize the impact on cell health (Cole, 2014; Laissue et al., 2017)

1.2.1. Common live-cell imaging techniques

The choice of live-cell imaging method depends on the specific application. Currently, there are numerous techniques available, including widefield microscopy (WFM), which is the oldest method. WFM is simple and cost-effective, and includes brightfield microscopy, dark-field microscopy, PCM, DIC microscopy, and widefield fluorescence microscopy. Since WFM illuminates the entire specimen, it requires very low photon doses, minimizing the effects on cellular health. The technique is based on transmitted light and can be used to visualize fluorophores (Cole, 2014). By using post-processing methods, confocal quality can be approached with a much lower photon dose compared to laser scanning confocal microscopy (LSCM) (Swedlow & Platani, 2002).

Confocal microscopy yields higher resolution than WFM as it focuses imaging on a single spot of the specimen. The illumination light passes through a pinhole, allowing for illumination of only the field of view and reducing scattering effects from the surrounding specimen, which, in turn, results in higher resolution. Currently, LSCM is the most commonly used confocal microscopy method. It is capable of 3D imaging (x, y, z) by changing the focal point. However, it relies on fluorophores. The pinhole used for illumination in LSCM is small, requiring a high photon dose that leads to increased phototoxicity compared to WFM. To scan the entire specimen, the microscope stage must be moved over the light source, resulting in slower imaging speed. Thus, LSCM's suitability for live-cell imaging is limited. On the other hand, spinning disk confocal microscopy (SDCM) features two rotating disks with multiple pinholes arranged in a spiral, in contrast to LSCM's single pinhole, making it more suitable for live-cell

imaging. Fast imaging of the entire specimen is possible with the SDCM, which requires a lower photon dose and therefore causes less phototoxicity compared to LSCM. This makes the SDCM ideal for live-cell imaging (Cole, 2014; Elliott, 2020).

In contrast to fluorescence microscopy, quantitative phase imaging (QPI) is a label-free technique. It is an advancement of PCM and DIC microscopy, as it is based on the same principle. However, the recorded phase shift in QPI is decoupled from light intensity, which enables the extraction of quantitative information. This allows non-destructive, time-lapse determination of single-cell volume and mass. The main advantages of QPI include lower phototoxicity, no photobleaching, and high imaging speed. Numerous different QPI methods are currently utilized in various biological and medical applications. New methods are continually being developed, with a particular focus on breaking the Abbe diffraction limit to approach super-resolution, as described in the next chapter (Y. K. Park et al., 2018).

1.2.2. Super resolution microscopy

The field of super-resolution microscopy (SRM), also known as nanoscopy, is currently rapidly expanding. Achieving high spatial resolution below 100 nm is a significant challenge in live-cell imaging. To overcome the Abbe diffraction limit, which is defined by **Equation 1** (Lipson et al., 1995), several novel techniques have been developed.

***Equation 1**: Minimum resolvable distance d of a microscope according to Abbe's law.*

$$d = \frac{\lambda}{2NA}$$

The minimum resolvable distance is determined by dividing the wavelength λ by two times the numerical aperture (NA) of the microscope objective. NA, which is dimensionless, can be defined by **Equation 2**, where n is the refractive index of the immersion medium and θ is the half-angle of the maximum light cone allowed to enter or exit the objective (Lipson et al., 1995).

***Equation 2**: Calculation of the numerical aperture NA for a microscope objective.*

$$NA = n \times sin\theta$$

Modern microscopes typically have numerical aperture values that can reach 1.4-1.6. Therefore, the minimum resolution achievable when imaging with visible light wavelengths cannot be below 100 nm. However, there are several SRM techniques that can overcome this

diffraction limit, allowing for optical resolution below 100 nm. Two distinct approaches can be utilized to achieve this (Laine et al., 2023).

The initial method is referred to as single-molecule localization microscopy (SMLM) and comprises stimulated emission depletion (STED), photoactivated localization microscopy (PALM), and stochastic optical reconstruction microscopy (STORM). These approaches are considered diffraction-unlimited and have the capacity to achieve high spatial resolution near molecular resolution (10-20 nm). The technique takes advantage of the ON/OFF switching capabilities of specific fluorophores. However, the process of acquiring images using PALM and STORM is slow, as it requires thousands of acquisitions to reconstruct a single image (Laine et al., 2023).

The second set of so-called fluctuation-based approaches use diffraction-limited data to reconstruct super-resolution images and include super-resolution radial fluctuations (SRRFs), super-resolution optical fluctuation imaging (SOFI), Bayesian analysis of blinking and bleaching, multiple signal classification algorithm, or super-resolution with auto-correlation two-step deconvolution. Compared to SMLM, only small intensity variations between frames are required to generate a super-resolution image. In addition, these approaches require less illumination power. Since they generally have a higher acquisition speed and are compatible with most fluorescence microscopes, they can be used for long-term live-cell imaging (Laine et al., 2023). However, all these techniques require at least one fluorophore and its excitation. Therefore, photodamage or phototoxicity cannot be completely excluded, even if the required illumination power is low.

1.2.3. Holotomographic microscopy

Holotomographic microscopy (HTM), also known as optical diffraction tomography, is a label-free technique that can approach a resolution similar to SRM (Cotte et al., 2013). This technique belongs to the QPI methods, as it reconstructs phase images. Unlike most super-resolution techniques, it generates a 3D image by measuring the refractive index (RI) distribution of biological samples. Since RI is an intrinsic optical property, there is no need for labeling. This represents the major difference to other SRM techniques (D. Kim et al., 2018).

In detail, image acquisition is accomplished by sequentially illuminating the sample with a low-power laser beam at an oblique angle, in a 360° pattern. By this, the scattered field is measured in all possible directions. The resulting complex wave field can be utilized to reconstruct a 3D

RI distribution, or RI map, of the sample. The microscope uses a Mach-Zehnder interferometer to acquire quantitative phase images from hologram recordings. To achieve this, a laser beam, with a wavelength of λ = 520 nm, is divided into sample and reference beam. The sample is illuminated from all possible angles using a motorized tilted mirror set at a steep angle. After re-combining the sample and reference beams, a hologram is recorded for each illumination direction, allowing for phase images to be calculated using Fresnel reconstruction (Cotte et al., 2013; D. Kim et al., 2018).

HTM can achieve lateral resolution of less than 100 nm, and because it does not require fluorophores or high photon doses, it is excellent for high-resolution, long-term 4D imaging. Compared to other SRM techniques, phototoxic effects are minimized with HTM. Furthermore, quantitative information such as cell dry mass and cell volume of biological samples can be extracted from the RI map (T. I. Kim et al., 2017; S. Lee et al., 2014). If necessary, the technique can be coupled with 2D fluorescence microscopy (Cotte et al., 2013; D. Kim et al., 2018).

Given these advantages, HTM has been extensively applied to various mammalian cell types, including red blood cells (H. Park et al., 2015), white blood cells (S. Park et al., 2022), neuron cells (Hingorani et al., 2022), epithelial cells (Buzalewicz et al., 2022) and hepatocytes (K. Kim et al., 2016), among others. Sandoz et al. demonstrated the identification of subcellular structures like mitochondria, lipid droplets, and lipid-rich endocytic structures based on their RI, although the endoplasmic reticulum (ER) and Golgi apparatus were not discernible in the RI map. In their study, fluorescent markers overlaid on the RI map confirmed organelle-specific RI values. Nuclei, although not specifically targeted, were clearly visible in the RI map. Notably, they developed a tool to measure pre-mitotic nuclear rotation (Sandoz et al., 2019).

The 2D RI map of unlabeled HeLa cells from the work of Sandoz et al. is presented in **Figure 1**. Lipid droplets, marked with red arrows, are visible as bright spots, indicating a high RI. Nuclei, marked with blue arrows, appear as large, distinct subcellular structures with areas of higher and lower RI compared to the cytosol. The mitochondrial networks, marked with the green arrows, are characterized by thin filaments with a slightly brighter color compared to the cytosol.

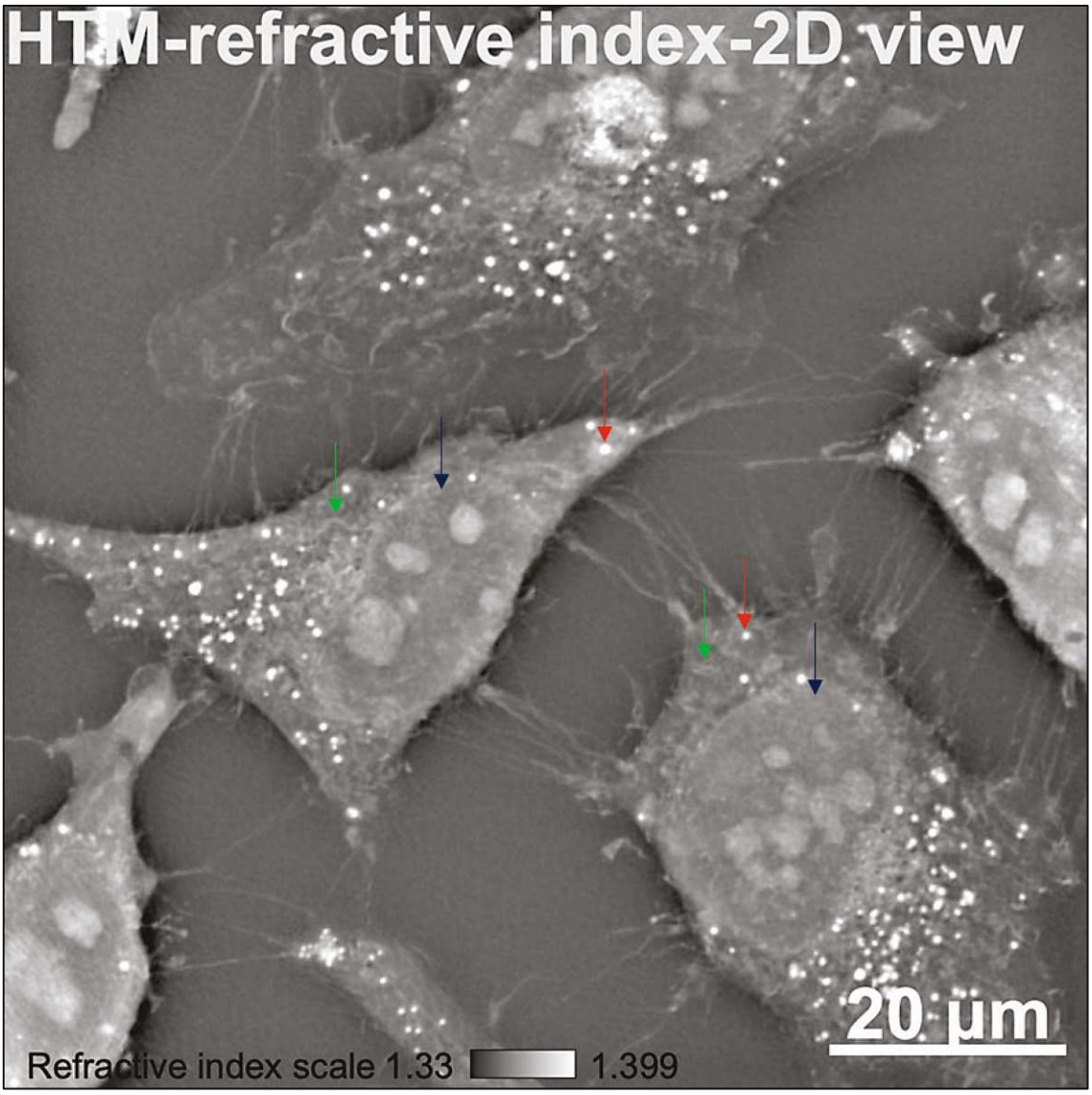

***Figure 1**: 2D RI map of unlabeled HeLa cells* (Sandoz et al., 2019; Fig. 1B).
The nuclei are indicated by the dark blue arrows and appear as large, distinct structures. Lipid droplets are marked with the red arrows and are clearly visible as bright spots due to their high RI. The mitochondrial networks are marked with the green arrows and appear as thin lines that are slightly brighter than the cytosol.

HTM has also been applied to diverse microorganisms, including bacteria (Buzalewicz et al., 2021), phytoplankton (S. Lee et al., 2014), insect cells (Shin et al., 2020) and yeasts (D. Lee et al., 2022; Odermatt et al., 2021). In bacteria, subcellular structures were not clearly distinguishable in the RI map, but a contrast between the cell wall and cytosol was evident (T. I. Kim et al., 2017). Challenges were encountered when applying HTM to yeasts due to their high RI value, which resulted in strong artifacts in the phase images. D. Lee et al. demonstrated that increasing the RI of the imaging media with iodixanol produced clear 2D phase images with visible subcellular structures for the yeast (D. Lee et al., 2022).

Given the absence of specific studies on filamentous fungi, the objective of this work is to apply HTM to filamentous fungi. The aim is twofold: firstly, to identify subcellular structures based on their RI and secondly, to explore the live-cell imaging capabilities of this technique on the filamentous fungus *Aspergillus niger*. The focus will be on morphological differences between a wild type and a citric acid production strain. Additionally, this study targeted the observation of nuclear dynamics and cellular events that may be associated with lateral branching mechanisms.

1.3. Filamentous fungi

Filamentous fungi comprise the majority of known fungal species. They grow by forming multicellular, tubular hyphae, which is why they are classified as filamentous fungi (Alexopoulos et al., 1996). As primarily saprophytic microorganisms, they play a vital role in ecosystems by breaking down various natural biopolymers. Filamentous fungi are capable of breaking down complex plant-derived polymers, such as cellulose and lignin, through the secretion of a variety of enzymes (El-Enshasy, 2007). These characteristics make them important decomposers. Some fungal species also have the ability to act as parasites or pathogens, infecting a wide range of plants and animals. In lichens, fungi act as mutualistic symbionts with bacteria or algae, providing a protected and moist environment in exchange for photosynthetically derived carbohydrates (Kendrick, 2011).

Filamentous fungi are highly attractive for industrial and biotechnological applications due to their exceptional enzymatic secretion capacity. However, their metabolic diversity results in the production of various organic acids, polysaccharides, plant growth regulators, alkaloids, pigments, and antibiotics, in addition to enzymes. Notably, filamentous fungi are not limited to enzyme secretion, making them intriguing hosts for the production of homologous and heterologous proteins, organic acids, antibiotics, and other secondary metabolites (El-Enshasy, 2007). Advances in bioengineering tools and process optimization have enhanced the potential for hyper-production and hyper-secretion (Meyer, 2021). Another advantage lies in the wide range of substrates filamentous fungi can utilize as carbon sources, including low-value options such as molasses (Grewal & Kalra, 1995) and abundant renewable resources like lignocellulose (Dörsam et al., 2017).

1.3.1. Fungal morphology

Efficient production of various products depends on understanding fungal morphology, which includes macro-morphology and micro-morphology. Macro-morphology involves interactions among many fungal cells, leading to pellet formation, for example. In contrast, micro-morphology focuses on the morphogenesis of individual fungal cells, including processes such as conidial swelling, germination, hyphal extension, and branching (El-Enshasy, 2007).

The morphogenesis of filamentous fungi occurs in three stages. The first stage is characterized by the dormant conidium or spore, which is characterized by high stress resistance to various environmental stressors, longevity, and a reduced metabolism. Recent studies have shown that the stage in which the conidium is still connected to the conidiophore plays a major role in adapting to changing environmental conditions. The resulting variability in phenotype ultimately enhances the survivability of the dormant conidium (F. Wang et al., 2021). The second stage is isotropic growth, which involves the swelling of conidia by the uptake of water and nutrients. This transition from dormancy to isotropic growth occurs under favorable conditions, requiring at least a carbon source and water. During this shift, a sudden change in the transcriptome towards protein biosynthesis, respiratory metabolism, and RNA turnover was reported (Novodvorska et al., 2013). The third stage, polarized growth, directs growth to one side of the cell, leading to the formation of germ tubes and later hyphae (Baltussen et al., 2020).

In the industrially most commonly used submerged cultivation, macro-morphology can range from compact pellets to dispersed mycelia. Although small pellets can enhance gas-liquid mass transfer in the bioreactor, optimal productivity is associated with larger and less dense pellets. However, increasing pellet size and density may limit internal substrate transport (Veiter et al., 2018). Furthermore, micro-morphological parameters, such as average hyphae length, diameter, and number of branches, can affect macro-morphological growth (El-Enshasy, 2007). As product secretion primarily occurs at hyphal tips, a hyperbranched micro-morphology with many short branches is desirable for optimal production (Meyer, 2021). In addition, short germination times and high germination efficiency are favorable for industrial applications (El-Enshasy, 2007).

Numerous factors influence macro- and micro-morphology, falling into three categories: strain-dependent factors, medium composition, and cultivation conditions. The preferred

macro-morphological characteristics vary depending on the strain and the product. For instance, pellet formation is favored for citric acid production by *Aspergillus niger*, while dispersed mycelium is preferred for enzyme production in the same organism (El-Enshasy, 2007).

Therefore, knowledge of how to control morphological parameters is crucial for industrial production. However, achieving a balance between optimal process control and production efficiency is usually necessary. Label-free 3D live-cell imaging can serve as a powerful tool for investigating fungal morphology, underscoring its significance in the context of this work.

1.3.2. Hyphal branching in filamentous fungi

The formation of hyphal branches is a crucial characteristic of filamentous fungi. Branching enhances the number of hyphal tips, enabling the fungus to quickly colonize new environments and thus maintain exponential growth (Trinci, 1984). Furthermore, branching is required for hyphal fusion events between different hyphae of the same colony, which enables the exchange of nutrients and signals within the colony (Harris, 2008). Hyphal tips are significant not only for the secretion of enzymes and other products but also for nutrient uptake and growth. An important element located at the hyphal tip is the Spitzenkörper that is composed of ribosomes, vesicles, and actin microfilaments. Previous research indicates that actin microfilaments serve as tracks for vesicle flow to and from the Spitzenkörper. The accumulated vesicles in the Spitzenkörper contain enzymes for cell wall synthesis and extracellular secretion, making it an essential component for hyphal extension, vesicle trafficking, and extracellular export (Harris et al., 2005; Riquelme & Sánchez-León, 2014).

Hyphal branching can generally be categorized into two types: apical and lateral branching. Apical branching occurs at the hyphal tip, while lateral branching starts from subapical compartments that are separated from the hyphal tip by at least one septum. It has been demonstrated that in *Neurospora crassa*, apical branching is accompanied by a deceleration of hyphal extension. This is followed by the disappearance of the Spitzenkörper, after which apical branches emerge from the hyphal tip, each with a newly formed Spitzenkörper. Apical branching is frequently observed in rapidly extending hyphae and it is presumably triggered by an increased vesicle flux to the hyphal tip (Riquelme & Bartnicki-Garcia, 2004).

Compared to apical branching, lateral branching mechanisms are less understood, although they are the predominant pattern in fungal hyphae. This process involves the formation of a

new Spitzenkörper in a subapical compartment, establishing a new polarity axis. Research has shown that lateral branching in *N. crassa* only occurs when the branching site is sufficiently distant from the hyphal tip. This observation suggests that the hyphal tip contains factors that inhibit lateral branching (Harris, 2008). Furthermore, a correlation was observed between nuclear number and branch frequency when comparing hypo- and hyper-branching mutants of *Aspergillus nidulans* with the wild type (Lin & Momany, 2004).

The framework for the regulation of branch formation proposed by Harris includes hyphal and compartmental level. On the hyphal level, apical dominance is maintained by reactive oxygen species (ROS) and Ca^{2+} which inhibits the formation of lateral branches. To link branch formation to hyphal growth, the protein kinase A and Target-of-Rapamycin pathways could act as signaling modules. On the compartmental level, the spatial and temporal occurrence of branch formation is presumably regulated by the individual hyphal cell. Events involved are most likely nuclear division and the establishment of a new polarity axis. Ultimately, septins and associated proteins stabilize and maintain the polarity axis and allow the formation of a new lateral branch (Harris, 2019).

However, the proposed framework includes assumptions and is generic. The complete mechanism underlying lateral branching, as well as important regulators, have not been fully revealed. Therefore, this work aims to observe visible events such as nuclear behavior during live-cell imaging potentially associated with lateral branching. Furthermore, the CDK $NimX^{Cdc2}$ of *A. niger* was targeted and investigated as it is known to play a significant role in regulating the cell cycle in filamentous fungi (Mcguire et al., 2000; Schier & Fischer, 2002).

1.3.3. *Aspergillus niger*

Aspergillus niger is a member of the Ascomycota phylum and is a significant fungal producer in industrial settings. It is well-known for its role in citric acid production since the early 20th century. James Currie identified *A. niger* in 1917 due to its exceptional citric acid productivity. Only two years later, industrial citric acid production with the fungus started (Cairns et al., 2018). *A. niger* exhibits rapid growth on low-cost materials, tolerates highly acidic environments, and produces high yields of citric acid, making it the preferred choice for industrial citric acid production. (Tong et al., 2019).

However, to maximize the yield, several factors must be considered. The carbon source must allow for rapid catabolism, and its concentration must be above 50 g/L to enable citric acid

accumulation. This is necessary to counteract the inhibitory effects of citrate on the enzyme phosphofructokinase 1 (PFK-1), which is a key enzyme in glycolysis. One way to bypass this inhibitory effect is through the accumulation of different positive effectors. Fructose-2,6-bisphosphate is the strongest activator of PFK-1. Previous work demonstrated that its intracellular concentrations increase when the fungus is exposed to high concentrations of sucrose or glucose. Another crucial factor is the concentration of trace metal ions, particularly Mn^{2+}. Limitation of Mn^{2+} is linked to various morphological changes, including a hyperbranched phenotype with many vacuoles and swollen, bulbeous hyphae. Although the positive impact of morphological changes on rheology and oxygen transfer is evident, the effect of Mn^{2+} deficiency on metabolism is not yet fully understood (Karaffa & Kubicek, 2003). A recent study revealed that Mn^{2+} ions inhibit the transcription of the *cexA* gene, which encodes the citrate exporter in *A. niger*. Furthermore, Reinfurt et al. demonstrated that overexpression of the citrate exporter can counteract the negative effect of Mn^{2+} on citric acid yield (Reinfurt et al., 2023). Other important factors for citric acid accumulation include a pH value below 3, an excess of oxygen and a balance between phosphate and nitrogen sources (Karaffa & Kubicek, 2003).

Beyond citric acid production, *A. niger* is extensively employed for enzyme production, ranging from individual enzymes such as glucoamylases and proteases to diverse enzyme mixtures facilitating the degradation of complex plant polysaccharides (Cairns et al., 2018). With the advent of genetic engineering tools, *A. niger* can also express recombinant, heterologous proteins. Despite the potential competition from bacteria or yeasts in terms of production efficiency, filamentous fungi offer specific advantages, such as the ability to produce large proteins with a lower degree of hyperglycosylation compared to yeasts (Ntana et al., 2020).

1.4. Plasmid construction via GoldenMOCS

Plasmid construction in this study employed Golden Gate Cloning (Engler et al., 2008, 2009; Weber et al., 2011), a well-established method facilitating the assembly of multiple DNA sequences. This technique utilizes type IIS restriction enzymes, such as BsaI and BbsI (also known as BpiI), which cleave DNA outside their recognition sites, creating DNA fragments with 4-base overhangs. These overhangs, termed fusion sites (FS), allow subsequent ligation into a recipient vector. Since the recognition sites are removed from the DNA fragments during assembly, no further cleavage occurs. Fusion sites enable the orderly assembly of multiple

sequences into vectors classified as BB1 (backbone 1), BB2, and BB3. BB1 contains a single insert (e.g., promoter, terminator, or coding sequence (CDS)), while BB2 represents an expression cassette composed of these individual parts. Multiple BB2 constructs (up to 8) can be ligated into a BB3 recipient vector. The enzyme BpiI is used for BB2 creation, while BsaI is employed for BB1 and BB3. Internal BsaI or BbsI recognition sites must be removed from DNA fragments by overlap-extension PCR which introduces a point mutation (Heckman & Pease, 2007). To guarantee gene expression and activity, point mutations in the CDS should maintain a normal or high codon usage in the host organism. The Golden Gate-derived Multiple Organism Cloning System (GoldenMOCS), developed by Sarkari et al., was used in this work. GoldenMOCS enables plasmid propagation in *E. coli* and subsequent transformation of the isolated plasmid into the target organism *A. niger* (Sarkari et al., 2017).

1.5. CRISPR/Cas

CRISPR, which stands for clustered regularly interspaced short palindromic repeat, is a crucial genome editing tool in molecular biology and biotechnology. Originally, it was part of the bacterial and archaeal immune system against viruses. The CRISPR-Cas system (Jinek et al., 2012) includes CRISPR regions separated by non-repeating spacer DNA sequences in the bacterial genome. Spacer sequences, which are obtained from viral genomes after infection, provide resistance. CRISPR-associated (Cas) genes, including Cas9, play a crucial role in proximity to CRISPR elements. Cas9, the catalytic protein in *Streptococcus thermophilus*, is guided by two short CRISPR RNAs (crRNA) transcribed from spacer sequences. The mature crRNA, along with a trans-activating crRNA (tracrRNA) or a single guide RNA (sgRNA), guides Cas9 to the target site. Protospacer-adjacent motifs (PAMs) on the foreign DNA, which are absent in the host DNA, are essential for Cas9 activity, preventing self-targeting. The CRISPR-Cas system operates in three stages: adaptation, crRNA biogenesis, and interference. During the adaptation stage, the system responds to invading genetic material and transcribes spacer sequences as pre-crRNA. In the crRNA biogenesis stage, the pre-crRNA is processed into mature crRNAs. Finally, in the interference stage, an RNA-Cas complex is formed that cleaves spacer-complementary sequences in foreign genetic material (Le Rhun et al., 2019).

The type II CRISPR-Cas9 system from *Streptococcus pyogenes* is widely used due to its simple NGG PAM sequence. This system enables targeting of almost any sequence through specific sgRNA design, resulting in double-strand DNA cleavage three base pairs before the PAM-site.

DNA repair occurs via non-homologous end joining (NHEJ) or homologous recombination, leading to gene knockout or integration of expression cassettes at a defined locus, respectively (Adli, 2018; Le Rhun et al., 2019).

1.5.1. CRISPR/Cas9 mediated integration of the expression cassettes at the *pyrG* locus

Homologous recombination at the *pyrG* locus was used to integrate the target DNA into the genome of the host organism A. niger in this study. The parent strain for transformation was provided by the lab, which had a *pyrG1* knockout generated through a CRISPR/Cas9-induced INDEL mutation. The plasmid used for transformation carried the expression cassettes and included the promoter region of the *pyrG* locus as a 5' homologous region, as well as the truncated and mutated *pyrG* gene under the control of the coxA promoter as a 3' homologous region. In addition, another plasmid containing the *Cas9* gene and the sgRNA was co-transformed.

The transcribed sgRNA, along with the *in-vivo* expressed Cas9, excises the expression cassette from its vector and the three base pairs 5' of the PAM site at the genomic *pyrG* locus via double-strand cleavage. The fungus' repair mechanism, activated by the double-strand break, undergoes homologous recombination, as a result of which the INDEL mutation is repaired and the expression cassettes are inserted. The resulting strain is capable of producing uridine, which is used as an auxotrophic selection marker. Hygromycin resistance, present on both plasmids, serves as an initial selection marker, along with uridine prototrophy. Clones displaying hygromycin sensitivity after two rounds of single colony isolation without hygromycin are selected, and successful cassette integration is confirmed through PCR verification (Sarkari et al., 2017).

2. Materials and Methods

2.1. Strains, media, and buffers

Competent *Escherichia coli* TOP10 cells were used for transformation and amplification of plasmid DNA. *Aspergillus niger* wild type ATCC 1015, the citric acid production strain ACIB1, *Trichoderma reesei* wild type QM6a Δtmus53, and *Aureobasidium pullulans* EXF-150 were used for HTM and staining procedures.

The *pyrG* deficient strains *A. niger* A621 (derived from ATCC 1015) and *A. niger* K621 (derived from ACIB1) were provided by the lab and used for transformation of plasmids, assembled by Golden Gate. Created plasmids and a complete list of modified strains used in this work are listed in the **Appendix**.

Media and buffers as well as chemicals, kits and devices used in the course of this work are also listed in the **Appendix**.

2.2. Plasmid construction

In-silico assemblies of the plasmids were performed using CLC Main Workbench software (Qiagen, Venlo, Netherlands). Plasmid construction was performed via Golden Gate Cloning (Sarkari et al., 2017). Backbone construction was performed in duplicates with a ligation control containing only the recipient vector but not the inserts. The reaction mix for each cloning step is given in **Table 1**. The incubation was performed for 45 cycles of restriction and ligation (37 °C, 5 minutes; 16 °C, 2.5 minutes) followed by 5 minutes at 50 °C and 10 minutes at 80°C. To reduce the number of re-ligated empty BBs, a re-digest was performed for 1 h at 37 °C by adding 0.4 µL of the appropriate restriction enzyme.

***Table 1**: Golden Gate cloning reaction mixture.*

Golden Gate cloning reagents	Stock concentration	Final concentration	Amount [µL]
Donor plasmid(s)	40 nM	2 nM	1
Recipient plasmid	40 nM	2 nM	1
rCutSmart™ Buffer	10x	1x	2
ATP	2 mM	200 nM	2
BpiI, 10 U/µL BsaI, 20 U/µL	10 U/µL 20 U/µL	1 U/µL 2 U/µL	2 1
T4 DNA ligase diluted 1:10 in T4 ligase buffer	100 U/µL	1.25 U/µL	2.5
ddH_2O			to 20 µL
Total volume			20

2.3. Transformation of *E. coli* and plasmid propagation

Plasmids were transformed into competent *E. coli* TOP10 cells that were provided by the lab. The Golden Gate mixture of 20 µL was added to 50 µL of the competent cells and then incubated on ice for 20 minutes. After a heat-shock for 2 minutes at 42 °C, 350 µL of SOC medium was added and cells were regenerated at 37 °C for 1 h. Transformed *E. coli* were plated on LB agar plates with an antibiotic selection marker and incubated o/n at 37 °C.

For plasmid extraction, pre-cultures of 3 mL LB media supplemented with the required antibiotic were prepared, each inoculated with a single colony from the transformation plate and cultivated o/n at 37 °C and 180 rpm. The plasmid DNA was extracted with HiYield® Plasmid Mini Kit according to the manufacturers' protocol. The correct plasmid assemble was confirmed by restriction digest of the extracted plasmid DNA with a suitable restriction enzyme. The reaction mixture is given in **Table 2**. The digest was performed at 37 °C o/n and the fragment sizes were then analyzed by agarose gel electrophoresis.

***Table 2**: Reaction mixture for the restriction digest.*

Restriction digest reagents	Stock concentration	Final concentration	Volume [µL]
Plasmid DNA			3
CutSmart buffer or NEBuffer 3.1	10x	1x	2
Restriction enzyme	20 U/mL	0.4 U/µL	0.4
ddH_2O			14.6
Total volume			20 µL

2.4. Agarose gel electrophoresis

For agarose gel electrophoresis, 1x TAE buffer was mixed with 0.8-1.4 % agarose and heated up until it dissolved. The amount of agarose used was depending on the size of the expected DNA fragment sizes. Midori Green was used as DNA stain. 0.005 % or 0.01 % were used for analytical and preparative gels, respectively. The gels were run for 40-60 minutes at 90 V and visualized using a ChemiDoc MP Imaging System.

2.5. Protoplast preparation and transformation of *A. niger*

Prior to the transformation, an o/n culture at 30 °C and 150 rpm of the strains A621 or K621 in complete medium (CM) supplemented with 10 mM uridine was harvested with a miracloth filter under sterile conditions and washed with 25 mL SMC. 0.5 g of the mycelium was

transferred to 10 mL lysing solution and incubated at 37 °C and 80 rpm for 2-2.5 hours if K621 was used, and 2.5-3 hours for A621. The formation of protoplasts was confirmed under the light microscope. Then, the protoplasts were released from the mycelium by pipetting up and down twice and subsequently filtered under sterile conditions with miracloth to remove residual mycelium. To enhance the protoplast yield, the filter was washed with 10 mL SMC. From this step on, the protoplasts were kept on ice. The samples were centrifuged at 2000 g and 4 °C for 10 minutes, washed with 1 mL of STC and centrifuged again at 3000 g and 4 °C for 5 minutes. The pellet was carefully resuspended in 100 µL STC for each transformation plate.

The plasmids were pipetted to the bottom of a sterile 50 mL tube and 100 µL of the protoplasts, 25 µL of PEG buffer, and lastly, 1 mL of PEG buffer were added. The solution was mixed by tapping the falcon followed by incubation of five minutes and then, 2 mL of STC was added. Subsequently, 25 mL of MMS top agar solution was poured to the transformation mixture. The tube was inverted a few times, and the mixture was then poured onto transformation plates. Incubation was performed at 30 °C for 7 days. Transformants were picked by a cotton swab that was dipped in Tween® 20 and transferred to selection plates (MM with 100 µg/mL hygromycin, referred to as V1). Positive clones were selected and transferred to MM selection plates without hygromycin, referred to as V2. This step was repeated once again (V3) and from the remaining clones 4-6 colonies were picked and transferred to MM plates and MM plates supplemented with hygromycin (100 µg/mL) to check the loss of hygromycin resistance. The genomic DNA (gDNA) of the positive clones was then extracted for PCR verification.

2.6. Extraction of genomic DNA

For the extraction of genomic DNA (gDNA) the Wizard Genomic DNA Preparation Kit (Promega, Madison, WI) was used. An o/n culture of the selected clones was prepared in 20 mL CM and the mycelium was harvested by filtration through a miracloth filter, washed with MQ H_2O and dried with paper towels. 100 mg of mycelium was incubated with 10 µL of 600 mg/mL lysing enzymes from *Trichoderma harzianum* in 290 µL 50 mM EDTA at 37 °C and 800 rpm for 90 minutes. The mixture was vortexed every 30 minutes. The samples were centrifuged at 16000 g for 7 minutes and the supernatant was discarded. 300 µL of nuclei lysis solution and subsequently 100 µL of protein precipitation solution was added to each sample and the mixture was incubated on ice for 5 minutes and centrifuged again at 16000 g for 7 minutes. The supernatant was transferred into a clean tube containing 300 µL isopropanol. The samples

were mixed by inverting and centrifuged at 16000 g for 2 minutes at RT. The DNA pellet was washed with 300 µL of 70% ethanol and centrifuged again with the same conditions. The supernatant was removed, and the pellet was dried at 37°C until the ethanol evaporated. Then, 50 µL of DNA rehydration solution and 1.5 µL of RNase were added and incubated at 37°C for 15 minutes, followed by another 15 minutes at 60°C. The concentration and purity of the gDNA was determined using Nanodrop™ One.

2.7. PCR verification

To verify the integration of expression cassette(s) into the *A. niger* genome, PCR was performed. PCR 1 spanned the area from the 5' prime region of the recombination site to the Tet-On promoter or sGFP sequence. PCR 2 reaches from the terminator sequence (*trpC)* to the 3' prime region of the truncated *pyrG*. PCR 3 spanned the whole expression cassette including the 5' and 3' prime region of the recombination sites. The analytical PCRs were performed as shown in **Table 8** and **Table 9**. A negative control with water instead of gDNA as well as a second control containing gDNA from the wild type ATCC 1015 was prepared for each PCR.

2.8. RNA extraction and cDNA synthesis

For the cDNA synthesis, the RNA was extracted from mycelium of *A. niger* ATCC 1015 cultivated o/n at 30°C and 150 rpm. The mycelium was harvested by filtration through a miracloth filter, washed with dH_2O and dried with paper towels. 100 mg of the mycelium was placed into a screw cap tube containing 0.25 mg of glass beads with 0.1 mm and 1 mm in diameter and 1 mL RNAzole. The mycelium was disrupted using FastPrep-24 for 3 cycles of 6 m/s for 20 s. RNA extraction was the performed with the innuPREP RNA Mini Kit 2.0 according to the manufacturers' protocol. Elution was performed using 50 µL RNase-free water after incubation for 1 minute at RT. The RNA concentration of the extract was determined using NanoDrop™ One.

To remove gDNA, the RNA extract was treated with DNase I. The reaction mix is given in **Table 3**. DNase digest was performed for 30 minutes at 37°C. Then 1 µL of 50 mM EDTA was added and incubated at 65°C for 10 minutes.

Table 3: Reaction mixture for DNase digest of the RNA extract.

DNase digest reagents	Stock concentration	Final concentration	Amount
RNA extract			2 µg
10X reaction buffer with $MgCl_2$	10x	1x	1 µL
DNase I	1000 U/mL	0.1 U/µL	1 µL
DEPC-treated water			To 10 µL
Total volume			10 µL

To assess the quality of the RNA extraction, an agarose gel electrophoresis was performed using 1, 0.5 and 0.2 µg of RNA extract for loading. High quality RNA is characterized by three distinct bands representing ribosomal RNA (Aranda et al., 2012). The samples and the RiboRuler RNA Ladder were mixed with an equal volume of 2x RNA Loading Dye and then incubated at 70°C for 10 minutes.

The DNase digested RNA extract was further used for first strand cDNA synthesis with the RevertAid First Strand cDNA Synthesis Kit (ThermoFisher Scientific, Waltham, MA). The reagents used can be seen in **Table 4**. The mixture was incubated for 60 minutes at 42°C, followed by 5 minutes at 70°C. Together with the two RNA samples, a negative control containing no template RNA, a positive control containing GAPDH RNA and specific primers as well as two reverse transcriptase minus negative controls, containing all reagents except the reverse transcriptase were performed.

Table 4: Reaction mixture for first strand cDNA synthesis.

First strand cDNA synthesis reagents	Stock concentration	Final concentration	Amount [µL]
Template RNA			5 (corresponds to 1 µg)
Oligo$(dT)_{18}$ primer	0.5 µg/µL	0.025 µg/µL	1
Water, nuclease free			6
Reaction buffer	5x	1x	4
RiboLock RNase inhibitor	20 U/µL	1 U/µL	1
dNTP mix	10 mM	1 mM	2
RevertAid H Minus M-MulV Reverse Transcriptase	200 U/µL	10 U/µL	1
Total volume			20

2.9. Preparation of DNA fragments for fusion PCR and subsequent Golden Gate cloning

To generate DNA sequences for fusion PCR and subsequent Golden Gate cloning, the cDNA of *A. niger* ATCC 1015 was used as template. PCRs were performed to add the correct FS at the 5' and 3' prime region of the CDS and to remove internal BsaI and BpiI cleaving sites. Received fragments were subsequently fused by fusion PCR. The target sequences were coding for the structural protein α-tubulin and the cyclin-dependent kinase (CDK) NimX^{Cdc2}. For the sGFP CDS, no fusion PCR was required. Only the correct FS was added as the CDS was provided by the lab. The primers 10-27 were used and can be found in the **Appendix**.

For α-tubulin and NimX^{Cdc2} three different PCRs, and for the sGFP a single PCR were performed. The PCR products were loaded onto a preparative agarose gel to confirm their size and to remove the primers. The gel was extracted with the Hi Yield® Gel/PCR DNA Fragment Extraction Kit according to the manufacturers' protocol. The concentration of the purified DNA fragments was determined with Nanodrop™ One.

The three fragments of α-tubulin and NimX^{Cdc2} were then each used for a fusion PCR. In total, 2 pmol of each fragment was used as template. The reaction mix is shown in **Table 5**. Before adding the primers, the PCR program 1 was run. The primer annealing temperature was calculated with NEB T_m calculator. The primers were then added, and program 2 was run. The programs can be seen in **Table 6** and **Table 7**.

***Table 5**: Reaction mixture for the fusion PCR. Primers were added after program 1.*

Fusion PCR reagents	Stock concentration	Final concentration	Amount [µL]
Q5 buffer	5x	1x	10
dNTPs	10 mM	200 µM	1
Q5 polymerase	20 U/µL	0.2 U/µL	0.5
Primer forward	10 µM	500 nM	2
Primer reverse	10 µM	500 nM	2
ddH_2O			Up to 50
Template DNA		0.04 pmol	
Total volume			50

***Table 6**: Program 1 used for the first step of the fusion PCR.*

Temperature [°C]	Time [s]	Step	
98	30	Initial denaturation	
98	10	Denaturation	Repeat 9x
Variable	30	Primer annealing	
72	30/kb	Elongation	

Table 7: Program 2 used for fusion PCR after addition of the primers.

Temperature [°C]	Time [s]	Step	
98	30	Initial denaturation	
98	10	Denaturation	Repeat 30x
Variable	30	Primer annealing	
72	30/kb	Elongation	
72	600	Final elongation	

The PCR products were then loaded on a gel, the correct band was excised, and a gel extraction was performed. The concentration was determined with Nanodrop™ One. The modified CDS, contained no restriction sites but appropriate FS and were then used for BB1 construction. The sGFP was fused to the CDS during the first Golden Gate cloning step and not via fusion PCR.

2.10. Preparative and analytical PCRs

Preparative and analytical PCRs were performed with Q5 Polymerase. The reaction mixture for one PCR approach is given in **Table 8** and the PCR program in **Table 9**. The primer annealing temperature was calculated with NEB T_m calculator. For preparative PCRs, a total volume of 50 µL was used with the same ratios. Used primers are listed in the **Appendix**.

Table 8: Reaction mixture for one analytical PCR approach.

PCR reagents	Stock concentration	Final concentration	Amount [µL]
Q5 buffer	5x	1x	5
dNTPs	10 mM	200 µM	0.5
Q5 polymerase	20 U/µL	0.2 U/µL	0.25
Primer forward	10 µM	500 nM	1.25
Primer reverse	10 µM	500 nM	1.25
ddH_2O			16.25
DNA	100-1000 ng/µL	2-20 ng/µL	
Total volume			25

Table 9: Standard PCR program used for Q5 polymerase.

Temperature [°C]	Time [s]	Step	
98	60	Initial denaturation	
98	20	Denaturation	Repeat 35x
Variable	20	Primer annealing	
72	30/kb	Elongation	
72	360	Final elongation	

2.11. Cell wall digestion of *A. niger*

Cell wall digest and subsequent imaging was performed with the engineered strains expressing the histone H2A tagged with sGFP. Protoplast preparation was performed as described in **2.5.** For the cell wall digest of the hyphae, *A. niger* was cultivated o/n in 20 mL MM supplemented with 1 µg/mL doxycycline in a Petri dish. Mycelium was then transferred to a 50 mL falcon containing 10 mL lysing solution supplemented with 1 µg/mL doxycycline. It was then incubated at 37 °C and 80 rpm for 3 hours. Liquid MMS was used as imaging medium to counteract the osmotic pressure.

2.12. Cultivation for microscopy and sample preparation for holotomographic imaging

A. niger strains were cultivated on MM plates for 7 days at 30°C. *T. reesei* was cultivated on MEX plates for 3 days at 30°C followed by 3 days at RT for sporulation. Conidia were harvested with a 0.1% Tween® 20 solution, filtered under sterile conditions with miracloth and centrifuged at 2600 g for 10 minutes. *A. pullulans* was cultivated on MEX plates for 7 days at RT and cells were suspended in a Tween®/NaCl solution (0.05% Tween® 80 (v/v) and 0.8% NaCl). Cells or conidia concentration was determined with a Thoma cell counting chamber using either 1:10 or 1:100 dilutions of the suspension.

Two different approaches were used for HTM. Imaging of modified strains and stained cells to identify subcellular structures was performed without time-resolution. Therefore, a microscope slide and a coverslip with mycelium in between were used. For each sample, 20 mL liquid medium was inoculated with 10^5 conidia of *A. niger*, *T. reesei* or $2.5*10^5$ cells for *A. pullulans* in a Petri dish. Coverslips were mounted on the bottom and incubated o/n at 30 °C. The coverslips were then placed on an object slide and subsequent imaging was performed with the 3D Cell Explorer-fluo (Nanolive SA, Tolochenaz, Switzerland).

For time-resolved imaging, ibidi® µ-Dishes (ibidi GmbH, Gräfelfing, Germany) with a coated polymer bottom for cell adhesion were used. Ibidi® µ-Dishes with glass bottom were used for optimization of the live-cell imaging protocol. In the optimized protocol, $3.3*10^5$ conidia were seeded in 500 µL culture medium for 1 hour at RT. Subsequently, the conidia were washed three times with 1 mL medium to remove floating cells. Imaging was started with 1.5 mL of fresh medium.

2.13. Staining methods

2.13.1. Staining of lipid droplets

For the staining of lipid droplets, Nile Red was used. The stock solution was prepared with a concentration of 0.5 mg/mL Nile Red in acetone. The coverslips that were incubated o/n as described previously, were washed three times with 10 mL phosphate buffered saline (PBS). The stock solution was diluted 1:100 in PBS to achieve a working solution with a concentration of 5 µg/mL Nile Red. 10 mL of the working solution was added to the coverslips in a Petri dish and incubated in the dark at RT for 5 minutes. It was washed again three times with PBS and the coverslips were placed on object slides for imaging.

2.13.2. Staining of mitochondria

For staining of mitochondrial networks, MitoTracker™ Deep Red FM was used. The MitoTracker™ stock was prepared by adding 20 µL DMSO to the vial. The overgrown coverslips were washed three times with PBS buffer. The working solution was prepared by diluting the stock solution 1:1000 in PBS. 10 mL of the working solution was used for staining and incubated in a Petri dish in the dark at 37°C for 35 minutes. The coverslips were washed again three times with PBS and then placed on object slides for imaging.

2.13.3. Staining of vacuoles

5(6)-Carboxy-2',7'-dichlorofluorescein diacetate (CDCFDA) was used for staining the lumen of the vacuoles. The stock solution was prepared with a concentration of 3 mM in DMSO. Staining was performed without washing the cells. 20 mL MM containing 50 mM sodium citrate at pH 4 and 20 µL CDCFDA stock solution were added to the coverslips in a Petri dish to achieve a final concentration of 3 µM CDCFDA. Incubation was performed in the dark at RT for 30 minutes and subsequently the coverslips were washed three times with 20 mL of the MM containing 50 mM sodium citrate. Each wash step was performed for 10 minutes in the dark at RT and the coverslips were then placed on object slides for imaging.

2.13.4. Staining of nuclei

Nuclei staining was performed with NucBlue™ Live ReadyProbes™ Reagent. Four drops of the reagent were added to the cultivation medium (MM supplemented with 1 µg/mL doxycycline) containing the coverslips and incubated in the dark at RT for 30 minutes. The coverslips were then washed three times with PBS buffer and placed on object slides for imaging. Fluorescence

imaging was performed with the epifluorescence microscope Leica DMi8 (Leica Camera, Wetzlar, Germany).

2.14. Holotomographic microscopy and data processing

HTM was performed with the 3D Cell Explorer-fluo using the software Steve (Nanolive SA, Tolochenaz, Switzerland). The microscope was used to record stacks of holotomographic slices. Additional fluorescence imaging was performed with the 3D Cell Explorer-fluo or the Leica DMi8. The corresponding excitation and emission maxima of the fluorophores used, and the fluorescence channels used are listed in **Table 10**. For time resolved imaging, a stack of holotomographic slices was recorded every two minutes. If additional fluorescence imaging was required, it was performed every four minutes. The raw data was processed in Fiji (2.9.0; Schindelin et al., 2012). Images were displayed either as single holotomographic slices or as maximum intensity projection of holotomographic slices. For detailed information on data processing, the SOP written in the course of this work, is attached as online material. The link can be found in the **Appendix**. Statistical calculations were performed using a two-tailed *t*-test. Differences were deemed statistically significant when $p < 0.05$.

***Table 10**: List of used fluorophores, their excitation and emission maxima and the used fluorescence channel of the microscope.*

Fluorophore	Fluorescence Channel/Microscope	Excitation/Emission maxima [nm]
sGFP	FITC/3D Cell Explorer-fluo GFP/Leica DMi8	488/510
Nile Red	TRITC/3D Cell Explorer-fluo	515/585
MitoTracker™	Cy5/3D Cell Explorer-fluo	644/665
CDCDFA	FITC/3D Cell Explorer-fluo	504/529
NucBlue™	Y5-T/Leica DMi8	360/460

3. Results

The overall aim of this thesis was to examine the applicability of HTM on fungi. The focus was on the filamentous fungus *A. niger* of which the wild type ATCC 1015 and the citric acid production strain ACIB1 were investigated. To achieve this goal, an optimized protocol for live-cell HTM for fungi had to be established first. In addition, staining of subcellular structures was performed to see if identification based on characteristic RI patterns was possible by superimposing the fluorescence signal on the RI map. Furthermore, live-cell imaging experiments with *A. niger* were conducted to investigate growth and morphology, nuclear dynamics and the CDK NimX^{Cdc2}.

3.1. Projection methods for HTM data

Image acquisition by HTM results in a series of 2D holotomograms (2D RI maps), each representing an XY plane of the specimen, also called a slice. This stack of slices can then be used by the microscope software to generate a 3D RI map, as shown in **Fig. 2A**. In addition, image processing in Fiji (Schindelin et al., 2012) can be used to generate a z-projection of the holotomographic slices containing relevant information (**Fig. 2B**). The resulting 2D image contains the most relevant information from each slice, provided that an appropriate projection method is used. The appropriate projection type generally depends on the type of data. This work presents data from HTM using either single holotomographic slices or a maximum intensity z-projection of holotomographic slices.

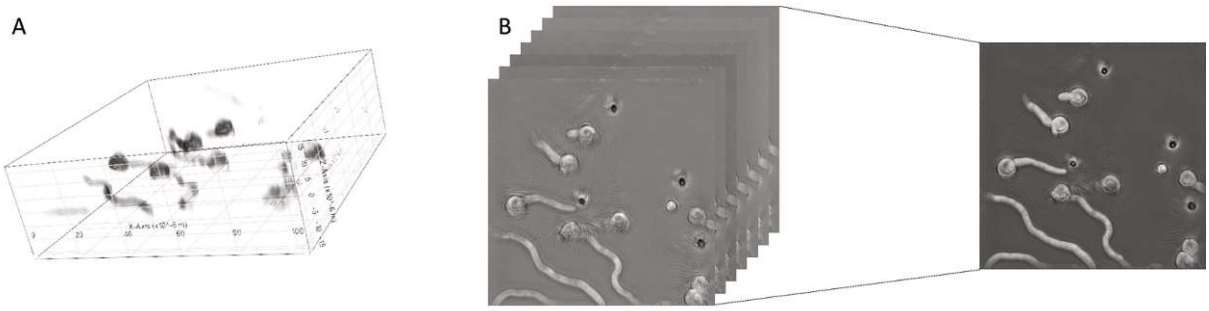

***Figure 2**: Different projection methods for the 2D holotomographic slices.*
Data shown is from the *Aspergillus niger* wild type ATCC 1015 cultivated in MM. **(A)** 3D RI map generated from 2D holotomographic slices by the software Steve (Nanolive SA, Tolochenaz, Switzerland). **(B)** Schematic view of generation of a maximum intensity projection from selected 2D holotomographic slices (left: seven single slices; right: maximum intensity projection of these seven slices).

3.2. Optimization of the live-cell HTM protocol for fungi

At the beginning of working with HTM on fungi, a difference in image quality was observed between using microscope slides versus the ibidi® µ-Dish used for live-cell imaging. Fine details such as bright dots, later identified as lipid droplets, as well as demarcated lighter and darker areas were not visible during live-cell imaging with the ibidi® µ-Dishes. Therefore, the parameters affecting the image quality were determined in order to create an optimized protocol for live-cell HTM on fungi.

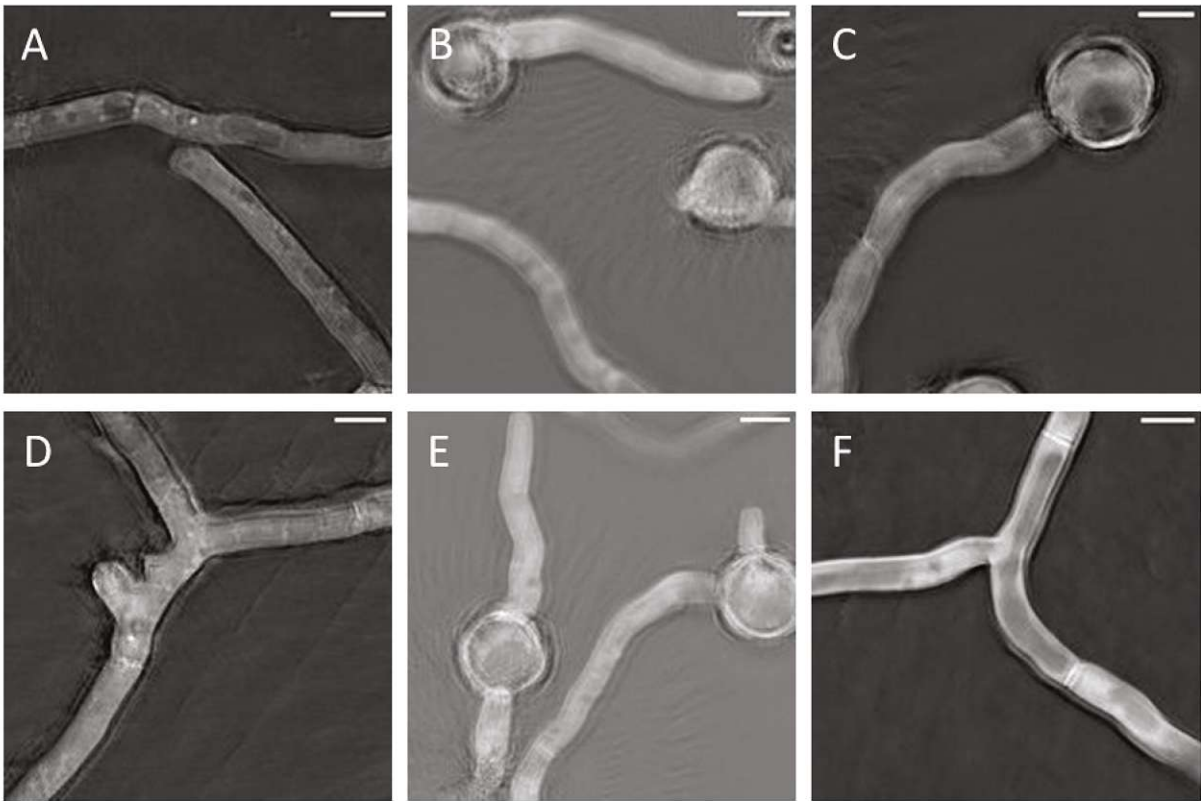

***Figure 3**: Images of the resolution tests for the optimization of the live-cell HTM protocol.*
Images show the *A. niger* wild type ATCC 1015, cultivated in MM, with the exception of image C. All images show a holotomographic slice. **(A)** Image of the fungus between object slide and coverslip. **(B)** Image after 10h of live-cell imaging in an ibidi® µ-Dish. The holotomographic slice displayed is not at the focal point. **(C)** Image of the engineered strain A621_H2A:sGFP cultivated in MM and induced with 1 µg/mL doxycycline. The image was taken after 10h of cultivation in an ibidi® µ-Dish. The holotomographic slice shown represents the precise focal point. **(D)** Only 500 µL culture medium was used and a coverslip was placed above the liquid surface. Cultivation was performed o/n and culture medium was then transferred to an ibidi® µ-Dish. **(E)** Image after 10h of live-cell imaging in an ibidi® µ-Dish with glass bottom. **(F)** Image after 20h of live-cell imaging in an ibidi® µ-Dish with glass bottom. Only 500 µL culture medium was used and a coverslip was placed above the liquid surface. The microscope was placed on a balance table. Scalebar: 5 µm.

In **Figure 3**, different images of *A. niger* are shown including a reference image (**A**) using a microscope slide and two example images (**B**, **C**) for the time-resolved imaging. All displayed images represent a single holotomographic slice, and therefore a 2D RI map. This projection type typically provides the highest resolution, although it only includes data from a two-dimensional plane. The reference image in **Fig. 3A** shows the wild type strain ATCC 1015

between a microscope slide and coverslip. Many details are visible, including brighter dots and darker areas that are clearly separated from the surrounding cytosol. These indicate higher and lower RIs, respectively. Additionally, the hyphae and other visible structures exhibit sharp edges. The first example image in **Fig. 3B** also displays the ATCC 1015 strain, but after 10 hours of cultivation in an ibidi® µ-Dish. None of the aforementioned details are visible and the edges of the hyphae are blurry. However, the holotomographic slice shown is below the focal point. This shift in the focal plane frequently occurred during live-cell imaging, either due to growth in the z-axis or due to focus drift. For comparison, the second example image in **Fig. 3C** depicts a holotomographic slice at the precise focal point. The image shows the engineered strain A621_H2A:sGFP after 10 hours of cultivation in an ibidi® µ-Dish. Compared to **Fig. 3B**, it is generally less blurred and details such as some brighter dots, a septum recognizable as bright line and darker areas are visible. However, only the septum is clearly demarcated among these structures.

The importance of the focal point is highlighted in these images. However, the goal was to achieve the same image resolution as shown in **Fig. 3A** during live-cell imaging. Therefore, several other factors were considered as potential contributors to image quality. The initial protocol already included sterile filtering of the cultivation medium. In addition, sterile filtering of the Tween® 20 solution, used for preparation of conidia suspensions, was added. To remove floating conidia from the medium, a seeding and washing step prior to imaging was added as well.

Furthermore, it was assumed that both the water surface and the amount of medium may have an impact on the image quality. Therefore, the media amount was reduced to 0.5 mL from the initial 1.5 mL and a coverslip was placed on the liquid surface. As cultivation under these conditions was challenging in terms of oxygen supply and medium evaporation, the culture medium was transferred to an ibidi® µ-Dish after o/n cultivation in a Petri dish. **Fig. 3D** displays an image of this experiment using the ATCC 1015 strain. Some well demarcated brighter dots and septa are visible. In addition, the image is less blurry compared to image **C**. However, the background is not clear and separated darker areas, as seen in the reference image (**A**), are not visible.

An additional experiment was conducted with the same strain using an ibidi® µ-Dish with a glass bottom instead of a coated polymer bottom. According to the manufacturer, the highest

resolution is typically achieved with the glass bottom culture dishes. The resulting image after 10 hours of cultivation is shown in **Fig. 3E**. Some darker areas and a septum are visible. However, the image is still blurred and there is no significant improvement in its resolution compared to image **C**.

In a final attempt, all of the aforementioned factors were considered. This involves using an ibidi® µ-Dish with a glass bottom and a medium volume of 0.5 mL with a coverslip placed above the liquid surface. Additionally, the microscope was placed on a balance table to eliminate any minor vibrations. The same strain was used and time-lapse HTM was performed. As no hyphae grew in the field of view, the image was taken on the next day after 20 hours of cultivation. The resulting image is displayed in **Fig. 3F**. Septa as well as lighter and darker areas are visible. In addition, the hyphae exhibit sharp edges. However, none of the bright dots visible in **Fig. 3A** are present. In general, the hyphae in this image look different compared to the other images, probably because of the longer cultivation time.

The final experiment was not repeated due to the cultivation difficulties mentioned earlier. The coverslip covering most of the gas/liquid interface caused limited oxygen supply. Additionally, evaporation still had a stronger impact on the media composition as the total medium volume was lower. Thus, this approach was deemed unsuitable for live-cell HTM.

In summary, the optimized protocol for live-cell HTM included the usage of sterile filtered media and Tween® 20 solution, as well as a seeding and washing step prior to imaging. Ibidi® µ-Dishes with coated polymer bottoms and a media volume of 1.5 mL, as recommended by the manufacturer, were used for imaging. The microscope was kept on the balance table, and the initial inoculation density of $1*10^6$ conidia per 1.5 mL of medium was adjusted to the seeding step. The protocol can be found in the **Materials and Methods** section.

3.3. Identification of subcellular structures in holotomographic images

The aim of this study was to assign subcellular structures including lipid droplets, mitochondria, nuclei, proteins and vacuoles to a specific RI pattern generated by HTM. Therefore, structures such as lipid droplets, vacuoles and mitochondria were visualized by staining. In addition, a GFP-tag was used to visualize proteins including the histone H2A and α-tubulin. The fluorescence signal of the dye or the GFP-tag was superimposed on the holotomographic image to identify specific patterns. The *A. niger* wild type ATCC 1015 as well as the citric acid production strain ACIB1, *A. pullulans* and *T. reesei* were investigated. *T. reesei*

was only examined in one experiment, in which the organism was found to be too small for the resolution capabilities of the microscope. *A. pullulans* was chosen for this experiment because of its phenotypic plasticity, which results in different morphologies ranging from yeast-like cells to filamentous growth, depending on the cultivation conditions. (Slepecky & Starmer, 2009). Therefore, *A. pullulans* was cultivated in MM and MEX to obtain different morphologies. However, the results showed that there was no clear difference in morphology between the media used, hence only images of MEX are depicted. In the following chapter, microscope slides and cover slips were used for imaging.

3.3.1. Lipid droplets

Lipid droplets have a much higher refractive index compared to the cytosolic environment (Chen et al., 2021). Therefore, they are expected to be visible in the RI map as brighter dots. Staining was performed with Nile Red which targets neutral lipids commonly found in lipid droplets (Diaz et al., 2008).

In **Figure 4**, images of the *A. niger* wild type ATCC 1015 cultivated in MM are depicted. **Fig. 4A** shows a holotomographic slice, while **Fig. 4B** shows the corresponding fluorescence signal of the dye. **Figure 5** shows a zoomed section of these images. Some of the lipid droplets that were identified due to the fluorescence signal are visible in the RI map as brighter dots. Especially the bigger droplets that show also a more intense fluorescence signal are visible by holotomography. However, **Fig. 4A** represents only a single holotomographic slice, thus some of the lipid droplets may not be located in the depicted slice and are therefore not visible in the RI map.

Figure 6 shows images of *A. pullulans* wild type EXF-150 cultivated in MEX. **Fig. 6A** shows a holotomographic slice and **Fig. 6B** the corresponding fluorescence signal of the lipid dye. Lipid droplets are visible in the fluorescence image. However, in the holotomographic slice none of the droplets appear as bright dots.

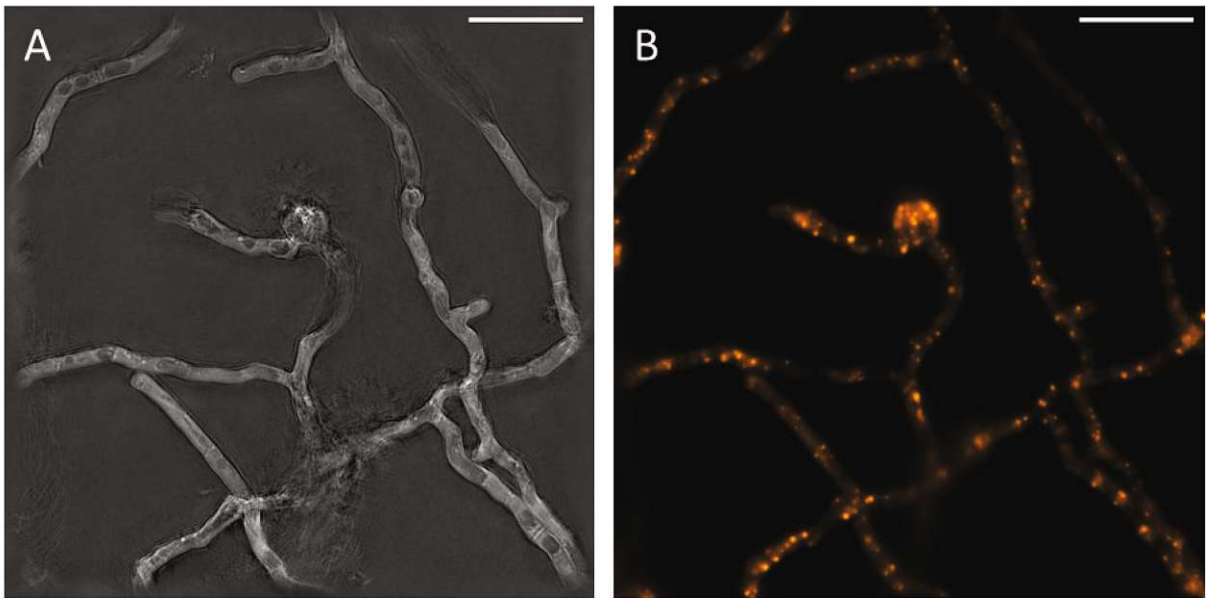

***Figure 4**: Images of A. niger strain ATCC 1015 cultivated in MM and stained with Nile Red.*
(A) Holotomographic slice. **(B)** Fluorescence signal of the dye, colorized. Scalebar: 20 µm.

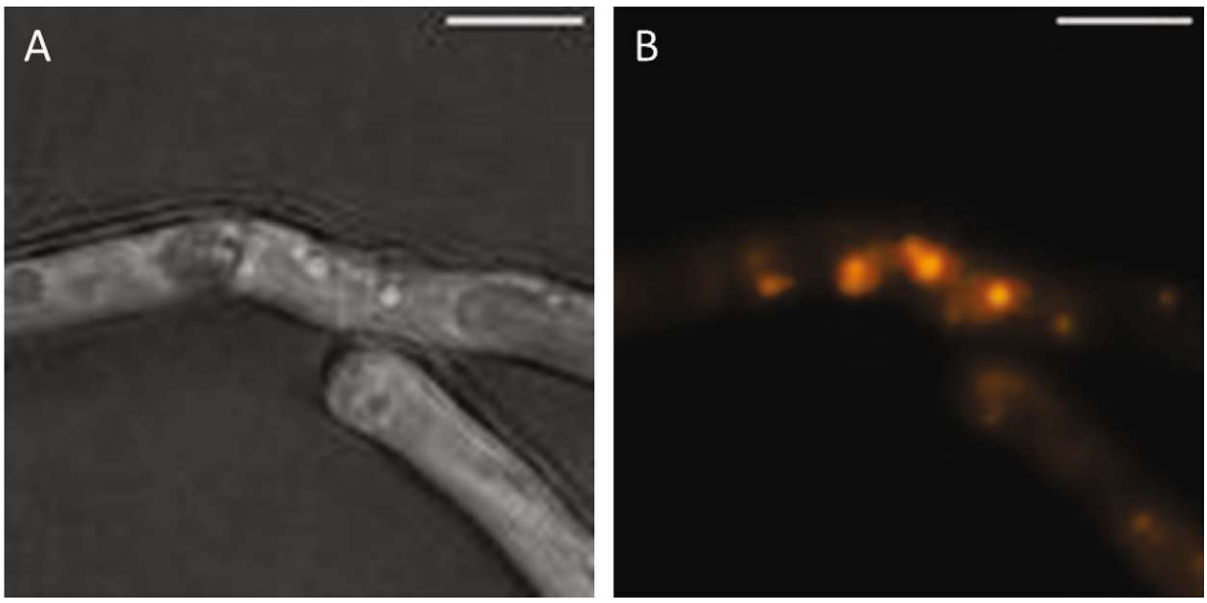

***Figure 5**: Zoomed section of the images shown in **Figure 4**.*
(A) Holotomographic slice. **(B)** Fluorescence signal of the dye, colorized. Scalebar: 5 µm.

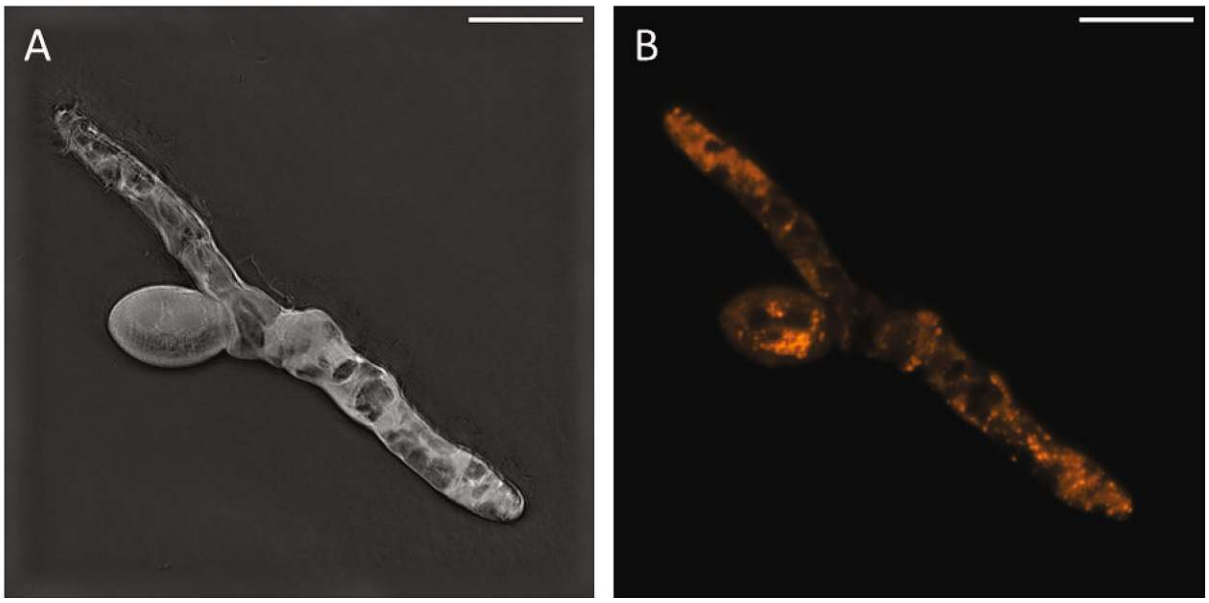

***Figure 6**: Images of A. pullulans strain EXF-150 cultivated in MEX and stained with Nile Red.*
(A) Holotomographic slice. **(B)** Fluorescence signal of the dye, colorized. Scalebar: 20 µm.

3.3.2. Vacuoles

Vacuoles were stained with CDCFDA which targets the lumen of the vacuole (Peñalva, 2005). As described by Park et al., vacuoles have a lower refractive index compared to the cytosol (Park et al., 2008). Therefore, vacuoles are expected to appear as darker spots in the RI map.

In **Figure 7**, images of the *A. niger* wild type ATCC 1015 cultivated in MM are shown. **Fig. 7A** shows a holotomographic slice, while **Fig. 7B** shows the corresponding fluorescence signal of the dye. The two darker spots marked with red arrows in **Fig. 7A** match with the signal of the dye in **Fig. 7B**. However, smaller vacuoles that are visualized by staining are hard to detect in the RI map. An example is marked with a green arrow.

Figure 8 shows images of the citric acid production strain ACIB1 cultivated in VM. This strain was chosen as its micro-morphology differs from the wild type. The nutrient rich VM was utilized to simulate the conditions of citric acid production. In addition, effects on morphology were expected when using different media. **Fig. 8A** shows a holotomographic slice, while **Fig. 8B** shows the corresponding fluorescence signal of the dye. In contrast to the wild type in **Figure 7**, more vacuoles that are confirmed by the fluorescence image are visible in the RI map.

In **Figure 9**, images of *A. pullulans* strain EXF-150 cultivated in MEX is shown. **Fig. 9A** shows a holotomographic slice, while **Fig. 9B** shows the corresponding fluorescence signal of the dye. All vacuoles visualized by staining appear as clearly distinct, dark areas in the RI map.

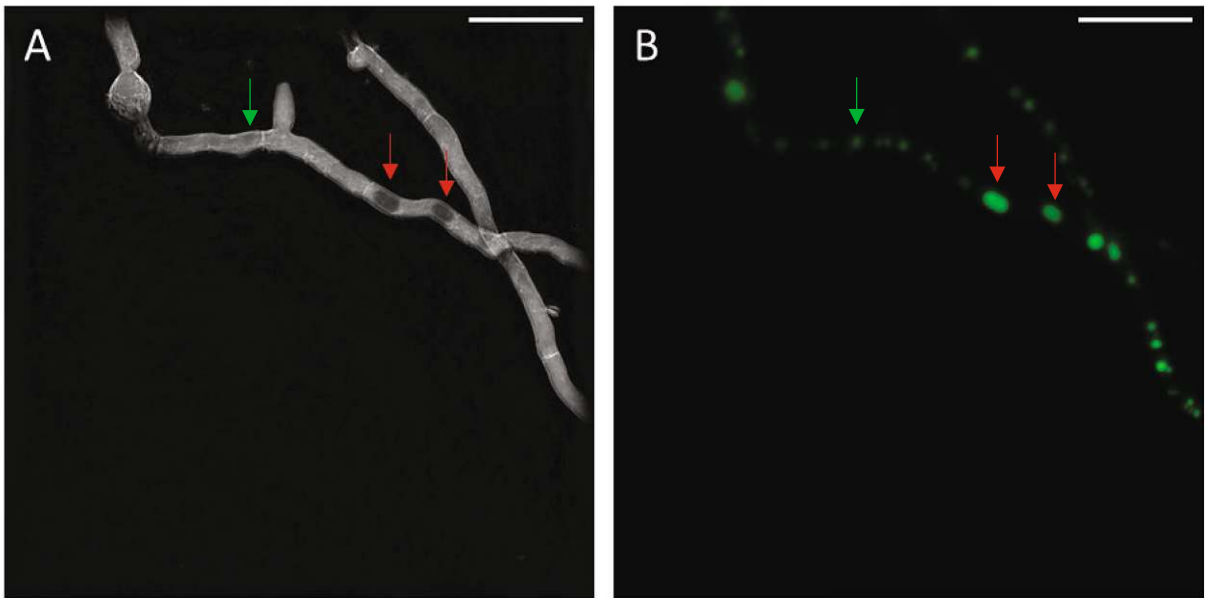

***Figure 7**: Images of A. niger strain ATCC 1015 cultivated in MM and stained with CDCFDA.*
(A) Holotomographic slice. **(B)** Fluorescence signal of the dye, colorized. Red arrows mark vacuoles that are clearly visible in the holotomographic slice. The green arrow indicates the position of a small vacuole, that is hardly visible in the holotomographic slice. Scalebar: 20 µm.

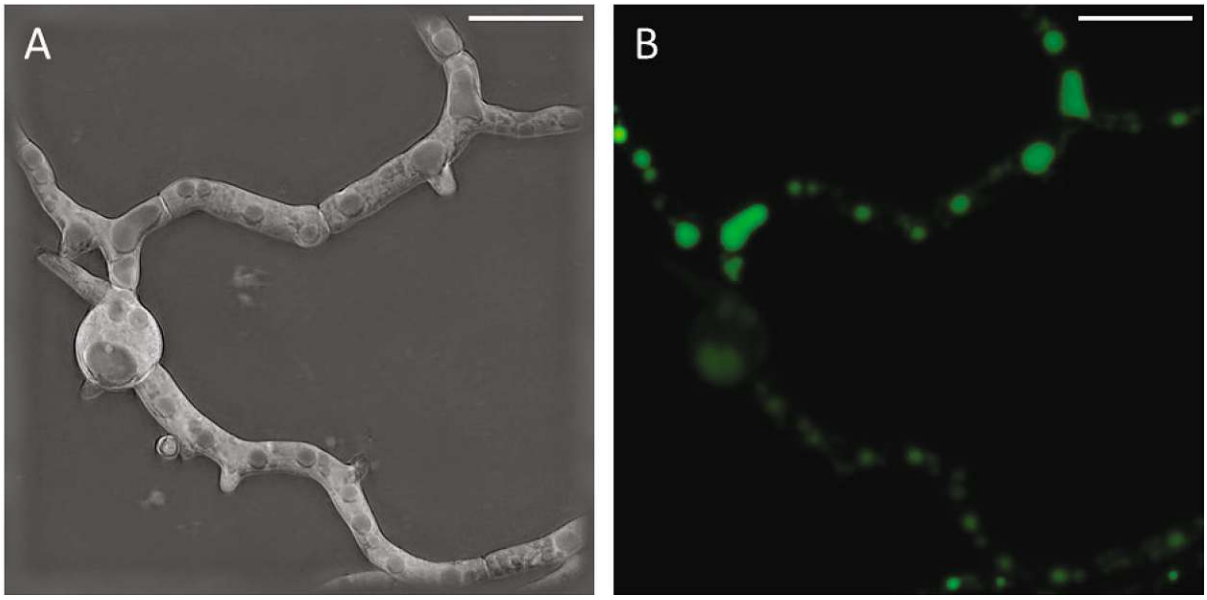

***Figure 8**: Images of A. niger strain ACIB1 cultivated in VM and stained with CDCFDA.*
(A) Holotomographic slice. **(B)** Fluorescence signal of the dye, colorized. Scalebar: 20 µm.

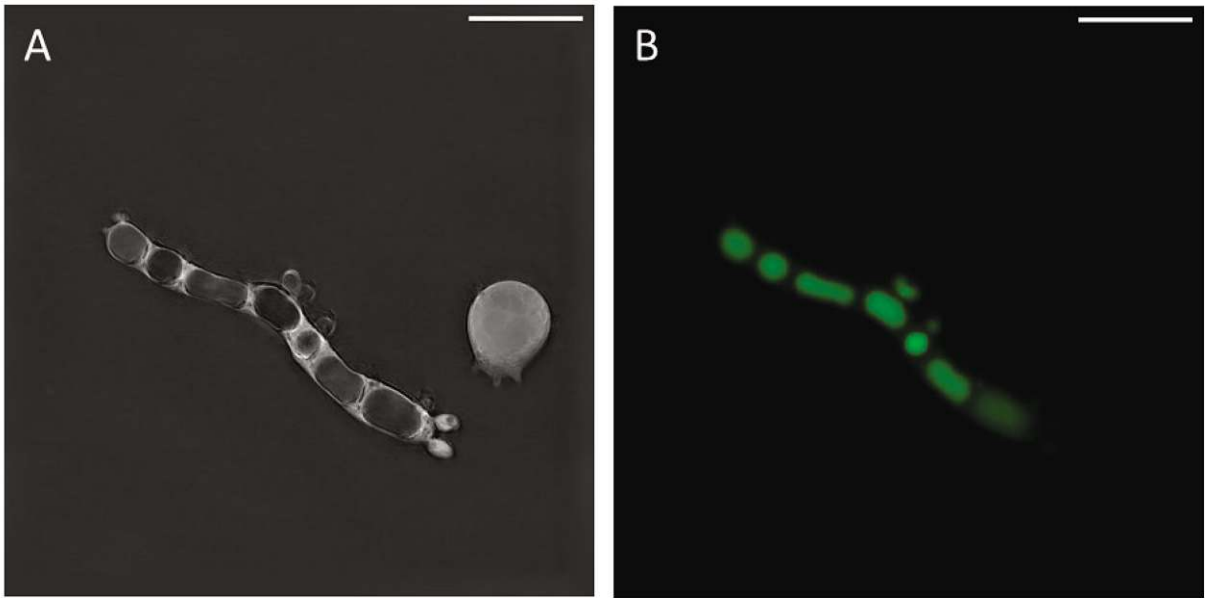

Figure 9: *Images of A. pullulans strain EXF-150 cultivated in MEX and stained with CDCFDA.*
(A) Holotomographic slice. **(B)** Fluorescence signal of the dye, colorized. Scalebar: 20 µm.

3.3.3. Mitochondria

The next investigated subcellular structures were the mitochondria. So far, the mitochondrial networks could be identified in the RI map of mammalian cells appearing as brighter lines compared to the cytosol (Sandoz et al., 2019). Staining of fungal cells was performed with MitoTracker™ Deep Red FM which accumulates in active mitochondria (Xiao et al., 2016).

In **Figure 10**, images of the *A. niger* wild type ATCC 1015 cultivated in MM is shown. No RI pattern of the holotomographic slice in **Fig. 10A** overlaps with the signal of the dye in **Fig. 10B**. However, more and less intensively stained areas are visible in **Fig. 10B** presumably indicating accumulated mitochondria.

Figure 11 shows an image of the citric acid production strain ACIB1 cultivated in VM. Again, there is no overlap of the RI map in **Fig. 11A** with the signal of the dye in **Fig. 11B**.

In **Figure 12**, images of *A. pullulans* wild type EXF-150 cultivated in MEX are shown, while **Figure 13** and **Figure 14** depicts images of *T. reesei* strain QM6a Δtmus53 cultivated in MA. There is no overlap between the stained areas in the fluorescence image (**B**) and an RI pattern in the holotomograms (**A**) for both fungi. Furthermore, the zoomed image in **Figure 14** demonstrates that the resolving power of the microscope is insufficient for visualizing details of the small hyphae of *T. reesei*.

To ensure that no details were overlooked, all the individual holotomographic slices were analyzed. However, no mitochondrial patterns could be observed for the investigated organisms.

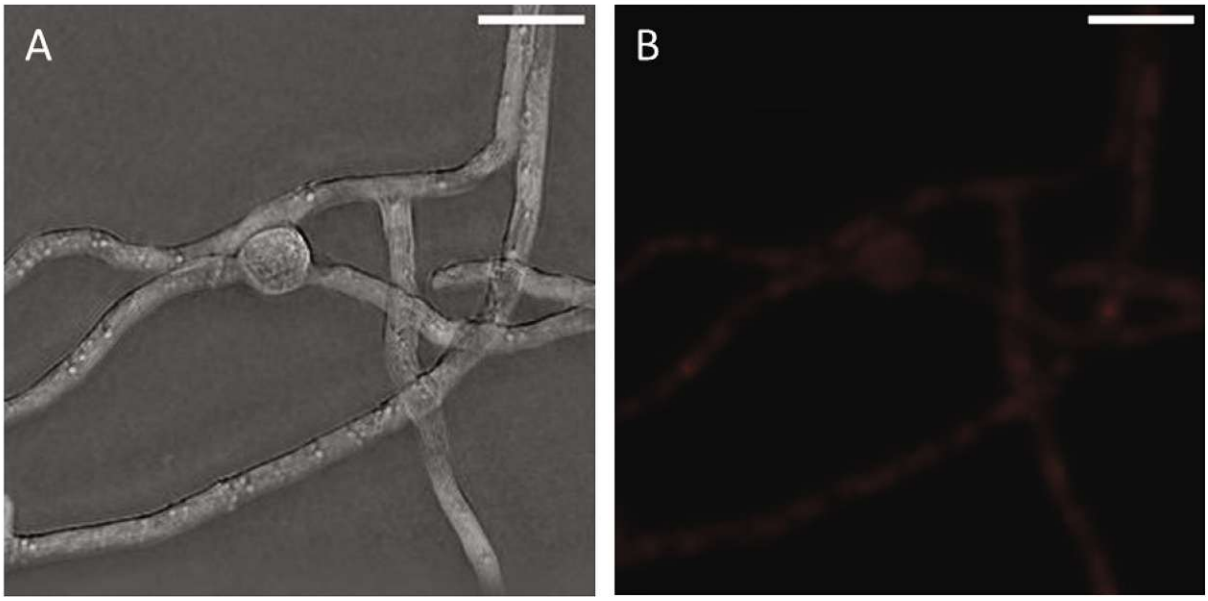

***Figure 10**: Images of A. niger strain ATCC 1015 cultivated in MM and stained with MitoTracker™ Deep Red FM.*
(A) Holotomographic slice. **(B)** Fluorescence signal of the dye, colorized. Scalebar: 10 µm.

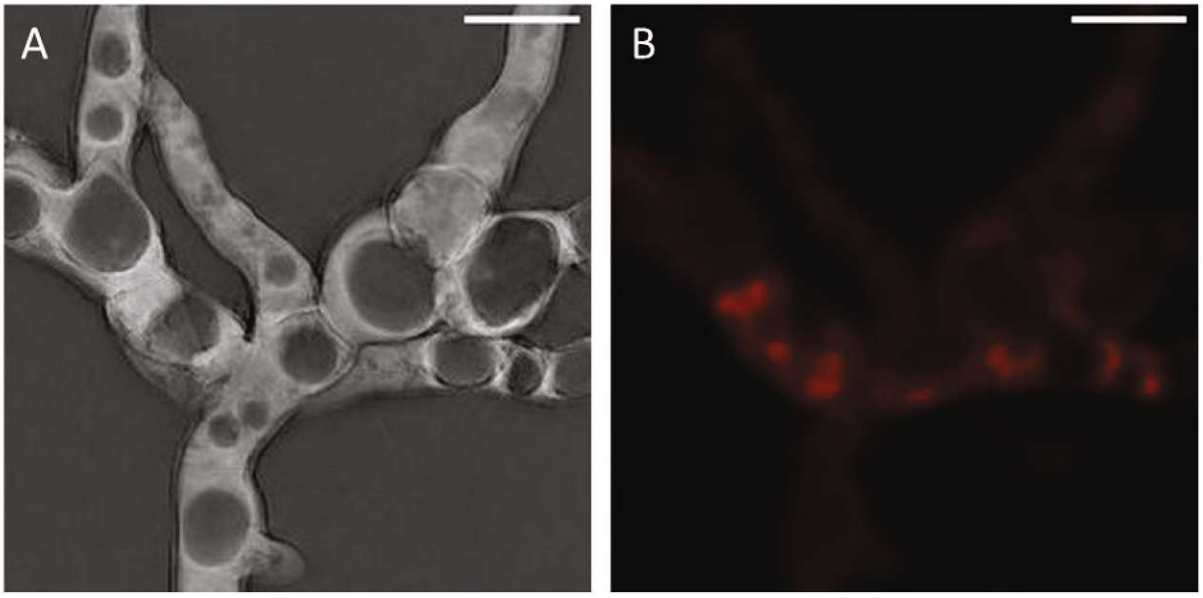

***Figure 11**: Images of A. niger strain ACIB1 cultivated in VM and stained with MitoTracker™ Deep Red FM.*
(A) Holotomographic slice. **(B)** Fluorescence signal of the dye, colorized. Scalebar: 10 µm.

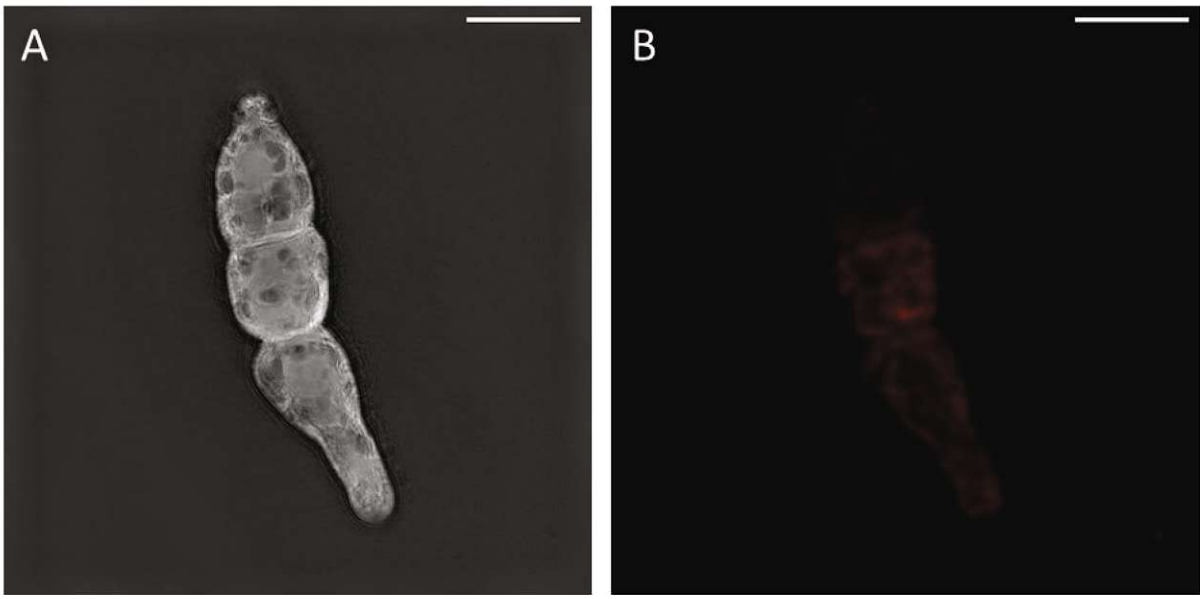

***Figure 12**: Images of A. pullulans strain EXF-150 cultivated in MEX and stained with MitoTracker™ Deep Red FM.*
(A) Holotomographic slice. **(B)** Fluorescence signal of the dye, colorized. Scalebar: 20 µm.

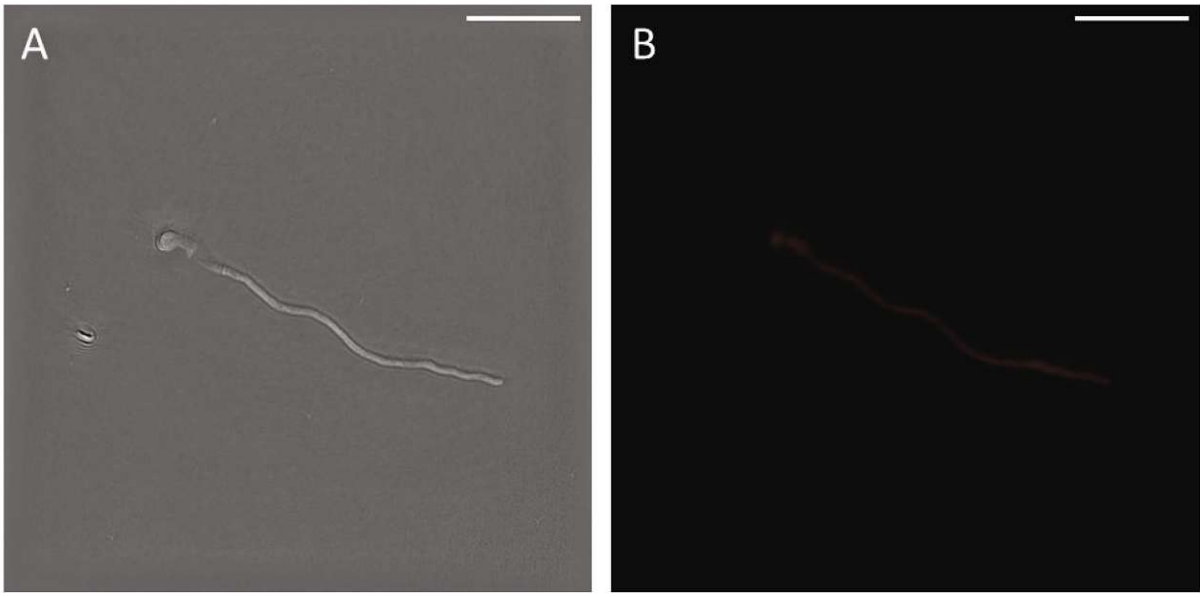

***Figure 13**: Images of T. reesei strain QM6a Δtmus53 cultivated in MA and stained with MitoTracker™ Deep Red FM.*
(A) Holotomographic slice. **(B)** Fluorescence signal of the dye, colorized. Scalebar: 20 µm.

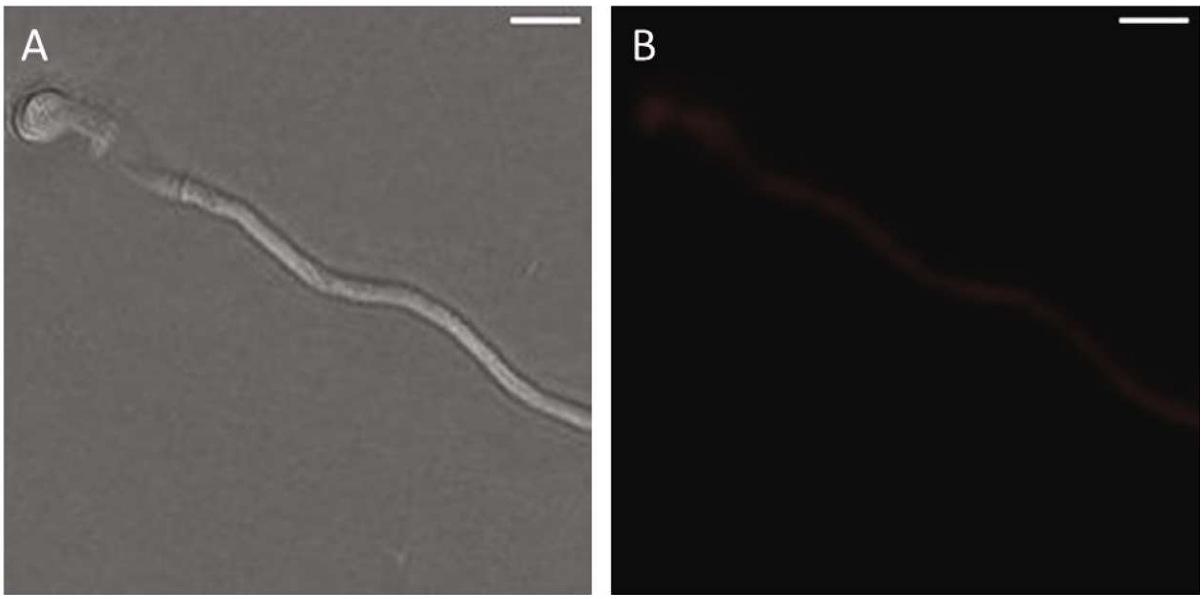

***Figure 14**: Zoomed section of the images shown in **Figure 13**.*
(A) Holotomographic slice. **(B)** Fluorescence signal of the dye, colorized. Scalebar: 5 µm.

3.3.4. Microtubules

In the course of this work, a strain was engineered to express the structural protein α-tubulin with a GFP-tag at the *pyrG* locus under the tet-on inducible promoter system. As the RI of microtubules is high compared to the cytosol (Krivosudský et al., 2017) it is expected that tubular networks are visible in the RI map captured by HTM. **Figure 15** shows images of the *A. niger* strain A621_tubA:sGFP that was cultivated in MM and induced with 1 µg/mL doxycycline. As shown in **Fig. 15B**, the signal of the GFP seems to be equally distributed among the hyphae. Only spots, that were earlier identified as vacuoles, show no fluorescence signal. No specific RI pattern in **Fig. 15A**, that shows a holotomographic slice, can be assigned to the fluorescence signal of the GFP.

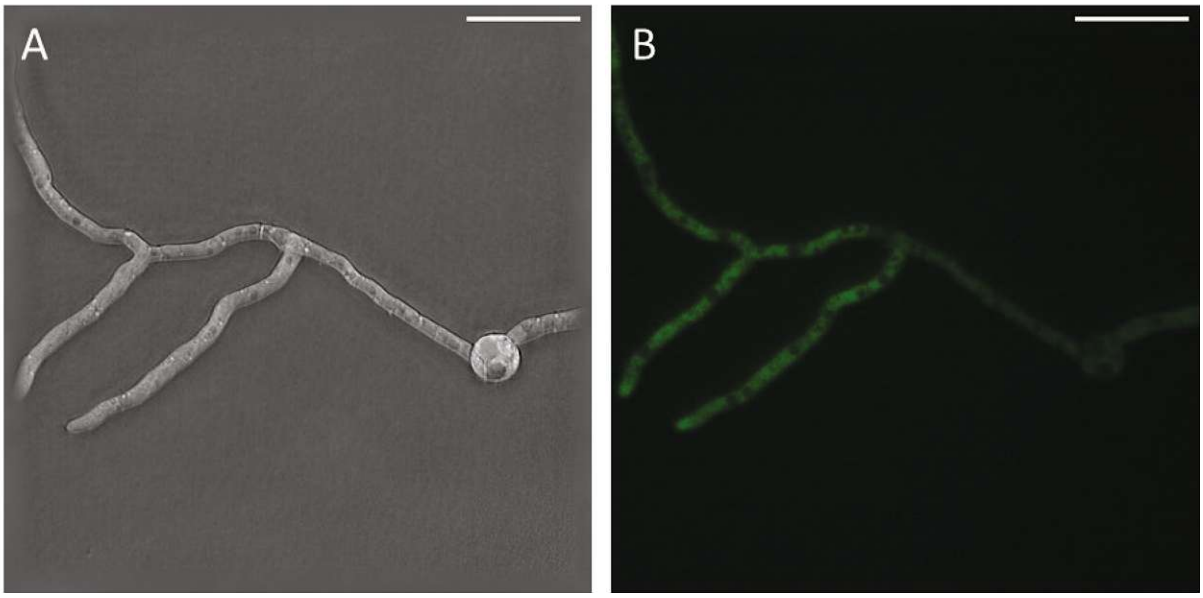

***Figure 15**: Images of the engineered A. niger strain A621_tubA:sGFP cultivated in MM and induced with 1 µg/mL doxycycline.* **(A)** Holotomographic slice. **(B)** Fluorescence signal of the GFP, colorized. Scalebar: 20 µm.

3.3.5. Nuclei

The positions of nuclei were visualized by tagging the histone H2A with sGFP. In **Figure 16**, images of the engineered *A. niger* strain A621_H2A:sGFP expressing H2A with a GFP-tag at the *pyrG* locus under the tet-on inducible promoter system are depicted. The fungus was cultivated in MM supplemented with 1 µg/mL doxycycline. In **Fig. 16A**, a holotomographic slice is shown and in **Fig. 16B** the GFP signal is overlaid. The green dots indicating the positions of the nuclei in the hyphae do not match with a specific RI pattern. To confirm this result, all holotomographic slices containing information were analyzed. However, there was no RI pattern indicating the position of the GFP-tagged nuclei.

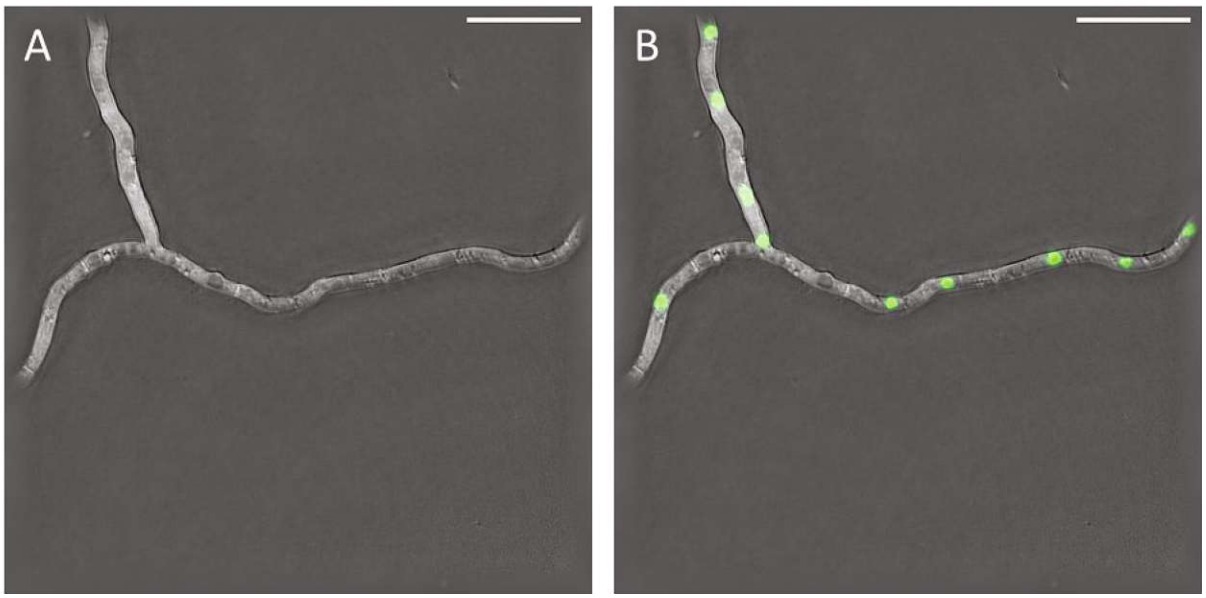

***Figure 16**: Images of the engineered A. niger strain A621_H2A:sGFP cultivated in MM induced with 1 µg/mL doxycycline.* **(A)** Holotomographic slice. **(B)** Holotomographic slice with the GFP signal overlaid, colorized. Scalebar: 20 µm.

As it was considered possible that the cell wall blocks the visualization of cell organelles by HTM, a cell wall digest was performed using the engineered *A. niger* strain A621_H2A:sGFP. The cell wall of hyphae and that of conidia was digested and the cells were subsequently imaged. For this experiment, nuclei were selected as they represent larger subcellular structures compared to mitochondria or microtubules, making them easier to locate in the RI map. Previous studies confirmed that nuclei of mammalian cells have a lower RI compared to the cytosol (Schürmann et al., 2016; Steelman et al., 2017). Therefore, assuming the same for fungi, nuclei should appear as darker spots in the RI map.

In **Figure 17**, hyphae of the engineered strain after cell wall digest are shown. **Fig. 17A** shows the maximum intensity projection of the holotomographic slices and in **Fig. 17B** the signal of the GFP is overlaid. Maximum intensity projection was used as the hypha was not growing

planar and therefore more holotomographic slices are required to obtain a meaningful image. **Figure 18** shows images of a protoplast of the same strain. In **Fig. 18A** a holotomographic slice is depicted and in **Fig. 18B** the GFP signal is overlaid. Darker spots in the RI map correspond to the positions of the nuclei, as indicated by the GFP signal. The finding confirms that the fungal cell wall has a significant impact on HTM. Furthermore, in **Figure 18** there is an expected difference in color visible for the large vacuole in the middle of the cell, which appears as very dark structure while the nuclei show a less dark to greyish color.

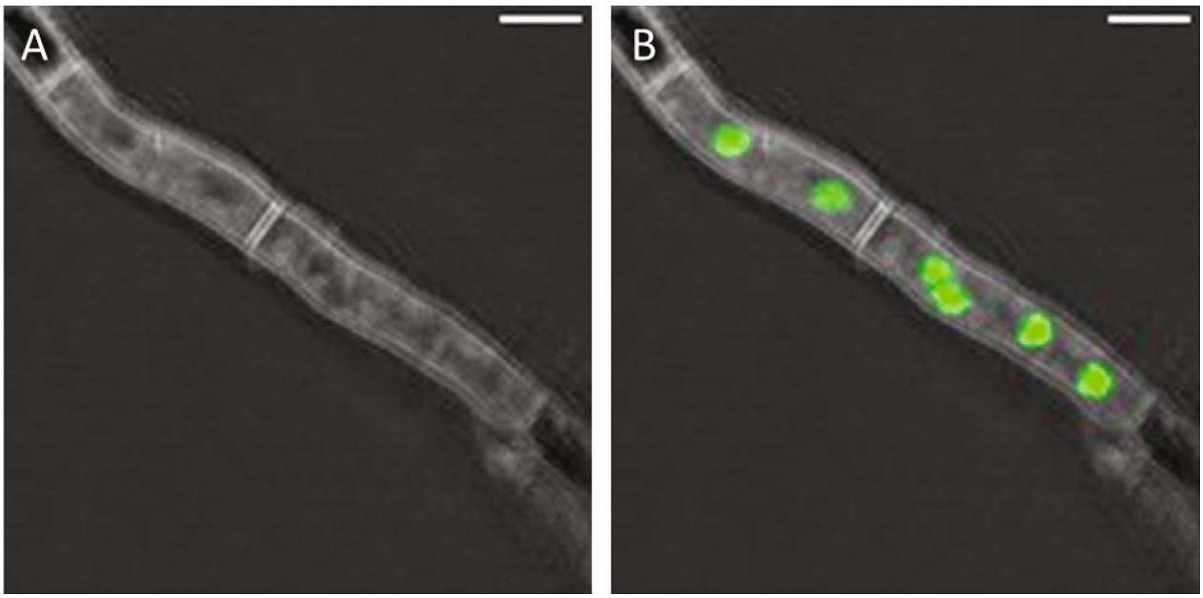

***Figure 17**: Images of the engineered A. niger strain A621_H2A:sGFP after cell wall digest with Vinotaste® Pro.*
(A) Maximum intensity projection of the holotomographic slices. **(B)** Maximum intensity projection of the holotomographic slices with the GFP signal overlaid, colorized. Scalebar: 5 µm.

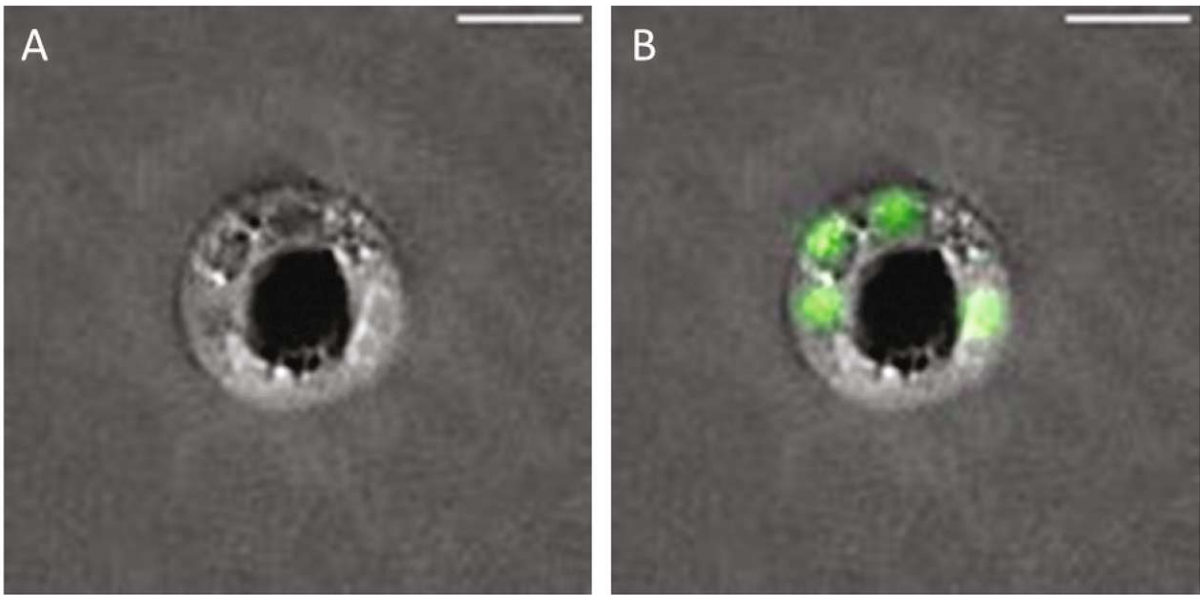

***Figure 18**: Images of a protoplast of the engineered A. niger strain A621_H2A:sGFP.*
(A) Holotomographic slice. **(B)** Holotomographic slice with the GFP signal overlaid, colorized. Scalebar: 5 µm.

3.4. Live-cell imaging

Several targets were selected for this study to investigate the potential of live-cell imaging using HTM. These included nuclei behavior and nuclei density, investigation of the CDK NimX^{Cdc2} and morphological analyses of different *A. niger* strains.

3.4.1. Nuclear dynamics of the engineered *A. niger* strain A621_H2A:sGFP

The nuclear dynamics in multinucleated organisms, such as the mycelium of filamentous fungi, are diverse. Mitosis, resulting in nuclear division, can occur synchronously, asynchronously, or parasynchronously. This pattern is mainly dependent on the organism but can sometimes change with changing environmental conditions such as low nutrient availability (Gladfelter, 2006). For instance, in *Neurospora crassa*, nuclei divide asynchronously without a visible pattern (Serna & Stadler, 1978). In *A. nidulans*, nuclei division occurs in a parasynchronous pattern starting from the hyphal tip, resulting in consecutive division of the neighboring nuclei (Clutterbuck, 1970). In contrast, synchronous nuclei division, where all nuclei within an apical compartment divide simultaneously, was reported in *Ceratocystis fagacearum* (Aist, 1969). Each of the described patterns has its own benefits and drawbacks for the metabolism of the fungal cell. However, specific studies on the nuclear dynamics of *A. niger* are lacking. Therefore, HTM was used to study nuclear dynamics in *A. niger*. Since the cell wall prevents the visualization of the nuclei by HTM, the modified strain expressing the histone H2A tagged with sGFP was used. Furthermore, it was necessary to combine HTM with fluorescence imaging in this experiment.

In **Figure 19**, a time-series of the engineered strain A621_H2A:sGFP cultivated in MM and induced with 1 µg/mL doxycycline is shown. Maximum intensity projection of the holotomographic slices was required as the hyphae grow generally less planar when using the ibidi® µ-Dishes. The link to the corresponding video is included as online material and can be found in the **Appendix**. In the first image at 13:10:00 hours, a hypha without septa is visible. After 20 minutes, septa appear as distinct lines. As a result, a nucleus is localized in a subapical compartment marked with the red arrow. The third image, at 14:30:00 hours, shows the time point before nuclear division in the left compartment of the hypha, marked with a red rectangle. Eight minutes later, at 14:38:00 hours, the nuclei have simultaneously divided. The subsequent two images at 14:42:00 hours and 14:46:00 hours show the same behavior for the hyphal compartment on the right, which is again marked with a red rectangle. For the

remaining time of the time-lapse recording, until 20:38:00 hours, the separated nucleus in the subapical compartment rests at the same position undergoing no nuclear division.

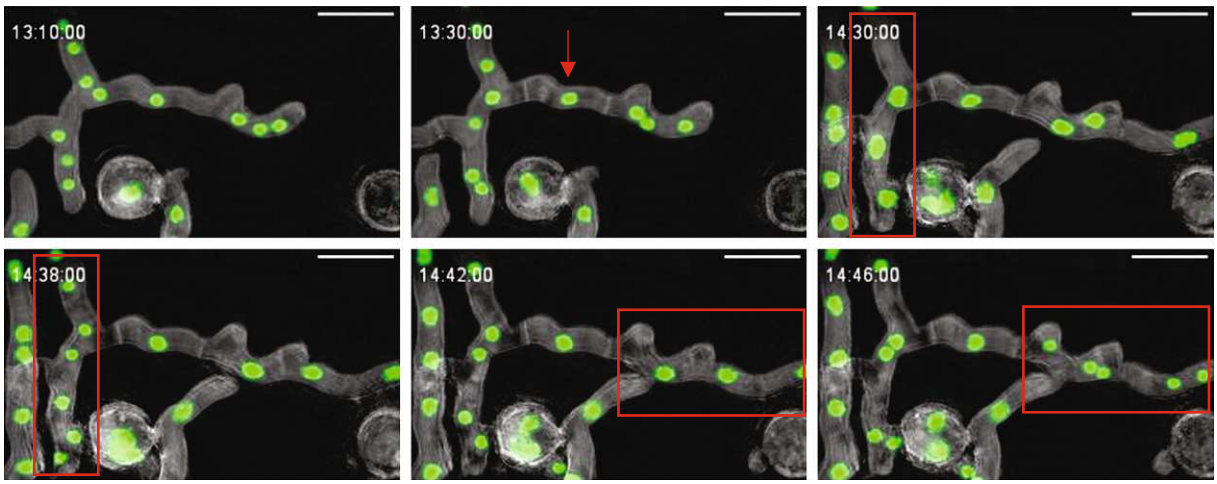

***Figure 19**: Time-series of the engineered A. niger strain A621_H2A:sGFP cultivated in MM and induced with 1 µg/mL doxycycline.*
Maximum intensity projection of the holotomographic slices with the GFP signal overlaid. Events described in the continuous text are highlighted in red. Scalebar: 10 µm.

3.4.2. Determination of nuclei density of the engineered *A. niger* strains A621_H2A:sGFP and K621_H2A:sGFP

In this experiment the nuclei density of both the *A. niger* wild type ATCC 1015 and the citric acid production strain ACIB1 was determined and compared. However, since fluorescence imaging was required to count nuclei, the engineered strains A621_H2A:sGFP and K621_H2A:sGFP which express GFP-tagged histone H2A were used. The aim here was to see if there is a difference in nuclei density between the two strains used which could be related to their different morphology. In contrast to the wild type, the strain ACIB1 is characterized by thicker hyphae with a tendency to form more, but shorter branches, resulting in increased number of hyphal tips. This morphology seems to be in relation with its capability to secrete high amounts of citric acid (Paul et al., 1999). The nuclei density was calculated using the area of the analyzed hyphae. This method was previously used to determine the number of nuclei per unit volume of cytoplasm (#N/C) in *Ashbya gossypii* (Dundon et al., 2016). Furthermore, the nuclei density was calculated with a second approach, using the length of the hyphae. This approach was chosen because it may provide a more appropriate value for the elongated cellular shape of filamentous fungi.

The ATCC 1015 derived strain A621_H2A:sGFP was cultivated in MM, and the ACIB1 derived strain K621_H2A:sGFP in VM. Both were induced with 1 µg/mL doxycycline. Different media was chosen to compare the wild type strain under nutrient-limited conditions and the citric

acid production strain under production conditions. To receive comparable results, the nuclei were counted right before the synchronous nuclei division. Analysis of hyphae was limited to hyphae and their corresponding conidia that were completely in the field of view. Areas as well as the hyphae length were measured by hand with Fiji. The results are summarized in **Figure 20** and **Figure 21**. For the first approach, the ATCC 1015 derived strain had a slightly higher nuclei density with a mean of 0.0269 nuclei/µm² hypha compared to 0.0253 nuclei/µm² hypha for the ACIB1 derived strain. However, the difference was not statistically significant. In contrast, the second approach showed a significantly higher nuclei density for the ACIB1 derived strain with a mean of 0.1263 nuclei/µm hypha compared to 0.0813 nuclei/µm hypha for the ATCC 1015 derived strain.

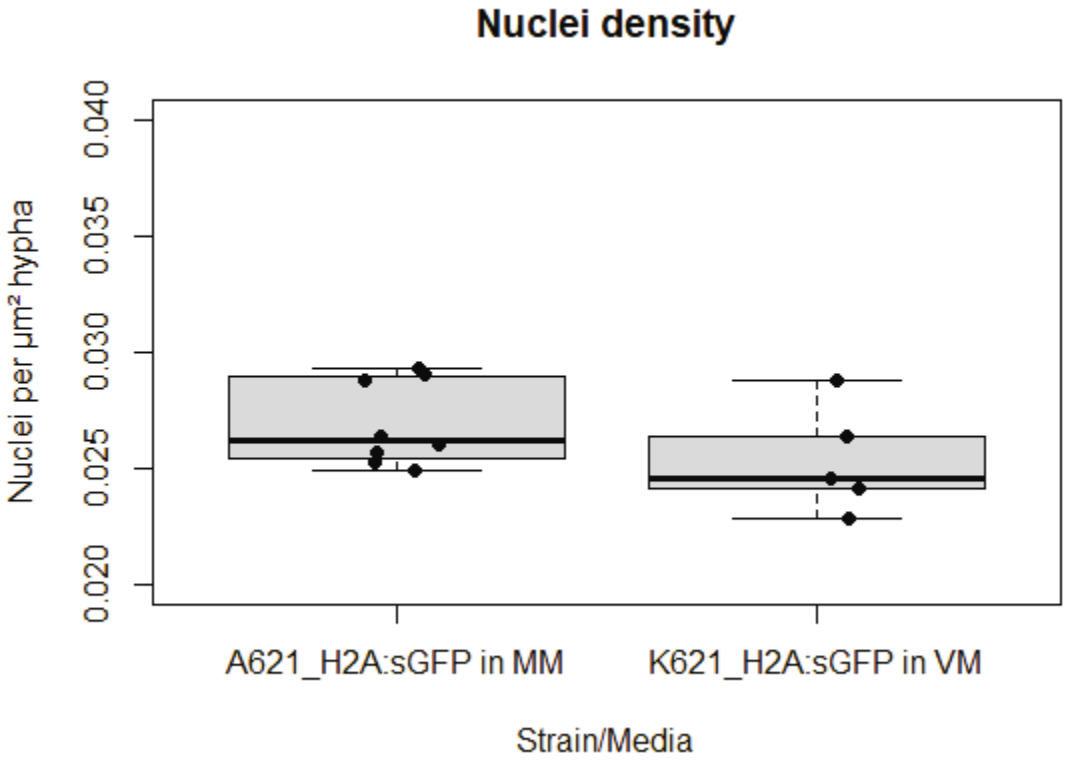

***Figure 20**: Determination of nuclei density per µm² hypha.*
The strains A621_H2A:sGFP cultivated in MM and K621_ H2A:sGFP cultivated in VM induced with 1 µg/mL doxycycline were analyzed. The black dots indicate the individual measurements. There is no significant difference in nuclei density between the strains.

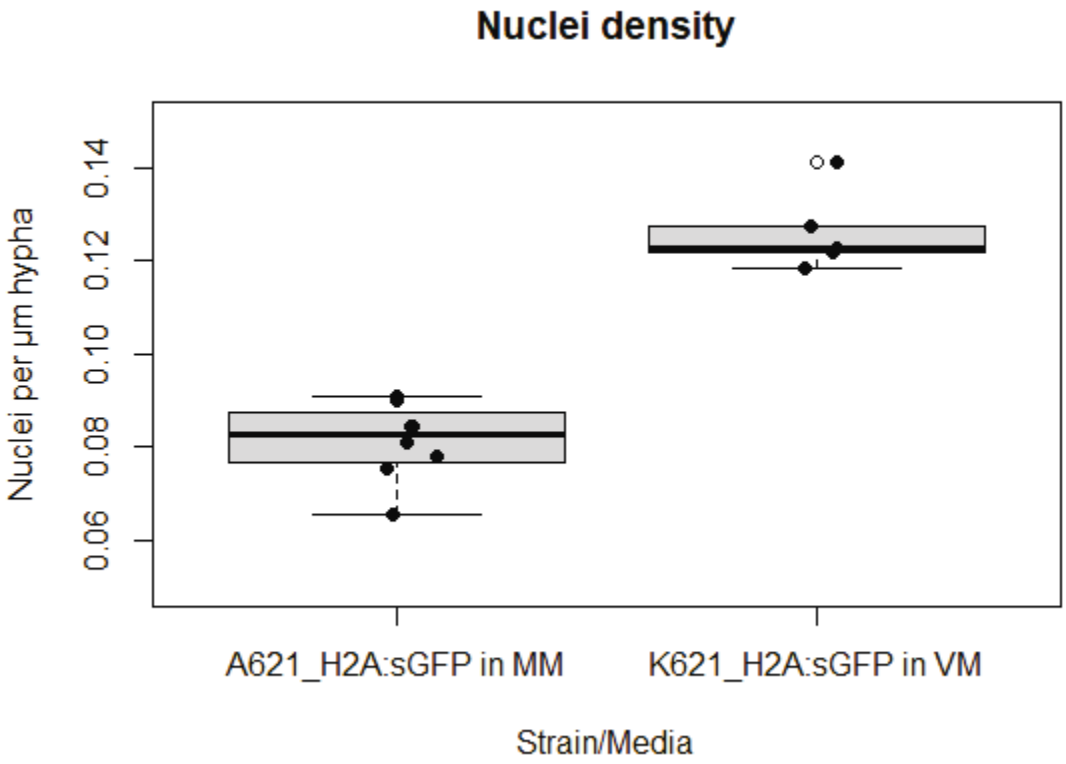

***Figure 21**: Determination of nuclei density per µm hypha.*
The strains A621_H2A:sGFP cultivated in MM and K621_ H2A:sGFP cultivated in VM induced with 1 µg/mL doxycycline were analyzed. The black dots indicate the individual measurements. The ACIB1 derived strain K621_H2A:sGFP shows a significantly larger number of nuclei per µm hypha.

3.4.3. Growth and morphological analysis of *A. niger* ATCC 1015 and ACIB1

A. niger wild type strain ATCC 1015 and the citric acid production strain ACIB1 were cultivated in minimal and Vogel's medium. The aim of this experiment was the analysis of morphological differences of these strains under nutrient-limited conditions as well as citric acid production conditions. Since citric acid production is associated with thicker, short-branched hyphae (Paul et al., 1999), this phenotype would be expected for the citric acid producer ACIB1. Furthermore, it was investigated whether the use of different media also causes a significant change in morphology. In contrast to MM, VM does not contain Mn^{2+}, which has been reported to significantly affect morphology, and, ultimately, citric acid production (Karaffa & Kubicek, 2003; Kisser et al., 1980). Parameters analyzed were conidia diameter, hyphal diameter, length of isotropic growth and the germination efficiency in the observed timeframe. The strains were cultivated for 16 hours and in this period time-lapse HTM was performed. The diameter of the conidia was measured at the time points 0, 3, 5, 7, 10 and 16 hours and the hyphal diameter was measured at 10 and 16 hours. To obtain comparable results, only conidia that reached the polarized growth state were analyzed.

In **Figure 22** the results for the measurement of the conidia diameter are shown. The citric acid production strain ACIB1 shows generally a significantly higher conidia diameter as well as a higher growth rate compared to the wild type strain *A. niger* ATCC 1015. After 16 hours of cultivation, conidia of ACIB1 had a mean conidia diameter of 12.87 ± 1.99 and 12.51 ± 1.89 µm in MM and VM, respectively. For ATCC 1015 the mean conidia diameter after 16 hours was 8.45 ± 0.86 µm in MM and 7.08 ± 0.82 µm in VM. It was observed that ATCC 1015 had significantly larger conidia in MM from 7 hours onwards when compared to VM. For ACIB1, no significant difference in conidia size was observed between cultivation in MM and VM. However, the diameter of ACIB1's conidia exhibited a significantly larger variance than that of ATCC 1015 at 10 and 16 hours.

A better visualization to compare these results is shown in **Figure 23**. The first plot shows the conidia diameter of ATCC 1015 and ACIB1 cultivated in both media at the 0-hour time point. The second plot shows the same for the 16-hour time point.

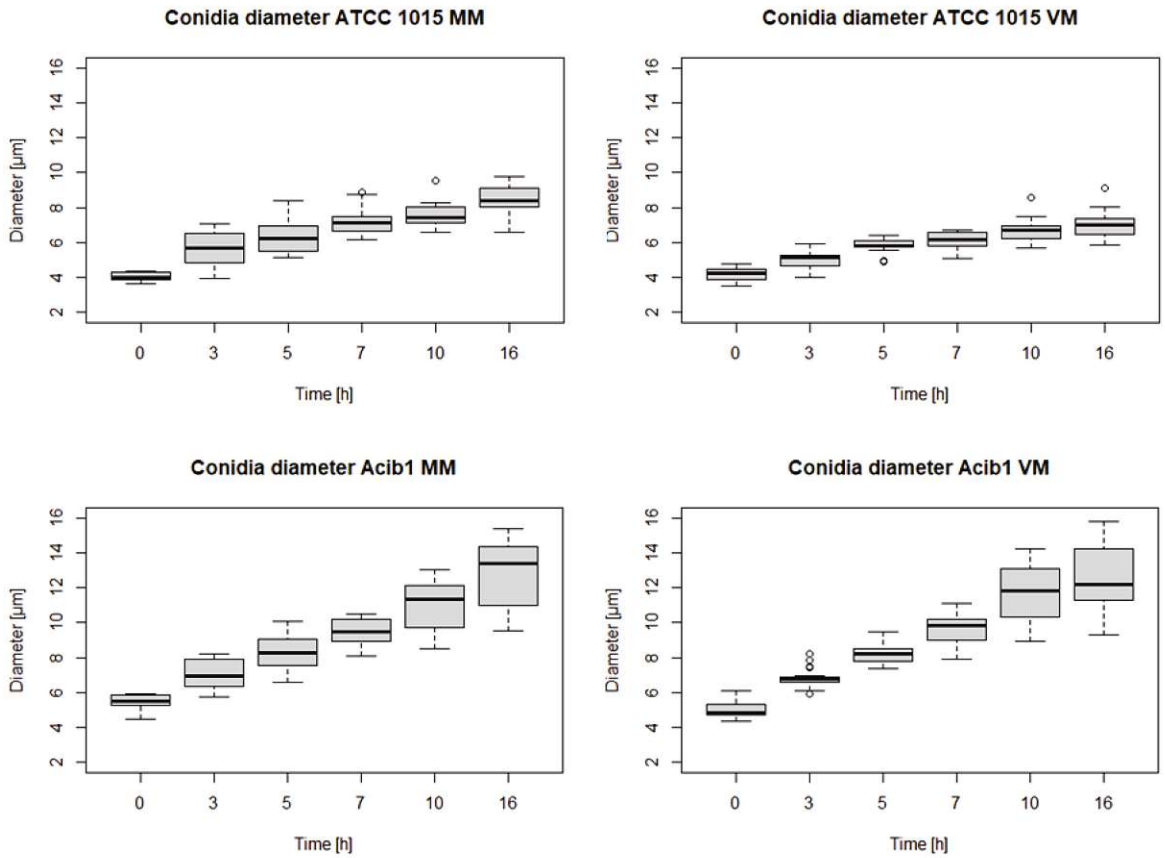

***Figure 22**: Measurements of the conidia diameter for different timepoints.*
The *A. niger* strains ATCC 1015 and ACIB1 were cultivated in MM and VM. Only conidia that reached isotropic growth are included in these graphs.

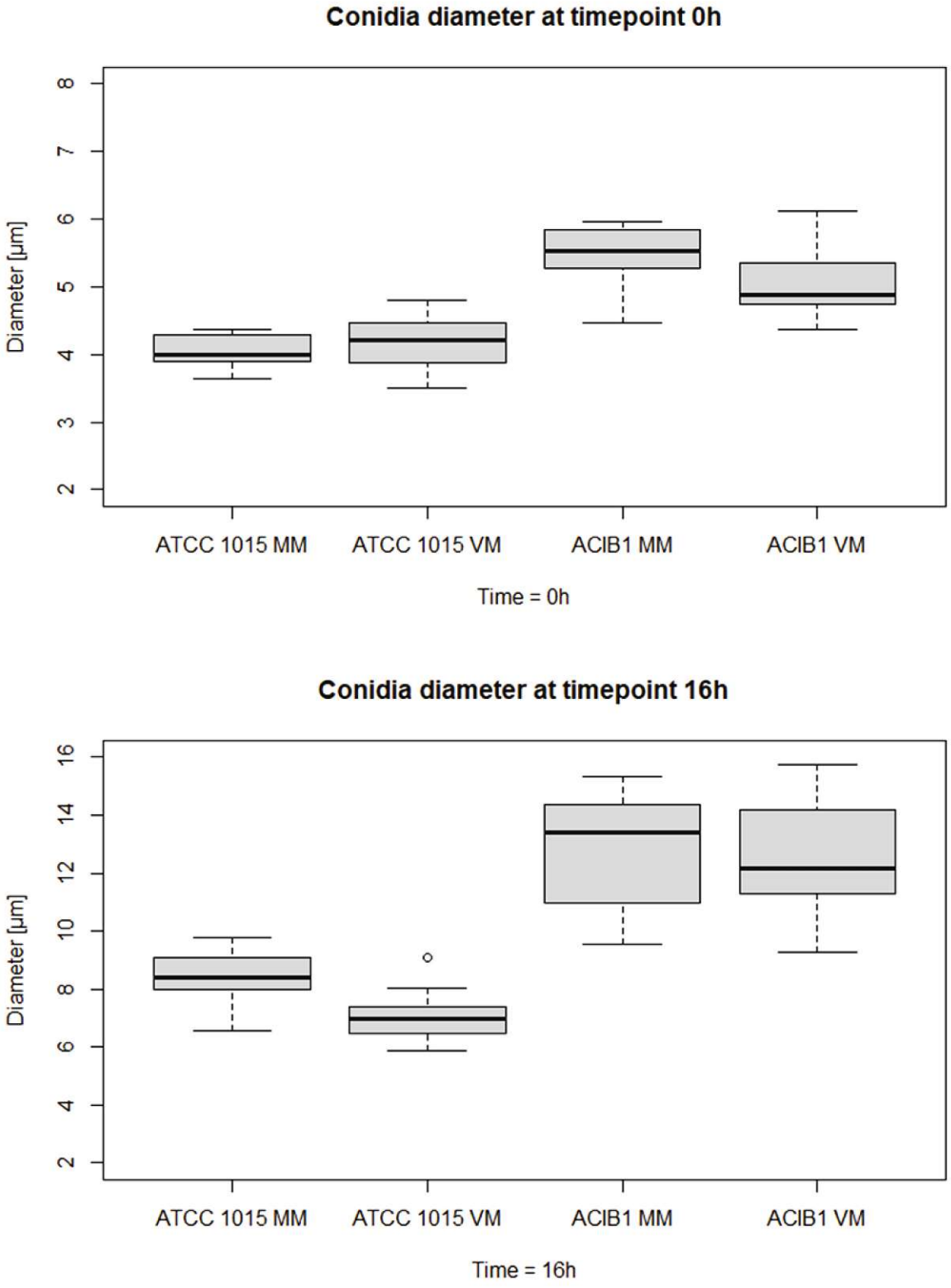

***Figure 23**: Measurements of the conidia diameter at time point 0h and 16h.*

A significant difference in conidia diameter is observed for ATCC 1015 compared to ACIB1 at the 0h time point. At the 16h time point, there is a significant difference in conidia diameter between ATCC 1015 cultivated in MM and VM.

To assess the growth kinetics, the conidial diameter measurement data were fitted to a growth model. The resulting growth model that gave the best fit is logarithmic and is shown in **Figure 24**. The model starts at the 3-hour time point to exclude the dormant phase of the conidia. In the upper left, the corresponding equations for each strain and media variant are shown, as well as the coefficient of determination. The logarithmic model fits well and shows a high R^2 around 0.99, except for ACIB1 grown in VM, which has a slightly lower R^2.

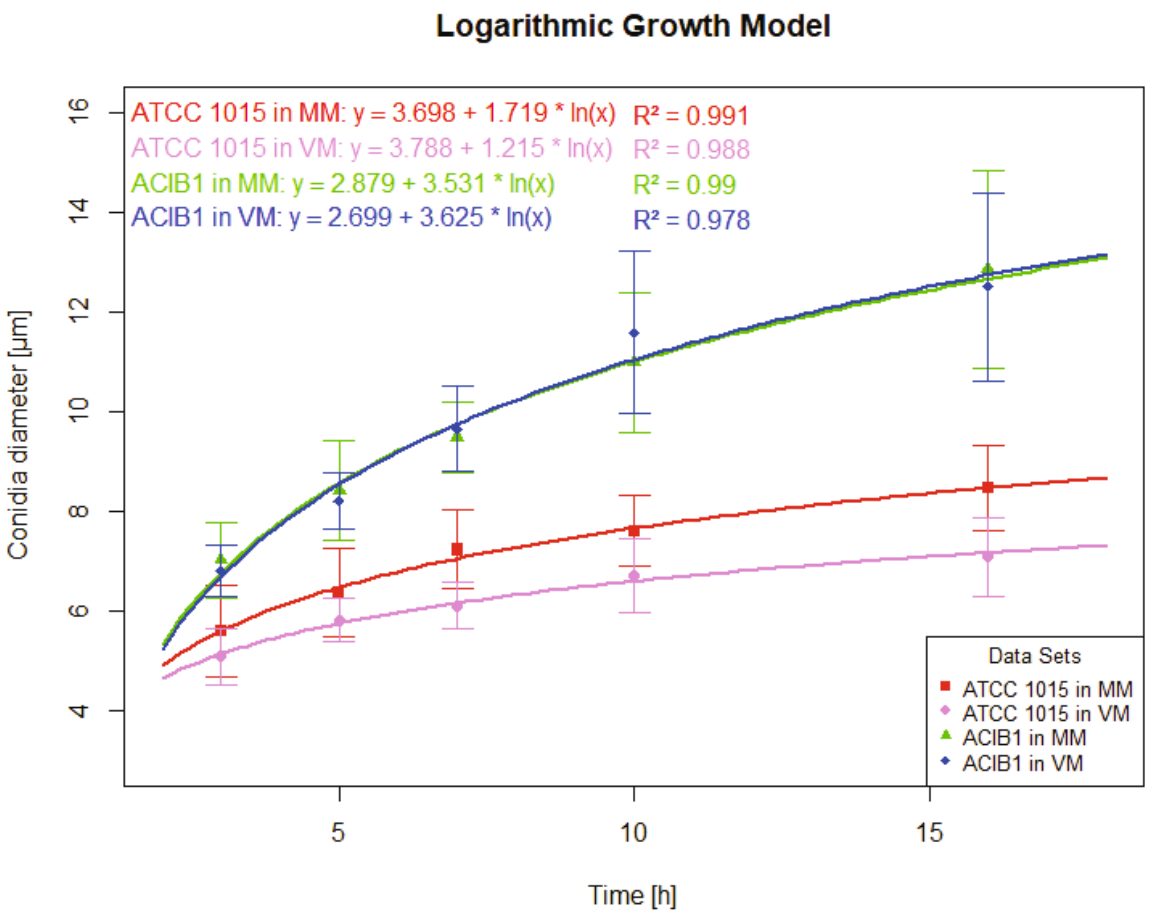

***Figure 24**: Logarithmic growth model of ATCC 1015 and ACIB1 cultivated in MM and VM.*
The logarithmic growth model visualizes the significant difference in conidia diameter of ATCC 1015 cultivated in MM and VM. For ACIB1, there is almost no difference in the growth curve between the two media used.

Furthermore, the corresponding conidia volume was calculated using the data of the conidial diameter, assuming that the conidia are spherical structures. The resulting model, presented in **Figure 25**, showed a linear relationship between conidia volume and cultivation time. In the upper left, the corresponding equations for each strain and media variant are shown, as well as the coefficient of determination. The coefficient of determination is slightly lower compared

to the logarithmic growth model, except for ACIB1 cultivated in MM. However, the linear model is suitable for the observed time frame in this experiment.

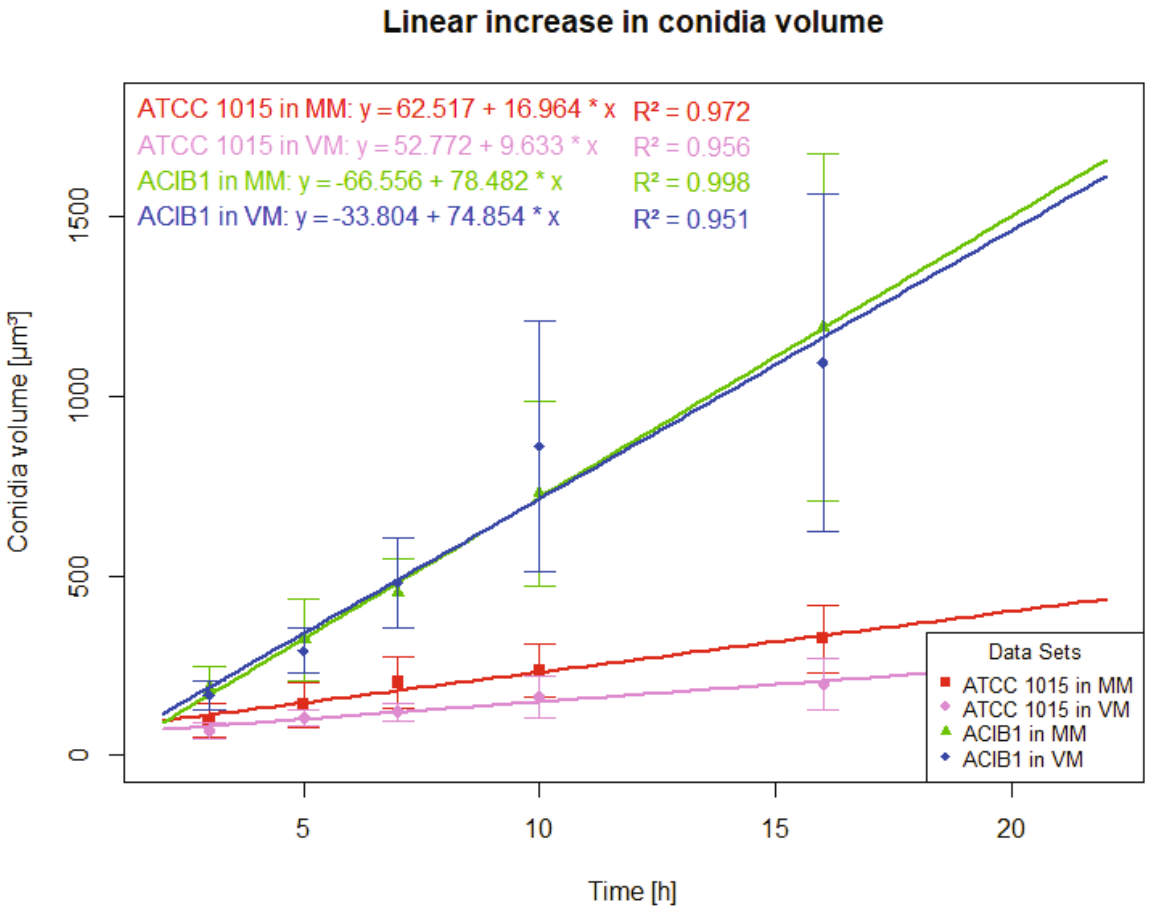

***Figure 25**: Linear regression of the conidia volume of ATCC 1015 and ACIB1 cultivated in MM and VM.*
Calculation of the conidia volume assuming spheric conidia showed a linear increase in conidia volume over time. The same trends are observed as presented in **Figure 22**. However, the standard deviation is high for the large conidia of ACIB1.

Figure 26 shows the results of the hyphal diameter measurements after 10 and 16 hours of cultivation. *A. niger* ACIB1 shows generally a significantly larger hyphal diameter compared to the wild type ATCC 1015. After 16 hours, the mean hyphal diameter of ACIB1 was 4.38 ± 0.5 and 4.51 ± 0.59 µm for MM and VM, respectively. ATCC 1015 had a mean hyphal diameter of 3.72 ± 0.27 µm in MM and 2.78 ± 0.19 µm in VM. As observed for conidia diameter, the difference in hyphal diameter between ATCC 1015 cultivated in MM and VM at the 16-hour timepoint is statistically significant. Additionally, ACIB1 exhibited a significantly larger hyphal diameter in VM compared to MM at the 10-hour timepoint. However, the conidia did not show a significant difference in diameter at this timepoint, despite being larger in VM.

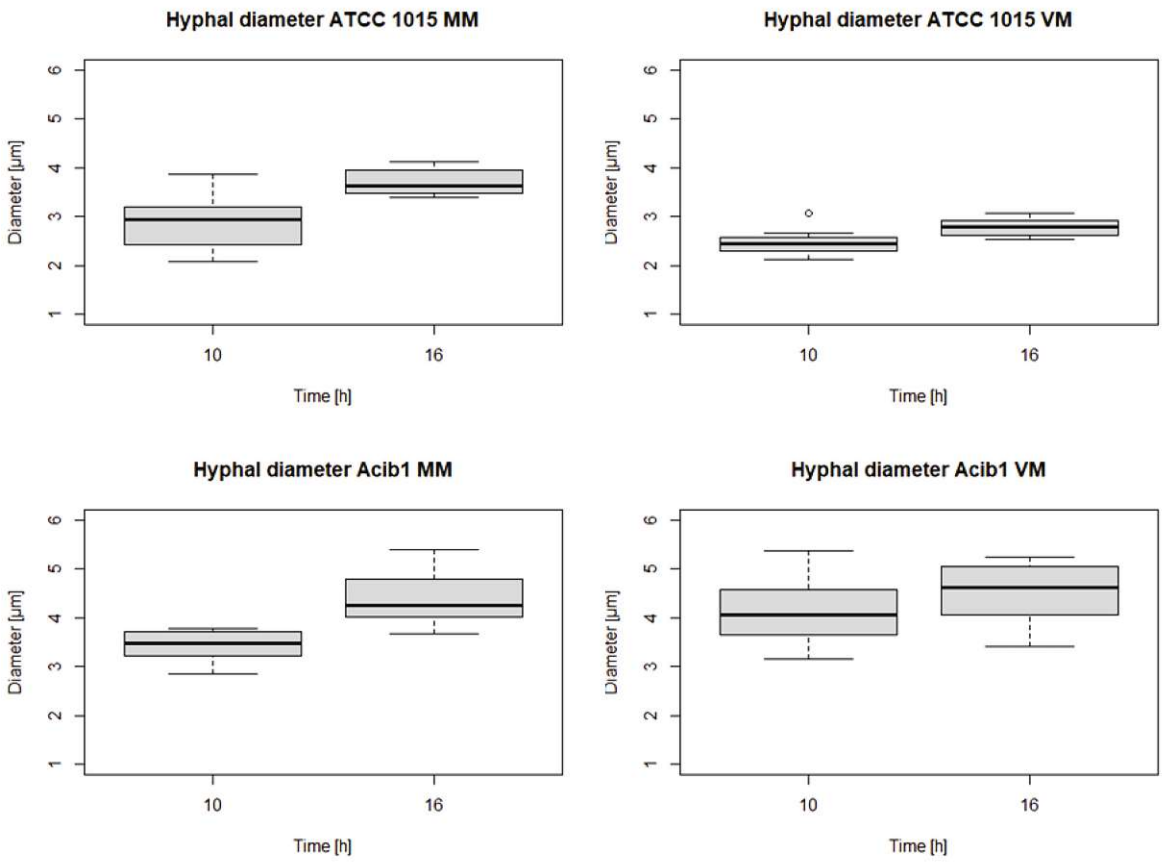

***Figure 26**: Measurements of hyphal diameter after 10 and 16 hours.*
The A. niger strains ATCC 1015 and ACIB1 were cultivated in MM and VM. The smallest hyphal diameter was observed for ATCC 1015 cultivated in VM. The same trend was observed for the conidia diameter. ACIB1 generally had a significantly larger hyphal diameter compared to ATCC 1015.

A better visualization of these results is shown in **Figure 27**. The first plot shows the hyphal diameter of ATCC 1015 and ACIB1 cultured in both media at the 10-hour time point and the second plot shows the same for the 16-hour time point. The significantly larger hyphal diameter of ACIB1 cultivated in VM compared to MM at the 10-hour time point can be observed. Furthermore, at the 16-hour time point, the hyphal diameter of ACIB1 is almost the same for both media, but the significant difference in hyphal diameter of ATCC 1015 cultivated in MM and VM is clearly visible.

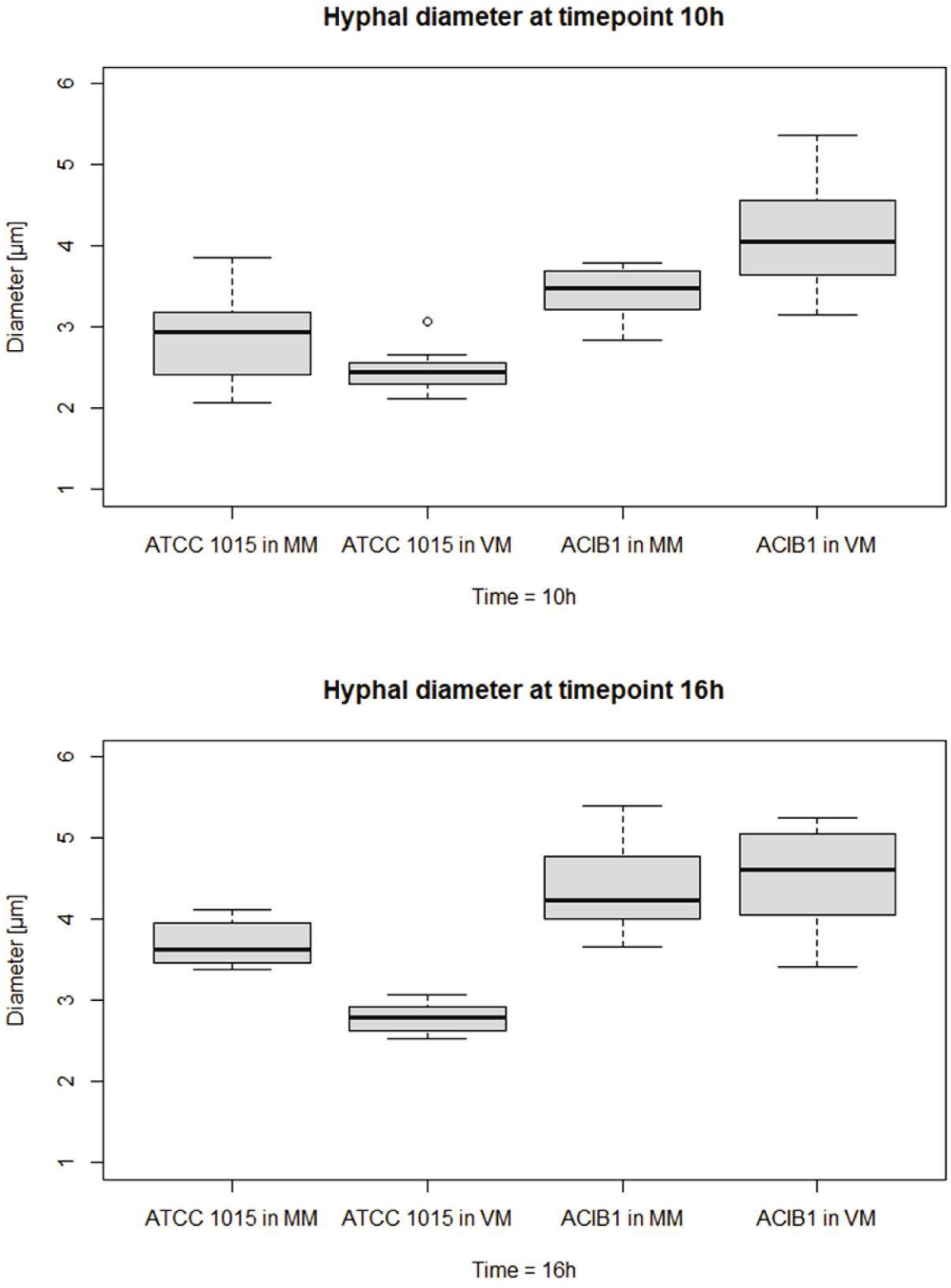

***Figure 27**: Measurements of hyphal diameter at time point 10h and 16h.*

A significant difference in hyphal diameter is observed for ATCC 1015 compared to ACIB1 at 10h and 16h. At the 16h time point, there is a significant difference in conidia diameter between ATCC 1015 cultivated in MM and VM. At the 10h time point, ACIB1 has a significantly larger hyphal diameter in VM compared to MM.

Additional data including germination efficiency during the time-lapse imaging, the average time of isotropic growth as well as the total number of analyzed conidia is shown in **Table 11**. The germination efficiency was the highest for ACIB1 cultivated in VM with 74.2% of conidia reaching the polarized growth state. ATCC 1015 cultivated in MM showed the lowest germination efficiency with 51.7%. In general, germination efficiency was higher in VM compared to MM and slightly higher for ACIB1 compared to ATCC 1015. The average time of isotropic growth, on the other hand, seems to be strain specific. The wild type strain ATCC 1015 had a shorter time of isotropic growth with a mean of 250.1 ± 103 minutes in MM and 229.2 ± 71 minutes in VM. ACIB1 stayed longer in the isotropic growth phase with 334 ± 99 and 314.4 ± 110 minutes in MM and VM, respectively. Although the variance was high for this parameter, the difference in isotropic growth length between the two strains was significant.

***Table 11**: Additional information for the growth and morphology analysis including the total number of analyzed conidia for a specific condition, the germination efficiency during the time-lapse imaging and the average time of isotropic growth.*

Strain/Media	Number of conidia observed	Germinating conidia [%]	Average time of isotropic growth [min]
ATCC 1015 MM	29	51.7	250.1 ± 103
ATCC 1015 VM	23	69.6	229.2 ± 71
ACIB1 MM	23	60.9	334 ± 99
ACIB1 VM	31	74.2	314.4 ± 110

3.4.4. Investigation of the CDK NimX^{Cdc2}

The CDK NimX^{Cdc2} of *A. niger* was targeted as it shows a high similarity to the CDK Cdc28 of *S. cerevisiae*. Cdc28 has been reported to play a major role in regulation of cell division (Mendenhall & Hodge, 1998). For budding yeasts, it was demonstrated that the mitotic CDK Cdc28 promotes the breakdown of the nuclear membrane as well as spindle formation and chromosome condensation prior to mitosis (Nigg, 2001). In the filamentous fungus *A. nidulans*, the homologous protein NimX^{Cdc2} was investigated. In this organism it is the only mitotic CDK, and its activity is therefore located in the nucleus. Besides their general function in initiating mitosis, it was reported that NimX^{Cdc2} plays an essential role in the cell cycle (Mcguire et al., 2000; Schier & Fischer, 2002). Therefore, the homologous protein in *A. niger* was investigated as it could affect growth, morphology and branching behavior.

The *A. niger* strain A621_NimX:sGFP developed in this work expresses a GFP-tagged NimX^{Cdc2} at the *pyrG* locus under the tet-on inducible promoter system. It was cultivated in MM and induced with 1 µg/mL doxycycline. The images in **Figure 28** show the engineered strain placed between microscope slides. **Fig. 28A** shows a holotomographic slice and **Fig. 28B** the corresponding GFP signal. As demonstrated previously for microtubules and nuclei, none of the RI patterns depicted in **Fig. 28A** coincide with the fluorescence signal in **Fig. 28B**. However, some dots showing a more intense fluorescence signal are visible in **Fig. 28B**, probably indicating the positions of the nuclei.

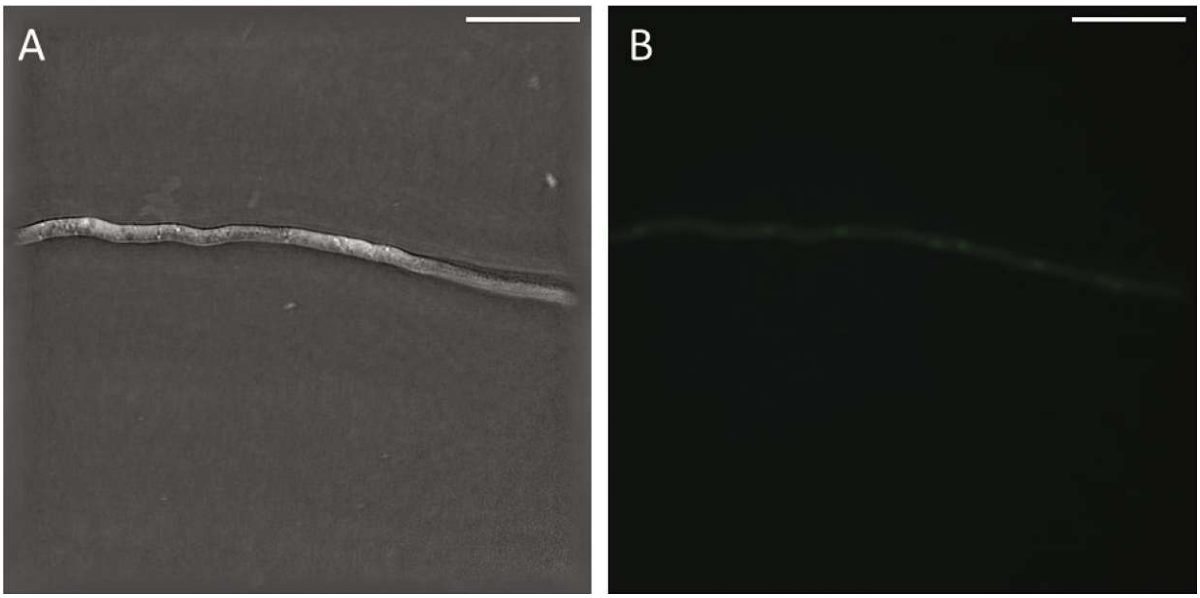

***Figure 28**: Images of the engineered A. niger strain A621_NimX:sGFP cultivated in MM induced with 1 µg/mL doxycycline.* **(A)** Holotomographic slice. **(B)** Fluorescence signal of the GFP, colorized. Scalebar: 20 µm.

To verify that the green dots observed in the fluorescence image represent the nuclei, the enigneered strain A621_NimX:sGFP was cultivated in MM induced with 1 µg/mL doxycycline and stained with NucBlue™ Live ReadyProbes™ Reagent. This dye was used to visualize nuclei as it emits blue fluorescence at 460 nm when bound to DNA. For visualization, the epifluorescence microscope Leica DMi8 was used. In **Figure 29** the GFP signal is shown in **A** and the signal of the dye is shown in **B**. This means that the GFP-tagged $NimX^{Cdc2}$ is visualized in **Fig. 29A** and the stained nuclei are depicted in **Fig. 29B**. The stained nuclei appear as demarcated structures and are located at distinct positions. However, the GFP signal does not directly overlap with the stained areas. Nevertheless, there are areas of more intense GFP signal that partially overlap with the stained nuclei.

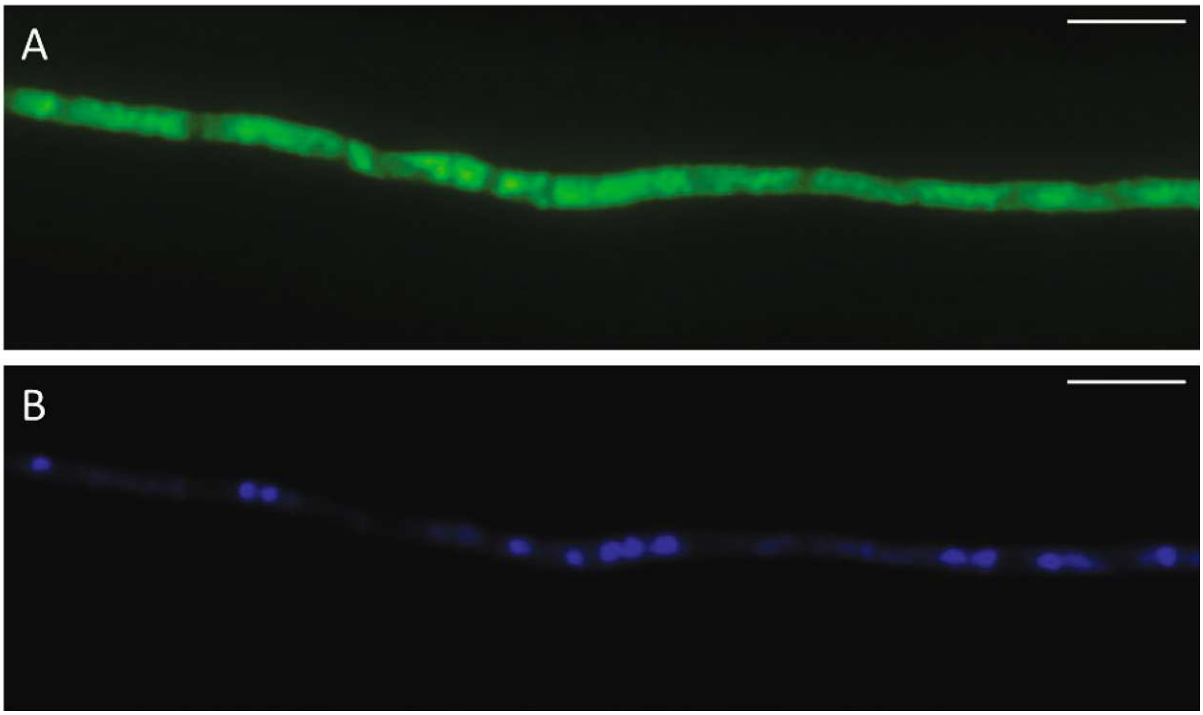

***Figure 29**: Images of the engineered A. niger strain A621_NimX:sGFP stained with NucBlue™ Live ReadyProbes™ Reagent.* **(A)** GFP signal of the protein. **(B)** Signal of the stained nuclei. Scalebar: 10 µm.

As an initial aim of this thesis was to investigate lateral branching mechanisms, live-cell imaging of the NimX overexpressing strain was of high interest. In **Figure 30** a time-series of the engineered strain is shown. The link to the corresponding video is included as online material and can be found in the **Appendix**. On the left, the maximum intensity projection of the holotomographic slices is depicted and next to it on the right the signal of the GFP. In the first image at 16:28:00 hours, the formation of two hyphae can be seen, marked with a red arrow. The following image at 18:16:00 hours shows growing hyphae in the maximum intensity projection and elongated green dots in the fluorescence signal. In the third image at 19:32:00 hours, the intensity of the green dots decreases. In the last image at 19:40:00, which is only eight minutes later, the green dots have disappeared suddenly. A similar observation was also made using the microscope slide approach. Although the GFP-tagged $NimX^{Cdc2}$ always produced a detectable GFP signal, the green dots that indicate a higher concentration of the protein, and most likely the positions of the nuclei, were not found in all parts of the mycelia. Assuming that the accumulated nimX represents the positions of the nuclei, no nuclear division was observed in the GFP signal in any time-lapse recording of the engineered strain. In contrast, the engineered strain expressing GFP-tagged H2A allowed for easy observation of nuclear division.

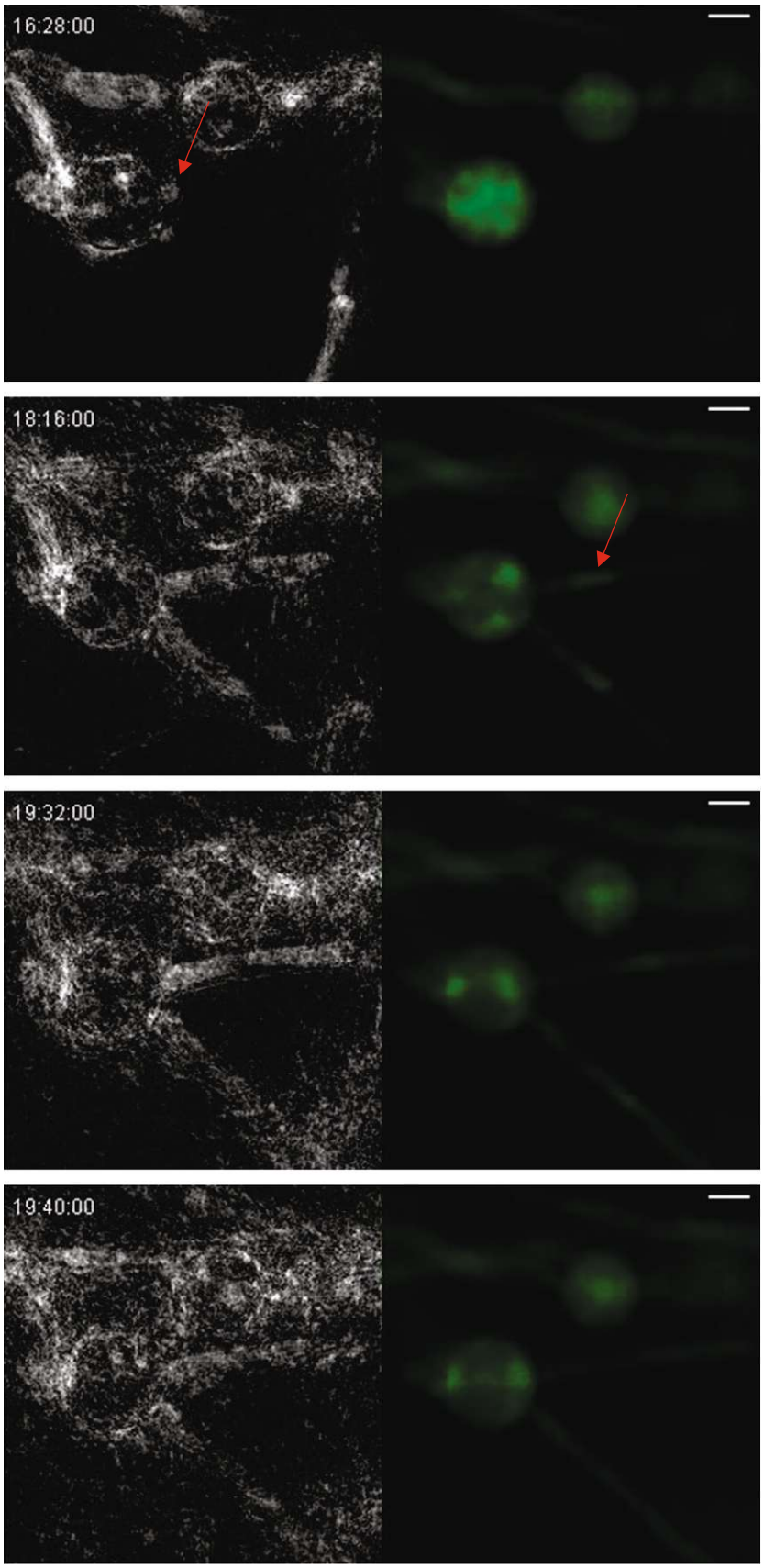

***Figure 30**: Time-series of the engineered A. niger strain A621_NimX:sGFP.*

On the left, the maximum intensity projection of the holotomographic slices is shown and, on the right, the GFP signal. (16:28:00) Hyphae emerge from a conidium, marked with a red arrow. (18:16:00) Growing hyphae show areas with a higher concentration of GFP-tagged NimX, marked with a red arrow. (19:32:00) The GFP signal gradually diminishes. (19:40:00) No areas remain in the hyphae that indicate a higher GFP concentration. Scalebar: 5 µm.

4. Discussion

The applicability of HTM on fungi was investigated in different experiments. Prominent subcellular structures including lipid droplets and vacuoles could be assigned to an RI pattern. However, other structures such as mitochondria, nuclei and proteins were not visible in the RI map. It could be confirmed that the fungal cell wall affects the visualization of subcellular structures by HTM. Furthermore, the protocol for live-cell HTM was optimized to increase image quality. Live-cell HTM was subsequently used to analyze growth and morphology, nuclear dynamics, and the CDK NimX^{Cdc2} of *A. niger*.

4.1. Optimization of the live-cell HTM protocol for fungi

As presented in the results in **Figure 3**, a difference in resolution and image quality was observed when using microscope slides versus the ibidi® µ-Dishes. Fine details including lipid droplets and demarcated brighter and darker areas were not visible when using an ibidi® µ-Dish. Furthermore, visible hyphae were blurred.

One of the reasons for this difference seems to be the increased media volume when using the ibidi® µ-Dishes. On the one hand, this allows mycelium to grow in the direction of the z-axis and therefore out of the focal point. As depicted in **Fig. 3B** and **Fig. 3C**, planes below and above the focal point show a lower resolution and appear blurry. When using microscope slides, there is only a thin layer of medium that restricts the movement of the mycelia in z-axis. Therefore, refocusing on the area of interest during live-cell imaging improves image quality and was considered critical for high image quality. Refocusing is necessary because a thermal focus drift always occurs when the media is heated to 30°C.

On the other hand, the thicker layer of medium may impact resolution as the laser must penetrate a greater distance, increasing the likelihood of unwanted interference with floating conidia, mycelium or particles. Therefore, it is crucial to sterile filter the media and allow the conidia to settle to the bottom of the ibidi® µ-Dish before live-cell imaging. However, it is not possible to eliminate all interfering particles.

The length of the time-lapse recording also affects image quality. A prime example on how the length of the time-lapse imaging influences the quality is shown in **Figure 30**. Despite post-processing the images by adjusting the contrast, resulting in reduced artifacts, the image of the RI map remains blurry, and artifacts persist. The main reason for this is, that the mycelium

grows out of the focal plane at a certain point and eventually interferes with the laser of the microscope. This effect can be reduced by decreasing the inoculation density. Imaging time may be extended beyond 20 hours if a low inoculation density is used.

Minor vibrations, the polymer bottom of the ibidi® µ-Dish as well as the water surface of the medium seem to have no significant impact on image quality. However, the placement of a coverslip on the surface of the medium seems to limit oxygen supply and therefore could affect growth and metabolism.

Summarized, it can be said the most important factor for high image quality during live-cell imaging is that refocusing is performed to have the area of interest exactly in the focal plane. However, live-cell imaging using ibidi® µ-Dishes does not allow for the same level of detail in the RI map as can be obtained with microscope slides.

4.2. Identification of subcellular structures and the role of the cell wall in HTM of fungi

Prominent subcellular structures such as lipid droplets and vacuoles were successfully assigned to an RI pattern. However, lipid droplets were hardly or not at all visible when using ibidi® µ-Dishes. This is probably due to the resolution difference discussed above. Additionally, lipid droplets were not visible in the RI map of *A. pullulans* cells. This may be attributed to their larger size compared to *A. niger*, combined with interference with the fungal cell wall. In contrast, vacuoles were visible in the RI map for both sample preparation methods and for *A. niger* and *A. pullulans*. The fact that very small vacuoles were not visible in the RI map could also be due to the fungal cell wall, as discussed in the following paragraph.

In general, the fungal cell wall was found to interfere with the laser and prevent the visualization of subcellular structures. Structures that could not be successfully assigned to an RI pattern were mitochondria, nuclei, and proteins. For nuclei, the cell wall digest revealed a characteristic RI pattern as shown in **Figure 17** and **Figure 18**. The fungal cell wall has a higher RI compared to the cytosol (Baró et al., 2021) and naturally acts as a mechanical and chemical barrier (El-Enshasy, 2007). Baró et al. showed that the fungal cell wall additionally acts as light modulator, and the reflectance of the fungal cell wall can reach up to 30% of the incoming light. However, this value depends on the wavelength of the incident light (Baró et al., 2021). Apart from the reflectance, the high RI of the cell wall, visible as a brighter grey, may obscure smaller differences in RI, such as small vacuoles, within the fungal cell.

Furthermore, it should be noted that the images presented in **Figure 17** and **Figure 18** may not accurately depict the state of a complete cell wall digest due to the continuous reproduction of new fungal cell walls. Therefore, it is possible that even finer structures could be observed if the cell wall is completely absent. Further experiments could be conducted by genetically engineering a strain deficient in cell wall production. However, it is important to note that this directly affects the survivability of the fungus. A fungal cell without cell wall does not represent a natural state and this could therefore influence growth and metabolism.

According to the results of this work, HTM can be used to visualize subcellular structures in fungi that show a large difference in RI to the surrounding cytoplasm such as lipid droplets and vacuoles. However, a detailed RI map including clearly distinct mitochondrial networks, nuclei and other subcellular structures as observed for mammalian cells (Sandoz et al., 2019) cannot be achieved with this technique for fungi without considering the fungal cell wall. One potential experiment is to add iodixanol to increase the RI of the imaging medium. D. Lee et al. successfully used this method for the yeast *Candida albicans* and could reduce artifacts, which resulted in the visibility of subcellular structures when applying HTM (D. Lee et al., 2022). Furthermore, when comparing mammalian cells with fungal cells, especially the different size must be considered besides the missing cell wall. For example, nuclei in mammalian cells can reach up to 20 µm in diameter (Lammerding, 2011), which is significantly larger than the reported average diameter of 2.2 µm for the fungus *Lentinula edodes* (Gao et al., 2019).

4.3. Live-cell imaging

The results so far have shown that there are several limitations for HTM of filamentous fungi. However, label-free 3D and easy-to-use live-cell imaging can be considered an advantage over other high-resolution live-cell imaging techniques, which are mainly based on fluorescent markers. For example, studies of fungal morphology and growth can be performed with little effort. In contrast, it is not possible to observe the movement of subcellular structures in fungi such as nuclei and proteins by HTM without additional labeling.

As shown in this work, HTM combined with fluorescence imaging can be used to observe cellular events such as nuclear movement and division, as well as the accumulation and localization of GFP-tagged proteins. However, fluorescence imaging requires significantly higher illumination levels, resulting in phototoxicity and/or photodamage. To minimize these

effects, the fungus was cultured for approximately 5 hours prior to fluorescence imaging. A fluorescence measurement was then performed every 2nd to 3rd frame, i.e. every 4 to 6 minutes. In addition, the required intensity and exposure time for each fluorophore and organism was determined and kept to a minimum. With this approach, there was no significant effect of the fluorescence laser on the growth of the fungus noticeable.

4.3.1. Nuclear dynamics of the engineered *A. niger* strain A621_H2A:sGFP

Image based analysis of nuclear dynamics showed that *A. niger* tends to a synchronous nuclei division in apical compartments. Furthermore, a nucleus located in a newly formed subapical compartment did not show significant movement or nuclear division during the observed timeframe of seven hours and was therefore considered mitotically inactive.

This pattern of a mitotically inactive nucleus in the first subapical compartment adjacent to an apical compartment was previously reported in *Fusarium oxysporum* (Ruiz-Roldán et al., 2010; Shahi et al., 2015). However, Shahi et al. demonstrated a switch in nuclear dynamics to a more complex pattern after two days of cultivation. Initially, young *F. oxysporum* mycelia exhibit a uninucleate state, which later transitions to a multinucleate state with parasynchronous nuclei division in the apical compartments. Furthermore, in some cases, mitotically active nuclei were observed in the first subapical compartment, and there was also a reactivation of previously inactive nuclei in older subapical compartments (Shahi et al., 2015). Ishikawa et al. reported diverse nuclear dynamics in Colletotrichum lindemuthianum (Ishikawa et al., 2013). They demonstrated that synchronous, parasynchronous, and asynchronous mitosis occurred in apical compartments, while subapical compartments mainly underwent synchronous nuclei division.

The presented studies suggest that nuclear dynamics in *A. niger* may be more complex and could change in later stages of growth. Further studies are required to strengthen the hypothesis of synchronous mitosis in apical compartments of *A. niger* due to the limited time frame of live-cell imaging in this experimental setup. To exclude other patterns of nuclear division, evaluation of more apical compartments is necessary, although this pattern has been observed multiple times during this work. Additionally, examining older mycelium, which is at least two days old, may be a promising approach to fully uncover the nuclear dynamics in *A. niger*.

4.3.2. Nuclei density of the engineered *A. niger* strains A621_H2A:sGFP and K621_H2A:sGFP

Determination of nuclei density showed a significantly higher nuclear number per µm of hypha in the ACIB1 derived strain K621_H2A:sGFP cultivated in VM. However, no significant difference was observed for the nuclear number per unit volume of cytoplasm (#N/C).

The cytoplasmic volume, however, does not increase proportionally to the hyphal area and is dependent on the hyphal diameter. As the analyzed strains exhibit different morphologies, the method proposed by Dundon et al. may not accurately reflect the nuclear number per unit volume of cytoplasm. However, the method proposed by Neumann and Nurse, which measures nuclear volume over cytoplasm volume (N/C) (Neumann & Nurse, 2007), could not be used due to the difficulty in accurately determining nuclear volume in this experimental setup. This is because fluorescence measurement is limited to the focal plane, and since the fungus grows in three dimensions, the GFP signal was not consistent. Furthermore, it should be noted that the number of individual measurements is low. Only a few of the time-lapse recordings could be analyzed because the growth of the hyphae out of the focal plane hindered the fluorescence measurement. Additionally, different media were used to compare the strains, increasing the number of factors that might affect the nuclei density.

Although few studies are available, previous work has shown that the number of nuclei per cytoplasm differs among various fungal species (Mela et al., 2020). In *Ashbya gossypii* the #N/C value remained constant even when the nuclei were clustered due to a knockout of a dynactin subunit (Dundon et al., 2016). Neumann and Nurse showed that the nuclear volume in *S. cerevisiae* is tightly correlated to the cytoplasm volume (Neumann & Nurse, 2007).

In summary, the results of this experiment suggest that there is no significant difference in #N/C between the strains, which is consistent with the findings of Dundon et al. The higher nuclear number per µm of hypha in the ACIB1 derived strain may be due to its larger hyphal diameter, resulting in a larger cell volume per µm of hypha. However, it should be noted that the N/C correlation of the spherical cells of S. cerevisiae may not apply to the elongated hyphae of filamentous fungi. Further studies are required to make a precise statement, including more individual measurements, and using the same cultivation medium for the analyzed strains or different media for only one strain. In addition, the utilization of microscope slides instead of culture dishes could enable accurate determination of nuclear volume and, consequently, the N/C ratio.

4.3.2. Growth and morphological analysis of *A. niger* ATCC 1015 and ACIB1

The experiment results indicate that the differences in micro-morphology and growth are mainly strain-specific, as the most significant variations were observed among the different strains used.

The citric acid production strain ACIB1 shows not only a faster growth rate, but also an overall higher conidia and hyphae size compared to the wild type ATCC 1015. Therefore, the longer time of isotropic growth until germ tube formation could be explained by their larger size and the necessity to acquire more material for cell wall production and metabolic activities. The slightly higher germination efficiency and lower germination time in VM could be attributed to the higher glucose concentration compared to MM. Ijadpanahsaravi et al. demonstrated that higher glucose concentrations enhance germination efficiency and reduce germination time (Ijadpanahsaravi et al., 2020).

At the 16-hour time point, a significant difference in hyphal diameter was observed for the wild type ATCC 1015 when comparing MM and VM. The same tendency was observed for conidia of ATCC 1015 after seven hours of cultivation. Furthermore, the presented growth curves visualize the difference between the two media used. A slower growth rate and smaller hyphal diameter of *A. niger* in glucose-rich medium was previously reported by Larralde-Corona et al. (Larralde-Corona et al., 1997). The exact mechanism behind this remains unclear, although changes in hyphal diameter appear to be related to the adaptation to high osmotic pressure.

At the 10-hour time point, ACIB1 showed a significant higher hyphal diameter in VM compared to MM, indicating a faster growth in the glucose-rich VM. The measured conidia size was also slightly larger in VM than in MM at 10h, although the difference was not statistically significant. This finding contrasts with the observations made by Larralde-Corona et al. However, it is possible that the industrial production strain is better adapted to high glucose concentrations, which are commonly used in industrial citric acid production. Furthermore, it is important to consider the difference in media composition. Apart from a higher glucose concentration in VM, there is also no Mn^{2+} included. Absence of Mn^{2+} has been reported to affect the micro-morphology of filamentous fungi towards small, swollen hyphae (Detroy & Ciegler, 1971). Therefore, the higher hyphal diameter of ACIB1 cultivated in VM at the 10-hour time point may be due to manganese deficiency.

The presented growth curves indicate a logarithmic increase in conidial diameter and a linear increase in conidia volume over time. However, there is a lack of studies on this particular topic to support these results. Nontheless, a previous study on *Aspergillus fumigatus* confirms that germinating conidia cease to grow in size after 24 hours (Du Pré et al., 2018). This observation favors the measured logarithmic increase in conidial diameter. However, it also implies that the linear increase in conidia volume only occurs until a certain size is reached.

4.3.3. Cell division control protein NimX^{Cdc2}

The cell division control protein NimX^{Cdc2} was detected in all hyphae of the modified *A. niger* strain. The GFP-tagged protein showed a uniformly distributed background fluorescence, with brighter spots observed in certain hyphae and conidia, but not throughout the entire mycelia. The nuclei staining with NucBlue™ Live ReadyProbes™ did not directly confirm that these spots were indeed the nuclei. The GFP signal showed areas of higher intensity that partially overlapped with the stained nuclei, but a direct overlap, as expected, was not observed. The reasons why the staining procedure could not confirm this expectation are discussed below.

As a different microscope device was used for this imaging procedure, the observed signal intensity might differ. Additionally, the staining efficiency of the NucBlue™ Live ReadyProbes™ dye was low, resulting in only a few hyphal compartments with well-stained nuclei. Consequently, the number of hyphae that could be investigated was limited. Since the accumulation of NimX^{Cdc2} was found only in certain hyphae, but not all, the absence of accumulated protein could be a random occurrence. However, none of the bright spots in the GFP signal, indicating accumulated NimX^{Cdc2}, were observed during the imaging procedure in any of the stained hyphae. This suggests that the staining procedure itself may have a negative impact on the visualization of the GFP-tagged NimX^{Cdc2}. Furthermore, photobleaching of the GFP may have affected the GFP intensity as it was necessary to search for well-stained areas under the higher energy illumination light of the Y5-T channel. A higher photobleaching rate was observed for wtGFP and αGFP when excited at a lower wavelength (Patterson et al., 1997).

However, based on previous studies in *A. nidulans*, it is highly probable that the bright spots observed in the GFP signal represent nuclear-accumulated NimX^{Cdc2} (Schier & Fischer, 2002). McGuire et al. have shown that NimX^{Cdc2} and its regulators play an essential role in progression of G_1 and G_2 of the cell cycle, septation, and conidiophore development in *A. nidulans* (Mcguire et al., 2000). Ye et al. could show that NimX^{Cdc2} is required for the G_2/M transition by

hyperphosphorylation of another protein kinase, NimA (Ye et al., 1995). The fact that no nuclear division could be observed in the GFP signal of the engineered strain expressing GFP-tagged nimX^{Cdc2} indicates that the protein is not located in the nucleus during cytokinesis which follows mitosis. In *S. cerevisiae*, exit of mitosis and onset of cytokinesis is induced by inactivation of mitotic CDKs, which is mainly controlled by the protein phosphatase Cdc14 (Sanchez-Diaz et al., 2012; Stegmeier & Amon, 2004). Furthermore, Wang et al. demonstrated that Cdc28 accumulates in the nucleus in late G_1 of the cell cycle (H. Wang et al., 2004). According to these studies and the results of this work, it can be inferred that the activity of NimX^{Cdc2} in the nucleus of *A. niger* is restricted from late G_1 until late mitosis. However, further studies are necessary to fully support this hypothesis.

Due to the diverse and important regulatory effects of NimX^{Cdc2} or its homologous proteins in the fungal cell cycle, it is reasonable to assume that there are additional roles of the protein yet to be discovered. For instance, Dynesen and Nielsen showed that a knockout of *nimX* in *A. nidulans* resulted in formation of significant less lateral branches compared to the wild type (Dynesen & Nielsen, 2003). However, no specific observations were made during this work that could be directly attributed to branching behavior or growth patterns influenced by overexpression of NimX^{Cdc2} in the engineered *A. niger* strains. Nevertheless, it could be promising to further investigate this protein as well as its regulatory pathway to gain more insights into its role in the fungal cell cycle or a possible influence on growth and branching patterns in *A. niger*.

5. Conclusion

Holotomographic microscopy was used to study the fungi *A. niger*, *A. pullulans*, and *T. reesei*. The applicability of this technique to fungal cells was evaluated by a variety of experiments including the assignment of subcellular structures to specific RI patterns, analysis of morphology and growth, as well as investigation of nuclear dynamics and the CDK NimX^{Cdc2} of *A. niger*.

For *T. reesei*, however, no subcellular structures could be assigned to an RI pattern due to their small size. Vacuoles were identified in *A. niger* and *A. pullulans* based on their RI. Lipid droplets were only visible in the RI map of *A. niger*. However, it was not possible to assign other structures, such as mitochondria, nuclei, and proteins, to a specific RI pattern, even though they are visible in the RI maps of mammalian cells. The fungal cell wall has been identified as a major drawback for this imaging modality as it interferes with the imaging of subcellular structures. Further data is necessary to make a precise statement on the severity of this interference. However, this work demonstrates that HTM on fungi is unable to produce a detailed RI map with clearly visible mitochondrial networks and nuclei, as observed in mammalian cells, without considering the fungal cell wall.

Furthermore, the protocol for live-cell HTM was optimized. However, the live-cell imaging approach using ibidi® µ-Dishes still resulted in a lower image resolution compared to microscope slides. Additional live-cell experiments with *A. niger* were conducted. HTM was combined with fluorescence imaging to analyze nuclear dynamics and the nuclei density of two different strains. Thereby, synchronous nuclei division was observed in apical hyphal compartments of *A. niger*. The nuclei density, however, seems to be correlated to the cell volume, although a difference between the wild type ATCC 1015 and the citric acid producer ACIB1 was observed when only hyphae length was considered. In addition, the CDK NimX^{Cdc2} was tagged with sGFP and investigated as this protein was suspected to be involved in the regulation of branching mechanisms. However, no direct relation to the branching behavior of *A. niger* was discovered, but the protein was found to accumulate in the nuclei at certain time points. Since no nuclear division was observed in the fluorescence signal of the GFP-tagged NimX^{Cdc2}, the hypothesis was made that the protein is not located in the nucleus during cytokinesis. However, to make a precise statement about this observation, additional research is required. An analysis on morphology and growth of the *A. niger* wild type ATCC 1015 and

the industrial citric acid production strain ACIB1 in two different media showed primarily strain-specific differences. However, the glucose-rich Vogel's medium slightly inhibited the growth of the wild type strain but did not have such an effect on the other strain. Additionally, this work shows that the growth in conidial diameter can be precisely described by a logarithmic function, while the increase in conidia volume exhibited a linear relationship during the observed time frame.

In summary, HTM can be applied to fungi for time-lapse or non-time-lapse imaging of living cells. Despite certain drawbacks when compared to HTM on mammalian cells, mainly due to the fungal cell wall, the technique still offers remarkable advantages when compared with other common live-cell imaging modalities. The primary benefits of this technique are its ability to provide three-dimensional resolution without the need for labeling and its low illumination power, which prevents phototoxic effects during live-cell imaging. Additionally, the microscope is easy-to-use does not require special training.

6. References

Adli, M. (2018). The CRISPR tool kit for genome editing and beyond. *Nature Communications 2018 9:1*, *9*(1), 1–13. https://doi.org/10.1038/s41467-018-04252-2

Aist, J. R. (1969). The mitotic apparatus in fungi, Ceratocystis fagacearum and Fusarium oxysporum. *The Journal of Cell Biology*, *40*(1), 120–135. https://doi.org/10.1083/JCB.40.1.120

Alexopoulos, C. J., Mims, C. W., & Blackwell, M. (1996). Introductory Mycology. 4th Edition. *Wiley, New York.*, 868. https://www.wiley.com/en-us/Introductory+Mycology%2C+4th+Edition-p-9780471522294

Aranda, P. S., Lajoie, D. M., & Jorcyk, C. L. (2012). Bleach Gel: A Simple Agarose Gel for Analyzing RNA Quality. *Electrophoresis*, *33*(2), 366. https://doi.org/10.1002/ELPS.201100335

Baker, M. (2010). Taking a long, hard look. *Nature 2010 466:7310*, *466*(7310), 1137–1138. https://doi.org/10.1038/4661137a

Baltussen, T. J. H., Zoll, J., Verweij, P. E., & Melchers, W. J. G. (2020). Molecular Mechanisms of Conidial Germination in Aspergillus spp . *Microbiology and Molecular Biology Reviews*, *84*(1). https://doi.org/10.1128/MMBR.00049-19

Baró, L., Dolinko, A. E., Rosenfeldt, S., Skigin, D. C., & Carmarán, C. (2021). *Photonics of fungal cell wall*. https://doi.org/10.48550/arXiv.2104.10848

Buzalewicz, I., Mrozowska, M., Kmiecik, A., Kulus, M., Haczkiewicz-Leśniak, K., Dzięgiel, P., Podhorska-Okołów, M., & Zadka, Ł. (2022). Quantitative Phase Imaging Detecting the Hypoxia-Induced Patterns in Healthy and Neoplastic Human Colonic Epithelial Cells. *Cells 2022, Vol. 11, Page 3599*, *11*(22), 3599. https://doi.org/10.3390/CELLS11223599

Buzalewicz, I., Ulatowska-Jarża, A., Kaczorowska, A., Gąsior-Głogowska, M., Podbielska, H., Karwańska, M., Wieliczko, A., Matczuk, A. K., Kowal, K., & Kopaczyńska, M. (2021). Bacteria Single-Cell and Photosensitizer Interaction Revealed by Quantitative Phase Imaging. *International Journal of Molecular Sciences*, *22*(10), 5068. https://doi.org/10.3390/ijms22105068

Cairns, T. C., Nai, C., & Meyer, V. (2018). How a fungus shapes biotechnology: 100 years of Aspergillus niger research. *Fungal Biology and Biotechnology*, *5*(1), 1–14. https://doi.org/10.1186/S40694-018-0054-5

Chen, X., Wu, T., Gong, Z., Guo, J., Liu, X., Zhang, Y., Li, Y., Ferraro, P., & Li, B. (2021). Lipid droplets as endogenous intracellular microlenses. *Light: Science & Applications 2021 10:1*, *10*(1), 1–11. https://doi.org/10.1038/s41377-021-00687-3

Clutterbuck, A. J. (1970). Synchronous nuclear division and septation in Aspergillus nidulans. *Journal of General Microbiology*, *60*(1), 133–135. https://doi.org/10.1099/00221287-60-1-133

Cole, R. (2014). Live-cell imaging. *Cell Adhesion & Migration*, *8*(5), 452–459. https://doi.org/10.4161/CAM.28348

Cotte, Y., Toy, F., Jourdain, P., Pavillon, N., Boss, D., Magistretti, P., Marquet, P., & Depeursinge, C. (2013). Marker-free phase nanoscopy. *Nature Photonics 2013 7:2*, *7*(2), 113–117. https://doi.org/10.1038/nphoton.2012.329

Cox, G., & Cox, G. (2012). *Optical imaging techniques in cell biology*. CRC Press. https://www.routledge.com/Optical-Imaging-Techniques-in-Cell-Biology/Cox/p/book/9781138199408

Detroy, R. W., & Ciegler, A. (1971). Induction of yeastlike development in Aspergillus parasiticus. *Journal of General Microbiology*, *65*(3), 259–264. https://doi.org/10.1099/00221287-65-3-259

Diaz, G., Melis, M., Batetta, B., Angius, F., & Falchi, A. M. (2008). Hydrophobic characterization of intracellular lipids in situ by Nile Red red/yellow emission ratio. *Micron (Oxford, England : 1993)*, *39*(7), 819–824. https://doi.org/10.1016/J.MICRON.2008.01.001

Dörsam, S., Fesseler, J., Gorte, O., Hahn, T., Zibek, S., Syldatk, C., & Ochsenreither, K. (2017). Sustainable carbon sources for microbial organic acid production with filamentous fungi. *Biotechnology for Biofuels*, *10*(1), 1–12. https://doi.org/10.1186/S13068-017-0930-X

Du Pré, S., Beckmann, N., Almeida, M. C., Sibley, G. E. M., Law, D., Brand, A. C., Birch, M., Read, N. D., & Oliver, J. D. (2018). Effect of the novel antifungal drug F901318 (olorofim) on growth and viability of aspergillus fumigatus. *Antimicrobial Agents and Chemotherapy*, *62*(8). https://doi.org/10.1128/aac.00231-18

Dundon, S. E. R., Chang, S. S., Kumar, A., Occhipinti, P., Shroff, H., Roper, M., & Gladfelter, A. S. (2016). Clustered nuclei maintain autonomy and nucleocytoplasmic ratio control in a syncytium. *Molecular Biology of the Cell*, *27*(13), 2000–2007. https://doi.org/10.1091/MBC.E16-02-0129

Dynesen, J., & Nielsen, J. (2003). Branching is coordinated with mitosis in growing hyphae of Aspergillus nidulans. *Fungal Genetics and Biology*, *40*(1), 15–24. https://doi.org/10.1016/S1087-1845(03)00053-7

El-Enshasy, H. A. (2007). Filamentous Fungal Cultures – Process Characteristics, Products, and Applications. *Bioprocessing for Value-Added Products from Renewable Resources: New Technologies and Applications*, 225–261. https://doi.org/10.1016/B978-044452114-9/50010-4

Elliott, A. D. (2020). Confocal Microscopy: Principles and Modern Practices. *Current Protocols in Cytometry*, *92*(1), e68. https://doi.org/10.1002/CPCY.68

Engler, C., Gruetzner, R., Kandzia, R., & Marillonnet, S. (2009). Golden Gate Shuffling: A One-Pot DNA Shuffling Method Based on Type IIs Restriction Enzymes. *PLOS ONE*, *4*(5), e5553. https://doi.org/10.1371/JOURNAL.PONE.0005553

Engler, C., Kandzia, R., & Marillonnet, S. (2008). A one pot, one step, precision cloning method with high throughput capability. *PloS One*, *3*(11). https://doi.org/10.1371/JOURNAL.PONE.0003647

Galilei, G. (2016). The Assayer. *The Controversy on the Comets of 1618*, 151–336. https://doi.org/10.9783/9781512801453-006

Gao, Q., Yan, D., Wang, D., Gao, S., Zhao, S., Wang, S., & Liu, Y. (2019). Variations in Nuclear Number and Size in Vegetative Hyphae of the Edible Mushroom Lentinula edodes. *Frontiers in Microbiology*, *10*, 471131. https://doi.org/10.3389/FMICB.2019.01987

Gladfelter, A. S. (2006). Nuclear anarchy: asynchronous mitosis in multinucleated fungal hyphae. *Current Opinion in Microbiology*, *9*(6), 547–552. https://doi.org/10.1016/J.MIB.2006.09.002

Grewal, H. S., & Kalra, K. L. (1995). Fungal production of citric acid. *Biotechnology Advances*, *13*(2), 209–234. https://doi.org/10.1016/0734-9750(95)00002-8

Harris, S. D. (2008). Branching of fungal hyphae: regulation, mechanisms and comparison with other branching systems. *Mycologia*, *100*(6), 823–832. https://doi.org/10.3852/08-177

Harris, S. D. (2019). Hyphal branching in filamentous fungi. *Developmental Biology*, *451*(1), 35–39. https://doi.org/10.1016/J.YDBIO.2019.02.012

Harris, S. D., Read, N. D., Roberson, R. W., Shaw, B., Seiler, S., Plamann, M., & Momany, M. (2005). Polarisome Meets Spitzenkörper: Microscopy, Genetics, and Genomics Converge. *Eukaryotic Cell*, *4*(2), 225. https://doi.org/10.1128/EC.4.2.225-229.2005

Heckman, K. L., & Pease, L. R. (2007). Gene splicing and mutagenesis by PCR-driven overlap extension. *Nature Protocols*, *2*(4), 924–932. https://doi.org/10.1038/NPROT.2007.132

Hingorani, M., Viviani, A. M. L., Sanfilippo, J. E., & Janušonis, S. (2022). High-resolution spatiotemporal analysis of single serotonergic axons in an in vitro system. *Frontiers in Neuroscience*, *16*, 994735. https://doi.org/10.3389/FNINS.2022.994735

Ijadpanahsaravi, M., Punt, M., W, H. A., & Teertstra, W. R. (2020). *Minimal nutrient requirements for induction of germination of Aspergillus niger conidia*. https://doi.org/10.1016/j.funbio.2020.11.004

Ishikawa, F. H., Souza, E. A., Read, N. D., & Roca, G. M. (2013). Colletotrichum lindemuthianum exhibits different patterns of nuclear division at different stages in its vegetative life cycle. *Mycologia*, *105*(4), 795–801. https://doi.org/10.3852/12-298

Jinek, M., Chylinski, K., Fonfara, I., Hauer, M., Doudna, J. A., & Charpentier, E. (2012). A programmable dual-RNA-guided DNA endonuclease in adaptive bacterial immunity. *Science (New York, N.Y.)*, *337*(6096), 816–821. https://doi.org/10.1126/SCIENCE.1225829

Karaffa, L., & Kubicek, C. P. (2003). Aspergillus niger citric acid accumulation: Do we understand this well working black box? *Applied Microbiology and Biotechnology*, *61*(3), 189–196. https://doi.org/10.1007/S00253-002-1201-7

Kendrick, B. (2011). Fungi: Ecological Importance and Impact on Humans. *ELS*. https://doi.org/10.1002/9780470015902.A0000369.PUB2

Kim, D., Oh, N., Kim, K., Lee, S. Y., Pack, C. G., Park, J. H., & Park, Y. K. (2018). Label-free high-resolution 3-D imaging of gold nanoparticles inside live cells using optical diffraction tomography. *Methods (San Diego, Calif.)*, *136*, 160–167. https://doi.org/10.1016/J.YMETH.2017.07.008

Kim, K., Lee, S., Yoon, J., Heo, J., Choi, C., & Park, Y. (2016). Three-dimensional label-free imaging and quantification of lipid droplets in live hepatocytes. *Scientific Reports 2016 6:1*, *6*(1), 1–8. https://doi.org/10.1038/srep36815

Kim, T. I., Kwon, B., Yoon, J., Park, I. J., Bang, G. S., Park, Y. K., Seo, Y. S., & Choi, S. Y. (2017). Antibacterial Activities of Graphene Oxide-Molybdenum Disulfide Nanocomposite Films. *ACS Applied Materials & Interfaces*, *9*(9), 7908–7917. https://doi.org/10.1021/ACSAMI.6B12464

Kisser, M., Kubicek, C. P., & Röhr, M. (1980). Influence of manganese on morphology and cell wall composition of Aspergillus niger during citric acid fermentation. *Archives of Microbiology*, *128*(1), 26–33. https://doi.org/10.1007/BF00422301

Köhler, A. (1893). Ein neues Beleuchtungsverfahren für mikrophotographische Zwecke. *Zeitschrift Für Wissenschaftliche Mikroskopie Und Für Mikroskopische Technik*, *10*(4), 433–440.

Krivosudský, O., Dráber, P., & Cifra, M. (2017). Resolving controversy of unusually high refractive index of a tubulin. *Europhysics Letters*, *117*(3), 38003. https://doi.org/10.1209/0295-5075/117/38003

Laine, R. F., Heil, H. S., Coelho, S., Nixon-Abell, J., Jimenez, A., Wiesner, T., Martínez, D., Galgani, T., Régnier, L., Stubb, A., Follain, G., Webster, S., Goyette, J., Dauphin, A., Salles, A., Culley, S., Jacquemet, G., Hajj, B., Leterrier, C., & Henriques, R. (2023). High-fidelity 3D live-cell nanoscopy through data-driven enhanced super-resolution radial fluctuation. *Nature Methods 2023*, 1–8. https://doi.org/10.1038/s41592-023-02057-w

Laissue, P. P., Alghamdi, R. A., Tomancak, P., Reynaud, E. G., & Shroff, H. (2017). Assessing phototoxicity in live fluorescence imaging. *Nature Methods 2017 14:7*, *14*(7), 657–661. https://doi.org/10.1038/nmeth.4344

Lammerding, J. (2011). Mechanics of the Nucleus. *Comprehensive Physiology*, *1*(2), 783. https://doi.org/10.1002/CPHY.C100038

Landecker, H. (2009). Seeing things: from microcinematography to live cell imaging. *Nature Methods*, *6*(10), 707–709. https://doi.org/10.1038/NMETH1009-707

Lane, N. (2015). The unseen world: reflections on Leeuwenhoek (1677) 'Concerning little animals.' *Philosophical Transactions of the Royal Society B: Biological Sciences*, *370*(1666), 20140344. https://doi.org/10.1098/RSTB.2014.0344

Larralde-Corona, C. P., López-Isunza, F., & Viniegra-González, G. (1997). Morphometric evaluation of the specific growth rate of Aspergillus niger grown in agar plates at high glucose levels. *Biotechnology and Bioengineering*, *56*(3), 287–294. https://doi.org/10.1002/(sici)1097-0290(19971105)56:3<287::aid-bit6>3.0.co;2-f

Le Rhun, A., Escalera-Maurer, A., Bratovič, M., & Charpentier, E. (2019). CRISPR-Cas in Streptococcus pyogenes. *RNA Biology*, *16*(4), 380. https://doi.org/10.1080/15476286.2019.1582974

Lee, D., Lee, M., Kwak, H., Kim, Y. S., Shim, J., Jung, J. H., Park, W., Park, J.-H., Lee, S., & Park, Y. (2022). High-fidelity optical diffraction tomography of live organisms using iodixanol refractive index matching. *Biomedical Optics Express, Vol. 13, Issue 12, Pp. 6404-6415*, *13*(12), 6404–6415. https://doi.org/10.1364/BOE.465066

Lee, S., Lee, S., Kim, K., Mubarok, A., Park, Y., Panduwirawan, A., Park, H., & Lee, K. (2014). High-Resolution 3-D Refractive Index Tomography and 2-D Synthetic Aperture Imaging of Live Phytoplankton. *Journal of the Optical Society of Korea, Vol. 18, Issue 6, Pp. 691-697*, *18*(6), 691–697. https://doi.org/10.3807/JOSK.2014.18.6.691

Lin, X., & Momany, M. (2004). Identification and complementation of abnormal hyphal branch mutants ahbA1 and ahbB1 in Aspergillus nidulans. *Fungal Genetics and Biology*, *41*(11), 998–1006. https://doi.org/10.1016/J.FGB.2004.07.005

Lipson, S. G., Lipson, H., & Tannhauser, D. S. (1995). Optical Physics. *Optical Physics*. https://doi.org/10.1017/CBO9781139170413

Mcguire, S. L., Roe, D. L., Carter, B. W., Carter, R. L., Grace, S. P., Hays, P. L., Lang, G. A., Mamaril, J. L. C., Mcelvaine, A. T., Payne, A. M., Schrader, M. D., Wahrle, S. E., & Young, C. D. (2000). *Extragenic Suppressors of the nimX2 cdc2 Mutation of Aspergillus nidulans Affect Nuclear Division, Septation and Conidiation*. https://doi.org/10.1093/genetics/156.4.1573

Mela, A. P., Rico-Ramírez, A. M., & Glass, N. L. (2020). Syncytia in Fungi. *Cells 2020, Vol. 9, Page 2255*, *9*(10), 2255. https://doi.org/10.3390/CELLS9102255

Mendenhall, M. D., & Hodge, A. E. (1998). Regulation of Cdc28 Cyclin-Dependent Protein Kinase Activity during the Cell Cycle of the Yeast Saccharomyces cerevisiae. In *MICROBIOLOGY AND MOLECULAR BIOLOGY REVIEWS* (Vol. 62, Issue 4). https://doi.org/10.1128/MMBR.62.4.1191-1243.1998

Meyer, V. (2021). Metabolic Engineering of Filamentous Fungi. *Metabolic Engineering: Concepts and Applications: Volume 13a and 13b*, *13*, 765–801. https://doi.org/10.1002/9783527823468.CH20

Neumann, F. R., & Nurse, P. (2007). Nuclear size control in fission yeast. *The Journal of Cell Biology*, *179*(4), 593–600. https://doi.org/10.1083/JCB.200708054

Nigg, E. A. (2001). Mitotic kinases as regulators of cell division and its checkpoints. *Nature Reviews Molecular Cell Biology 2001 2:1*, *2*(1), 21–32. https://doi.org/10.1038/35048096

Nomarski, G. (1955). Nouveau dispositif pour l'observation en contraste de phase différentiel. *Journal de Physique et Le Radium*, *16*(9).

Novodvorska, M., Hayer, K., Pullan, S. T., Wilson, R., Blythe, M. J., Stam, H., Stratford, M., & Archer, D. B. (2013). Trancriptional landscape of Aspergillus niger at breaking of conidial dormancy revealed by RNA-sequencing. *BMC Genomics*, *14*(1), 1–18. https://doi.org/10.1186/1471-2164-14-246

Ntana, F., Mortensen, U. H., Sarazin, C., & Figge, R. (2020). Aspergillus: A Powerful Protein Production Platform. *Catalysts 2020, Vol. 10, Page 1064*, *10*(9), 1064. https://doi.org/10.3390/CATAL10091064

Odermatt, P. D., Miettinen, T. P., Lemière, J., Kang, J. H., Bostan, E., Manalis, S. R., Huang, K. C., & Chang, F. (2021). Variations of intracellular density during the cell cycle arise from tip-growth regulation in fission yeast. *ELife*, *10*. https://doi.org/10.7554/ELIFE.64901

Park, H., Ahn, T., Kim, K., Lee, S., Kook, S., Lee, D., Suh, I. B., Na, S., & Park, Y. (2015). Three-dimensional refractive index tomograms and deformability of individual human red blood cells from cord blood of newborn infants and maternal blood. *Journal of Biomedical Optics*, *20*(11), 111208. https://doi.org/10.1117/1.JBO.20.11.111208

Park, S., Kim, H., Woo, M., & Kim, M. (2022). Label-free detection of leukemic myeloblasts in hyaluronic acid. *Journal of Biological Engineering*, *16*(1), 1–9. https://doi.org/10.1186/S13036-022-00308-6

Park, Y. K., Depeursinge, C., & Popescu, G. (2018). Quantitative phase imaging in biomedicine. *Nature Photonics 2018 12:10*, *12*(10), 578–589. https://doi.org/10.1038/s41566-018-0253-x

Park, Y. K., Diez-Silva, M., Popescu, G., Lykotrafitis, G., Choi, W., Feld, M. S., & Suresh, S. (2008). Refractive index maps and membrane dynamics of human red blood cells parasitized by Plasmodium falciparum. *Proceedings of the National Academy of Sciences of the United States of America*, *105*(37), 13730. https://doi.org/10.1073/PNAS.0806100105

Patterson, G. H., Knobel, S. M., Sharif, W. D., Kain, S. R., & Piston, D. W. (1997). Use of the green fluorescent protein and its mutants in quantitative fluorescence microscopy. *Biophysical Journal*, *73*(5), 2782–2790. https://doi.org/10.1016/S0006-3495(97)78307-3

Paul, G. C., Priede, M. A., & Thomas, C. R. (1999). Relationship between morphology and citric acid production in submerged Aspergillus niger fermentations. *Biochemical Engineering Journal*, *3*(2), 121–129. https://doi.org/10.1016/S1369-703X(99)00012-1

Peñalva, M. A. (2005). Tracing the endocytic pathway of Aspergillus nidulans with FM4-64. *Fungal Genetics and Biology : FG & B*, *42*(12), 963–975. https://doi.org/10.1016/J.FGB.2005.09.004

Reinfurt, A., Fritsche, S., Bíró, V., Márton, A., Ellena, V., Fekete, E., Sándor, E., Karaffa, L., & Steiger, M. G. (2023). Manganese(II) ions suppress the transcription of the citrate exporter encoding gene cexA in Aspergillus niger. *Frontiers in Bioengineering and Biotechnology*, *11*. https://doi.org/10.3389/FBIOE.2023.1292337

Riquelme, M., & Bartnicki-Garcia, S. (2004). Key differences between lateral and apical branching in hyphae of Neurospora crassa. *Fungal Genetics and Biology*, *41*(9), 842–851. https://doi.org/10.1016/J.FGB.2004.04.006

Riquelme, M., & Sánchez-León, E. (2014). The Spitzenkörper: a choreographer of fungal growth and morphogenesis. *Current Opinion in Microbiology*, *20*, 27–33. https://doi.org/10.1016/J.MIB.2014.04.003

Ruiz-Roldán, M. C., Köhli, M., Roncero, M. I. G., Philippsen, P., Di Pietro, A., & Espeso, E. A. (2010). Nuclear Dynamics during Germination, Conidiation, and Hyphal Fusion of Fusarium oxysporum. *Eukaryotic Cell*, *9*(8), 1216. https://doi.org/10.1128/EC.00040-10

Sanchez-Diaz, A., Nkosi, P. J., Murray, S., & Labib, K. (2012). The Mitotic Exit Network and Cdc14 phosphatase initiate cytokinesis by counteracting CDK phosphorylations and blocking polarised growth. *The EMBO Journal*, *31*(17), 3620–3634. https://doi.org/10.1038/EMBOJ.2012.224

Sandoz, P. A., Tremblay, C., Gisou van der Goot, F., & Frechin, M. (2019). Image-based analysis of living mammalian cells using label-free 3D refractive index maps reveals new organelle dynamics and dry mass flux. *PLOS Biology*, *17*(12), e3000553. https://doi.org/10.1371/JOURNAL.PBIO.3000553

Sarkari, P., Marx, H., Blumhoff, M. L., Mattanovich, D., Sauer, M., & Steiger, M. G. (2017). An efficient tool for metabolic pathway construction and gene integration for Aspergillus niger. *Bioresource Technology*, *245*(Pt B), 1327–1333. https://doi.org/10.1016/J.BIORTECH.2017.05.004

Schier, N., & Fischer, R. (2002). The Aspergillus nidulans cyclin PclA accumulates in the nucleus and interacts with the central cell cycle regulator NimXCdc2. *FEBS Letters*, *523*(1–3), 143–146. https://doi.org/10.1016/S0014-5793(02)02964-2

Schindelin, J., Arganda-Carreras, I., Frise, E., Kaynig, V., Longair, M., Pietzsch, T., Preibisch, S., Rueden, C., Saalfeld, S., Schmid, B., Tinevez, J. Y., White, D. J., Hartenstein, V., Eliceiri, K., Tomancak, P., & Cardona, A. (2012). Fiji: an open-source platform for biological-image analysis. *Nature Methods 2012 9:7*, *9*(7), 676–682. https://doi.org/10.1038/nmeth.2019

Schürmann, M., Scholze, J., Müller, P., Guck, J., & Chan, C. J. (2016). Cell nuclei have lower refractive index and mass density than cytoplasm. *Journal of Biophotonics*, *9*(10), 1068–1076. https://doi.org/10.1002/JBIO.201500273

Serna, L., & Stadler, D. (1978). Nuclear division cycle in germinating conidia of Neurospora crassa. *Journal of Bacteriology*, *136*(1), 341–351. https://doi.org/10.1128/JB.136.1.341-351.1978

Shahi, S., Beerens, B., Manders, E. M. M., & Rep, M. (2015). Dynamics of the establishment of multinucleate compartments in Fusarium oxysporum. *Eukaryotic Cell*, *14*(1), 78–85. https://doi.org/10.1128/EC.00200-14

Shin, M., Cha, N., Koranteng, F., Cho, B., & Shim, J. (2020). Subpopulation of Macrophage-Like Plasmatocytes Attenuates Systemic Growth via JAK/STAT in the Drosophila Fat Body. *Frontiers in Immunology*, *11*, 508529. https://doi.org/10.3389/FIMMU.2020.00063

Slepecky, R. A., & Starmer, W. T. (2009). Phenotypic plasticity in fungi: a review with observations on Aureobasidium pullulans. *Mycologia*, *101*(6), 823–832. https://doi.org/10.3852/08-197

Snyder, D. L., Conchello, J.-A., & Preza, C. (1999). Theoretical development and experimental evaluation of imaging models for differential-interference-contrast microscopy. *JOSA A, Vol. 16, Issue 9, Pp. 2185-2199*, *16*(9), 2185–2199. https://doi.org/10.1364/JOSAA.16.002185

Steelman, Z. A., Eldridge, W. J., Weintraub, J. B., & Wax, A. (2017). Is the nuclear refractive index lower than cytoplasm? Validation of phase measurements and implications for light scattering technologies. *Journal of Biophotonics*, *10*(12), 1714. https://doi.org/10.1002/JBIO.201600314

Stegmeier, F., & Amon, A. (2004). Closing mitosis: the functions of the Cdc14 phosphatase and its regulation. *Annual Review of Genetics*, *38*, 203–232. https://doi.org/10.1146/ANNUREV.GENET.38.072902.093051

Swedlow, J. R., & Platani, M. (2002). Live cell imaging using wide-field microscopy and deconvolution. *Cell Structure and Function*, *27*(5), 335–341. https://doi.org/10.1247/CSF.27.335

Tong, Z., Zheng, X., Tong, Y., Shi, Y. C., & Sun, J. (2019). Systems metabolic engineering for citric acid production by Aspergillus niger in the post-genomic era. *Microbial Cell Factories*, *18*(1), 1–15. https://doi.org/10.1186/S12934-019-1064-6

Trinci, A. P. J. (1984). Regulation of hyphal branching and hyphal orientation. . In H. H. Jennings & A. D. M. Rayner (Eds.), *The Ecology and Physiology of the Fungal Mycelium. Symposium of British Mycological Society.* (Vol. 8, pp. 24–52). Cambridge University Press.

Veiter, L., Rajamanickam, V., & Herwig, C. (2018). The filamentous fungal pellet—relationship between morphology and productivity. *Applied Microbiology and Biotechnology*, *102*(7), 2997–3006. https://doi.org/10.1007/S00253-018-8818-7

Wang, F., Sethiya, P., Hu, X., Guo, S., Chen, Y., Li, A., Tan, K., & Wong, K. H. (2021). Transcription in fungal conidia before dormancy produces phenotypically variable conidia that maximize survival in different environments. *Nature Microbiology 2021 6:8*, *6*(8), 1066–1081. https://doi.org/10.1038/s41564-021-00922-y

Wang, H., Garí, E., Vergés, E., Gallego, C., & Aldea, M. (2004). Recruitment of Cdc28 by Whi3 restricts nuclear accumulation of the G1 cyclin–Cdk complex to late G1. *The EMBO Journal*, *23*(1), 180. https://doi.org/10.1038/SJ.EMBOJ.7600022

Weber, E., Engler, C., Gruetzner, R., Werner, S., & Marillonnet, S. (2011). A Modular Cloning System for Standardized Assembly of Multigene Constructs. *PLOS ONE*, *6*(2), e16765. https://doi.org/10.1371/JOURNAL.PONE.0016765

Xiao, B., Deng, X., Zhou, W., & Tan, E. K. (2016). Flow Cytometry-Based Assessment of Mitophagy Using MitoTracker. *Frontiers in Cellular Neuroscience*, *10*(MAR2016), 76. https://doi.org/10.3389/FNCEL.2016.00076

Ye, X. S., Xu, G., Pu, R. T., Fincher, R. R., McGuire, S. L., Osmani, A. H., & Osmani, S. A. (1995). The NIMA protein kinase is hyperphosphorylated and activated downstream of p34cdc2/cyclin B: coordination of two mitosis promoting kinases. *The EMBO Journal*, *14*(5), 986–994. https://doi.org/10.1002/J.1460-2075.1995.TB07079.X

Yin, Z., Kanade, T., & Chen, M. (2012). Understanding the Phase Contrast Optics to Restore Artifact-free Microscopy Images for Segmentation. *Medical Image Analysis*, *16*(5), 1047. https://doi.org/10.1016/J.MEDIA.2011.12.006

Zernike, F. (1955). How I discovered phase contrast. *Science*, *121*(3141), 345–349. https://doi.org/10.1126/SCIENCE.121.3141.345

7. Appendix

7.1. Media and buffer

All media were sterilized by autoclavation or sterile filtering if not stated otherwise.

ASPA+N [1 L, 50x]

Substance	Amount
$NaNO_3$	297.5 g
KCl	26.1 g
KH_2PO_4	74.8 g

The salts were dissolved in 600 mL ddH_2O and the pH was set to 5.5 with 5M KOH. It was then filled up to 1 L with ddH_2O and autoclaved.

Biotin solution [50 mL]

The biotin solution was prepared by dissolving 5 mg biotin in 50 mL ddH_2O. The solution was then sterile filtered.

Complete medium (CM) [500 mL]

0.5 g of casein protein and 2.5g of yeast extract are added to 480 mL of ddH_2O and autoclaved.

Added under sterile conditions	Amount
Sterile Glucose 50% (w/v)	10 mL
ASPA+N (50x)	10 mL
Sterile $MgSO_4$ 1M	1 mL
Trace element solution (1000x)	500 µL

Lysing solution [10 mL]

400 mg Vinotaste Pro (Novozymes, Bagsværd, Denmark) was dissolved in 10 mL SMC and subsequently sterile filtered.

Lysogeny broth (LB) [1 L]

Substance	Amount
Tryptone	10 g
Yeast extract	5 g
NaCl	5 g

If LB is used for plates, 15 g agar (1.5% w/v) is added before autoclavation. Supplemented with kanamycin (50 µg/mL) or ampicillin (100 µg/mL) for selection.

Malt Extract (MEX) [500 mL]

10 g malt extract was dissolved in 500 mL ddH_2O and autoclaved. If plates were prepared, 7.5 g agar was added prior to autoclavation.

Mandels-Andreotti medium (MA) [500 mL]

Substance	Amount
KH_2PO_4	1 g
$(NH_4)_2SO_4$	0.7 g
$CaCl_2$ * 2 H_2O	0.2 g
$MgSO_4$ * 7 H_2O	0.15 g
Urea	0.15 g
$FeSO_4$ * 7 H_2O	0.0025 g
$CoCl_2$ * 6 H_2O	0.001 g
$MnSO_4$ * H_2O	0.0008 g
$ZnSO_4$ * 7 H_2O	0.0007 g
D-Glucose * 1 H_2O	5.5 g
Peptone	0.38 g

Minimal medium (MM) [500 mL]

Added under sterile conditions	Amount
Sterile ddH_2O	480 mL
Sterile Glucose 50% (w/v)	10 mL
ASPA+N (50x)	10 mL
Sterile $MgSO_4$ 1M	1 mL
Trace element solution (1000x)	500 µL

If MM is used for plates, 8 g agar (1.5%) is added to 480 mL ddH_2O, and it is then autoclaved before the other substances are added under sterile conditions.

Minimal medium *A. pullulans* [1 L]

Added under sterile conditions	Amount
5x salt concentration buffer	200 mL
$MgSO_4$ * 7 H_2O 2% (w/v)	10 mL
Yeast extract 4% (w/v)	10 mL
Sterile glucose 20% (w/v)	1 mL
Sterile ddH_2O	To 1 L

Stock solutions were prepared separately and autoclaved.

Minimal medium + sucrose (MMS) [500 mL]

162.6g of D(+)-saccharose was dissolved in approx. 300 mL of ddH_2O, 7.5g (1.5% w/v) of noble agar was added, it was filled up to 486 mL with ddH_2O and autoclaved.

Added under sterile conditions	Amount
ASPA+N	10 mL
$MgSO_4$ (1M)	1 mL
Trace element solution (1000x)	500 µL
Hygromycin (50 mg/mL)	2 mL

MMS top agar [500 mL]

The recipe is generally the same as 500 mL MMS. Only 4 g of noble agar (0.75% w/v) are used instead of 7.5 g before autoclavation and no hygromycin is added afterwards. After autoclavation the medium is stored in the water bath at 47-50 °C.

PEG 6000 solution [10 mL]

2.5 g of PEG 6000 was dissolved in 10 mL TC buffer.

PBS [1 L]

Substance	Amount
NaCl	8 g
KCl	0.2 g
Na_2HPO_4	1.42 g
KH_2PO_4	0.27 g

5x salt concentration buffer [1 L]

Substance	Amount
$(NH_4)_2SO_4$	3 g
K_2HPO_4	25 g
NaCl	5 g

The salts were dissolved in approx. 600 mL ddH_2O and the pH was set to 6.0 1M HCl. It was then filled up to 1 l with ddH_2O and autoclaved.

SMC [1 L]

Substance	Amount
D-sorbitol	242.3 g
$CaCl_2$ * 2 H_2O	7.3 g
MES hydrate	3.9 g

The substances were dissolved in approx. 600 mL ddH_2O and the pH was set to 5.8 using 1M NaOH and 1M HCl. It was then filled up to 1 L with ddH_2O and autoclaved.

STC [1 L]

242.3 g D-sorbitol were dissolved in 600 mL TC. It was then filled up to 1 L and autoclaved.

Super Optimal broth with Catabolite repression (SOC) [500 mL]

Substance	Amount
Yeast extract	2.5 g
Tryptone	10 g
NaCl	0.3 g
KCl	0.1 g
$MgCl_2$ * 6 H_2O	1.03 g
$MgSO_4$ * 7 H_2O	1.23 g
D-Glucose * 1 H_2O	1.98 g

An aqueous solution of the Mg^{2+} components and glucose were prepared and autoclaved separately and then added to the other substances. It was then filled up to 500 mL with sterile dd H_2O.

TC [1 L]

Substance	Amount
$CaCl_2$ * 2 H_2O	7.3 g
Tris	1.2 g

The substances were dissolved in 800 mL ddH_2O and the pH was set to 5.8 using 1M NaOH and 1M HCl. It was filled up to 1 L with ddH_2O and autoclaved.

Trace element solution [1 L, 1000x]

Substance	Amount
EDTA	10 g
$ZnSO_4$ * 7 H_2O	4.4 g
$MnCl_2$ * 4 H_2O	1.01 g
$CoCl_2$ * 6 H_2O	0.32 g
$CuSO_4$ * 5 H_2O	0.315 g
$(NH_4)_6Mo_7O_{24}$ * 4 H_2O	0.22 g
$CaCl_2$ * 2 H_2O	1.47 g
$FeSO_4$ * 7 H_2O	1.0 g

The salts were dissolved in 600 mL ddH_2O and the pH was set to 4.0 with 1M NaOH and 1M HCl. It was then filled up to 1 L with ddH_2O and autoclaved.

Trace element solution VM [100 mL]

Substance	Amount
Citric acid * 1 H_2O	5 g
$ZnSO_4$ * 7 H_2O	5 g
$Fe(NH_4)_2(SO_4)_2$ * 6 H_2O	1 g
$CuSO_4$ * 5 H_2O	4 g
H_3BO_3, anhydrous	0.05 g
Na_2MoO_4 * 2 H_2O	0.05 g

Vogel's medium [1 L]

220 g/L glucose D-Glucose * 1 H_2O was dissolved in 980 mL ddH_2O. The medium was then sterile filtered and 20 mL of Vogel's salts were added under sterile conditions.

Vogel's salts [1 L, 50x]

Substance	Amount
Trisodium citrate * 2 H_2O	125 g
KH_2PO_4	250 g
NH_4NO_3	100 g
$MgSO_4$ * 7 H_2O	10 g
$CaCl_2$ * 2 H_2O	5 g
Trace element solution VM	5 mL
Biotin solution	2.5 mL

7.2. List of Abbreviations

ATP	Adenosine triphosphate
BB	Backbone
CDCFDA	5(6)-Carboxy-2',7'-dichlorofluorescein diacetate
CDK	Cyclin-dependent kinase
CDS	Coding sequence
CM	Complete medium
CRISPR	Clustered regularly interspaced short palindromic repeat
crRNA	CRISPR RNA
DAPI	4',6-diamidino-2-phenylindole
DEPC	Diethyl pyrocarbonate
DIC	Differential interference contrast
DMSO	Dimethyl sulfoxide
DNA	Deoxyribonucleic acid
dNTP	Deoxyribose nucleoside triphosphate
EDTA	Ethylenediaminetetraacetic acid
ER	Endoplasmatic reticulum
FS	Fusion sites
GAPDH	Glyceraldehyde 3-phosphate dehydrogenase
gDNA	Genomic DNA
HT	Holotomographic
HTM	Holotomographic microscopy
hyg	Hygromycine
INDEL	Insertion/Deletion
LSCM	Laser scanning confocal microscopy
MA	Mandels-Andreotti medium
MES hydrate	2-(N-morpholino)ethanesulfonic acid
MEX	Malt-extract medium
MM	Minimal medium
MMS	Minimal medium with sucrose
NA	Numerical aperture
NEB	New England Biolabs
NHEJ	Non-homologous end joining
N/C	Nuclear volume over cytoplasm volume
o/n	Over night
P	Promoter
PALM	Photoactivation localization microscopy
PAM	Protospacer-adjacent motif
PBS	Phosphate-buffered saline

PCM	Phase contrast microscopy
PCR	Polymerase chain reaction
PEG	Polyethylene glycol
PFK-1	Phosphofructokinase 1
QPI	Quantitative phase imaging
RI	Refractive index
RNA	Ribonucleic acid
ROS	Reactive oxygen species
RT	Room temperature
SDCM	Spinning disc confocal microscopy
sGFP	Superfolder green fluorescent protein
sgRNA	Single guide RNA
SMC	Sorbitol-MES-calcium chloride buffer
SMLM	Single-molecule localization microscopy
SOC	Super Optimal broth with Catabolite repression
SOFI	Super-resolution optical fluctuation imaging
SOP	Standard Operating Procedure
SRM	Super-resolution microscopy
SRRFs	Super-resolution radial fluctiations
STC	Sorbitol-tris-calcium chloride buffer
STED	Stimulated emission depletion
STORM	Stochastic optical reconstruction microscopy
T	Terminator
TAE	Tris-acetic acid-EDTA buffer
TC	Tris-calcium chloride buffer
#N/C	Nuclear number per unit volume of cytoplasm

7.3. List of Figures

7.4. List of Tables

7.5. List of Chemicals

***Table 12**: List of chemicals and reagents used.*

Chemicals and reagents	MW [g/mol]	Supplier
10X reaction buffer with $MgCl_2$		ThermoFisher Scientific, Waltham, MA
2X RNA Loading Dye		ThermoFisher Scientific, Waltham, MA
5(6)-Carboxy-2',7'-dichlorofluorescein diacetate	529.3	Enzo Life Sciences, Farmingdale, NY
Agar-Agar, bacteriological	-	Carl Roth GmbH, Karlsruhe, Germany
Agar-Agar, Noble Quality	-	Carl Roth GmbH, Karlsruhe, Germany
Agarose	306.27 (Monomer)	VWR International, Radnor, PA
Ammonium heptamolybdate tetrahydrate	1,235.86	Merck KGaA, Darmstadt, Germany
Ammonium iron(II) sulfate hexahydrate	392.14	Carl Roth GmbH, Karlsruhe, Germany
Ammonium nitrate	80.04	Sigma-Aldrich, St. Louis, MO
Ammonium sulfate	132.14	Carl Roth GmbH, Karlsruhe, Germany
ATP	549.19	BLD Pharmatech Ltd., Shanghai, China
Biotin	244.31	ThermoFisher Scientific, Waltham, MA
Boric acid	61.83	Sigma-Aldrich, St. Louis, MO
BpiI		ThermoFisher Scientific, Waltham, MA
BsaI		NEB, Ipswich, MA
Calcium chloride dihydrate	147.02	Carl Roth GmbH, Karlsruhe, Germany
Citric acid monohydrate	210.14	Sigma-Aldrich, St. Louis, MO
Cobalt(II) chloride hexahydrate	237.93	Carl Roth GmbH, Karlsruhe, Germany
Copper(II) sulfate pentahydrate	249.69	Merck KGaA, Darmstadt, Germany
CutSmart buffer		NEB, Ipswich, MA
D(+)-glucose monohydrate	198.17	Carl Roth GmbH, Karlsruhe, Germany
Dimethylsulfoxid, DMSO	78.13	Carl Roth GmbH, Karlsruhe, Germany
Dipotassium phosphate	174.2	Carl Roth GmbH, Karlsruhe, Germany

Disodium phosphate	141.96	Carl Roth GmbH, Karlsruhe, Germany
DNase I		ThermoFisher Scientific, Waltham, MA
dNTPs		NEB, Ipswich, MA
D-sorbitol	182.17	Sigma-Aldrich, St. Louis, MO
Doxycycline	444.43	Sigma-Aldrich, St. Louis, MO
Ethanol	46.07	Merck KGaA, Darmstadt, Germany
Ethylenediaminetetraacetic acid, EDTA	292.24	Merck KGaA, Darmstadt, Germany
Hydrochloric acid	36.46	Sigma-Aldrich, St. Louis, MO
Hygromycin B	527.53	Carl Roth GmbH, Karlsruhe, Germany
Iron(II) sulfate heptahydrate	278.02	Merck KGaA, Darmstadt, Germany
Lysing enzymes (*Trichoderma harzianum*)		Carl Roth GmbH, Karlsruhe, Germany
Magnesium chloride hexahydrate	203.3	Sigma-Aldrich, St. Louis, MO
Magnesium sulfate heptahydrate	246.47	Carl Roth GmbH, Karlsruhe, Germany
Manganese(II) chloride tetrahydrate	197.91	Carl Roth GmbH, Karlsruhe, Germany
Manganese(II) sulfate monohydrate	169.02	Carl Roth GmbH, Karlsruhe, Germany
MES hydrate	195.2	Sigma-Aldrich, St. Louis, MO
Midori Green	-	Nippon Genetics Europe GmbH, Düren, Germany
MitoTracker™ Deep Red FM	-	ThermoFisher Scientific, Waltham, MA
NEB 1kb Plus DNA Ladder		NEB, Ipswich, MA
NEBuffer 3.1		NEB, Ipswich, MA
Nile Red	318.37	Sigma-Aldrich, St. Louis, MO
NucBlue™ Live ReadyProbes™ Reagent		ThermoFisher Scientific, Waltham, MA
Peptone	-	Merck KGaA, Darmstadt, Germany
Polyethylene glycol 6000	5000 - 7500	Merck KGaA, Darmstadt, Germany
Potassium chloride	74.55	Carl Roth GmbH, Karlsruhe, Germany
Potassium dihydrogen phosphate	136.09	Carl Roth GmbH, Karlsruhe, Germany
Q5 Buffer		NEB, Ipswich, MA
Q5 High Fidelity DANN Polymerase		NEB, Ipswich, MA

RiboRuler RNA Ladder		ThermoFisher Scientific, Waltham, MA
RNAzole	-	Sigma-Aldrich, St. Louis, MO
Sodium chloride	58.44	Carl Roth GmbH, Karlsruhe, Germany
Sodium hydroxide	40	Carl Roth GmbH, Karlsruhe, Germany
Sodium molybdate dihydrate	241.95	Carl Roth GmbH, Karlsruhe, Germany
Sodium nitrate	84.99	Merck KGaA, Darmstadt, Germany
T4 DNA ligase		NEB, Ipswich, MA
T4 DNA ligase buffer		NEB, Ipswich, MA
TAE buffer		Carl Roth GmbH, Karlsruhe, Germany
Tris	121.14	Carl Roth GmbH, Karlsruhe, Germany
Trisodium citrate dihydrate	294.1	Merck KGaA, Darmstadt, Germany
Tryptone	-	Merck KGaA, Darmstadt, Germany
Tween® 20, Polysorbat 20	1,227.54	Sigma-Aldrich, St. Louis, MO
Tween® 80, Polysorbat 80	1310	Merck KGaA, Darmstadt, Germany
Urea	60.06	ITW, Glenview, IL
Uridine	244.2	Carl Roth GmbH, Karlsruhe, Germany
Vinotaste® Pro	-	Novozymes, Bagsværd, Denmark
Yeast extract	-	Merck KGaA, Darmstadt, Germany
Zinc(II) sulfate heptahydrate	287.53	Merck KGaA, Darmstadt, Germany

7.6. List of Devices

***Table 13**: List of devices used.*

Devices	Source	Approach
3D Cell Explorer-fluo	Nanolive SA, Tolochenaz, Switzerland	HTM, fluorescence imaging
Binder Series B	Binder GmbH, Tuttlingen, Germany	Incubator
ChemiDoc MP Imaging System	Bio-Rad Laboratories, Hercules, CA	Gel imaging
Eppendorf® ThermoMixer® Compact	Eppendorf SE, Hamburg, Germany	Heating/mixing
FastPrep-24	MP Biomedicals, Santa Ana, CA	Cell disruption
Heidolph MR Hei-Standard	Heidolph Instruments, Schwabach, Germany	Magnetic stirrer
Herasafe KS	ThermoFisher Scientific, Waltham, MA	Sterile work bench
Kojair Biozard Golden Line biosafety cabinet	Kojair Tech Oy, Mänttä-Vilppula, Finland	Sterile work bench
Labor-pH Meter inoLab® pH 7110	Xylem, Washington, D. C.	Setting of pH
Leica DMi8	Leica Camera, Wetzlar, Germany	Epifluorescence microscopy
Microscope TR 500	VWR International, Radnor, PA	Light microscopy
Multitron Standard	Infors AG, Bottmingen, Switzerland	Shaker, Incubator
Nanodrop One	ThermoFisher Scientific, Waltham, MA	Determination of DNA/RNA concentration
PowerPac™ Basic Power Supply	Bio-Rad Laboratories, Hercules, CA	Gel electrophoresis
Sigma 1-14K Centrifuge	Sigma-Aldrich, St. Louis, MO	Centrifugation
Sigma 3-30K Centrifuge	Sigma-Aldrich, St. Louis, MO	Centrifugation

7.7. List of Kits

***Table 14**: List of kits used.*

Kits	Supplier	Approach
HiYield® Plasmid Mini Kit	IBL Baustoff und Labor GmbH, Gerasdorf bei Wien, Austria	Plasmid purification
Wizard Genomic DNA Preparation Kit	Promega, Madison, WI	gDNA extraction
innuPREP RNA Mini Kit 2.0	IST Innuscreen, Berlin, Germany	RNA extraction
HiYield® Gel/PCR DNA Fragment Extraction Kit	IBL Baustoff und Labor GmbH, Gerasdorf bei Wien, Austria	Gel purification
RevertAid First Strand cDNA Synthesis Kit	ThermoFisher Scientific, Waltham, MA	first strand cDNA synthesis

7.8. Primerlist

***Table 15**: List of Primers used. Primers were purchased from Integrated DNA Technologies, Coralville, IA. Nucleotides in small letters are fusion sites or are used to introduce point mutations to remove cleavage sites.*

Usage	Sequence	Nr.
PCR verification, pyrG 5'-prime, forward	TTTTGGTTAGCACCTACGCTAGTCTATCAG	1
PCR verification, sGFP FSX, reverse	gtggtctcctcatTTACTTGTACAGCTCGTCCATGCC	2
PCR verification, tet-on, reverse	CGCGGCCGCATGATTCATGACGTATAT	3
PCR verification, tet-on, forward	CCATGCATGGTTGCCTAGTGAATGC	4
PCR verification, pyrG 3'-prime, reverse	CATCGGAAGCACAATGAGGCGAGTTT	5
NimX check 1, forward	CGAGAAGATTGGAGAAGGTACG	6
NimX check 1, reverse	TGAGTAGGGAGATTTCACGGAT	7
NimX check 2, forward	TCAAACCCACTTTCCCTAAATG	8
NimX check 2, reverse	CCGGGTACGTCCTGAGTAGTAG	9
α-tubulin 1st fragment, FS1 forward	atggtctccATGAGAGAAGTTATTTCTTTGAACGTT	10
α-tubulin 1st fragment, reverse	ACCAGGAAACCCTGtAGACCAGCGCAGTTG	11
α-tubulin 2nd fragment, forward	CAGGGTTTCCTGGTtTTCCACTCC	12
α-tubulin 2nd fragment, reverse	CACGGCAGCGTGaGTCTCCTTGG	13
α-tubulin 3rd fragment, forward	CTGCCGTGGCCACCCTtAAGACTAAGC	14
α-tubulin 3rd fragment, reverse	gtggtctccaagcCTAGTACTCGGCCTCAACCTC	15
α-tubulin, FS sGFP, reverse	gtggtctccaagcCTAGTACTCGG	16
sGFP, FS2, forward	atGGTCTCCCATGGTGAGCAAGGGCGAG	17
sGFP, FS α-tubulin, reverse	gtggtctccTCATggcggcggcCTTGTACAGCTCGTCCATG	18
NimX 1st fragment FS2, forward	atggtctccATGGAGAACTACCAGAAGATCGAGAAGATTGGAGAAG GAACtTATGG	19
NimX 1st fragment, reverse	CTTGAGGTCGAGATCGAGGAATTCGAAaACGAGATAGAGC	20

NimX 2nd fragment, forward	TCGATCTCGACCTCAAGAAGTATATGG	21
NimX 2nd fragment, reverse	CGAGGAGGTCCAGACCATCtTCTTCAAGGTCA	22
NimX 3rd fragment, forward	GGTCTGGACCTCCTCGATGCTC	23
NimX 3rd fragment, FS3, reverse	gtggtctccaagcCTAGTTAAAACCATTCCTCCGGGTAC	24
sGFP, FS NimX, reverse	gtggtctccCCATggcggcggcCTTGTACAGCTCGTCCATGC	25
NimX, FS1, forward	atggtctccATGGAGAACTACCAGAAGATCGAG	26
NimX, FS sGFP, reverse	gtggtctccaagcCTAGTTAAAACCATTCCT	27

7.9. List of generated DNA sequences and BBs

***Table 16**: List of generated DNA sequences and BBs.*

Type	Name
DNA fragment	tubAmut
DNA fragment	NimXmut
Plasmid	BB1_tubAmut:sGFP
Plasmid	BB1_NimXmut:sGFP
Plasmid	BB2_tet-on:tubAmut:sGFP_trpC
Plasmid	BB2_tet-on:NimXmut:sGFP_trpC
Plasmid	BB3_hyg_KanOri_pyrG5'_tet-on:tubAmut:sGFP_trpC_pcoxA:pyrGtrunc_AMA1_2.8
Plasmid	BB3_hyg_KanOri_pyrG5'_tet-on:NimXmut:sGFP_trpC_pcoxA:pyrGtrunc_AMA1_2.8

7.10. List of engineered *A. niger* strains

***Table 17**: List of engineered A. niger strains used in this work.*

Parental strain	Genotype/Expression cassette	Name
ATCC 1015	Δ*pyrG*	A621 (provided by the lab)
ACIB1	Δ*pyrG*	K621 (provided by the lab)
A621	Tet-on:H2Amut:sGFP_trpC at *pyrG* locus	A621_H2A:sGFP (provided by the lab)
K621	Tet-on:H2Amut:sGFP_trpC at *pyrG* locus	K621_H2A:sGFP
A621	Tet-on:tubAmut:sGFP_trpC at *pyrG* locus	A621_tubA:sGFP
K621	Tet-on:tubAmut:sGFP_trpC at *pyrG* locus	K621_tubA:sGFP
A621	Tet-on:NimXmut:sGFP_trpC at *pyrG* locus	A621_NimX:sGFP
K621	Tet-on:NimXmut:sGFP_trpC at *pyrG* locus	K621_NimX:sGFP

7.11. Online material

Link: https://doi.org/10.48436/nxt26-y4977

Content:

Video 1 (Nuclear dynamics in *A. niger* A621_H2A:sGFP)

Video 2 (Behavior of nimX^{Cdc2} in *A. niger* A621_nimX:sGFP)

Standard Operating Procedure for Software Steve and Fiji